저작자표시-비영리-변경금지 2.0 대한민국

이용자는 아래의 조건을 따르는 경우에 한하여 자유롭게

- 이 저작물을 복제, 배포, 전송, 전시, 공연 및 방송할 수 있습니다.

다음과 같은 조건을 따라야 합니다:

저작자표시. 귀하는 원저작자를 표시하여야 합니다.

비영리. 귀하는 이 저작물을 영리 목적으로 이용할 수 없습니다.

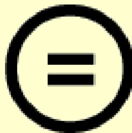

변경금지. 귀하는 이 저작물을 개작, 변형 또는 가공할 수 없습니다.

- 귀하는, 이 저작물의 재이용이나 배포의 경우, 이 저작물에 적용된 이용허락조건을 명확하게 나타내어야 합니다.
- 저작권자로부터 별도의 허가를 받으면 이러한 조건들은 적용되지 않습니다.

저작권법에 따른 이용자의 권리는 위의 내용에 의하여 영향을 받지 않습니다.

이것은 이용허락규약(Legal Code)을 이해하기 쉽게 요약한 것입니다.

Disclaimer

dCollection

Ph.D. DISSERTATION

Electrical Switching Characteristics of Chalcogenide Thin Films

by

Sijung Yoo

February 2019

DEPARTMENT OF MATERIALS SCIENCE AND ENGINEERING

COLLEGE OF ENGINEERING

SEOUL NATIONAL UNIVERSITY

Electrical Switching Characteristics of Chalcogenide Thin Films

Advisor: Prof. Cheol Seong Hwang

by

Sijung Yoo

A thesis submitted to the Graduate Faculty of Seoul National University in partial fulfillment of the requirements for the Degree of Doctor of Philosophy
Department of Materials Science and Engineering

February 2019

Approved
by

Chairman of Advisory Committee: Seungwu Han
Vice-chairman of Advisory Committee: Cheol Seong Hwang
Advisory Committee: Young Chang Joo
Advisory Committee: Byung Joon Choi
Advisory Committee: Taeyong Eom

Abstract

Chalcogenide materials have gained tremendous attentions since early report by S. Ovshinksy due to its unique electrical switching characteristics including volatile switching often referred as Ovonic Threshold Switching (OTS), non-volatile switching involving phase change also known as memory switching, and electrochemical metallization (ECM) where chalcogenide is utilized as solid electrolyte based on its high ion conductivity, which establish themselves as key materials for optical storage as well as next-generation non-volatile memory application.

In this study, detailed studies and application of electrical switching behavior of chalcogenide thin films are presented. First, the mechanism of bipolar resistive switching (BRS) of amorphous $Ge_2Sb_2Te_5$ (GST) thin film sandwiched between inert electrodes (Ti and Pt) was examined. Typical bipolar resistive switching behavior with a high resistance ratio ($\sim 10^3$) and reliable switching characteristics was achieved. High-resolution transmission electron microscopy revealed the presence of conductive Te-filament bridging between the top and bottom electrodes through an amorphous GST matrix. The conduction mechanism analysis showed that the low-resistance state was semiconducting and dominated by band transport, whereas Poole-Frenkel conduction governed the carrier transport in the high-resistance state. Thus, the BRS behavior can be attributed to the formation and rupture of the

semiconducting Te bridge through the migration of the Te ions in the amorphous GST matrix under a high electric field. The Te ions are provided by the thin (~5nm) Te-rich layer formed at the bottom electrode interface.

Second, atomic layer deposition (ALD) of Ge-Sb-Te ternary and Ge-Sb-Se-Te quaternary thin films are studied for its possible application to selection device, especially for 3D vertical device utilizing high step coverage capability of ALD. The binary film of Ge-Te, Sb-Te and Sb-Se and its pseudo-binary and pseudo-ternary compounds, namely ternary Ge-Sb-Te and quaternary Ge-Sb-Se-Te films were deposited using $Ge(OEt)_4$, $Sb(OEt)_3$, $(Me_3Si)_2Te$ and $(Me_3Si)_2Se$ precursors and their self-limited saturation behavior were examined. The composition of pseudo-binary and pseudo-ternary compounds was confirmed to be consist of stoichiometric binary $GeTe_2$, Sb_2Te_3 and Sb_2Se_3. The various composition were tested by two-terminal MIM structure device to examine the effect of composition of each elements on switching parameter such as threshold field (F_{th}) as well as reliability characteristics such as cycling endurance. It was found that variation in Ge : Sb ratio leads to modulation of threshold field while cycling endurance was scarcely improved. On the other hands, increasing Se concentration resulted in great improvement in cycling endurance up to 10^5 cycle while threshold field was almost unaffected.

Third, the phase change behavior in multiple layer of the ultrathin GST film and consequent optical contrast and its application are presented. The multiple color appearance is basically based on large optical shift originated from the phase transition of multiple ultrathin GST films separated by the dielectric oxide barrier layer. The stacking of multiple layer of GST film and selective phase transition of each layer results in the modification of the strong interference effect and concomitant variable color appearance. It is shown that the reflective static color optical coating whose color can be switched is realized by stacking of more than one layer of ultrathin (< 10nm) GST on the colored substrate. The gradual shift in reflectance spectral position is resulted from the selective phase transition of GST layers and confirmed by optical transfer matrix simulation. Also, the feasibility of nanoscale image recording by static color switching is demonstrated by conductive atomic force microscopy.

Keywords: Chalcogenide materials, Electrical switching behavior, GeSbTe, Atomic layer deposition

Student Number: 2014-30213

Sijung Yoo

Table of Contents

Ph.D. DISSERTATION 1

Abstract i

Table of Contents iv

List of Figures vii

List of Tables xiv

List of Abbreviations xv

1. Introduction 1

1.1. Electrical switching behavior in chalcogenide 1

1.1.1. Phase change behavior 8

1.1.2. Solid electrolytic switching behavior 17

1.1.3. Ovonic threshold switching behavior 19

1.2. Objective and Chapter Overview 22

1.3. Bibliography 23

2. Bipolar resistive switching behavior of $Ge_2Sb_2Te_5$ thin films without phase change 27

2.1. Introduction 27

2.2. Experimental Procedures 32

2.3. Results and Discussions 37

2.4. Summary 55

2.5. Bibliography 56

3. Ovonic threshold switching behavior of Ge-Sb-Se-Te thin films deposited by Atomic layer deposition 60

3.1. Introduction 60

3.2. Experimental 64

3.3. Results and Discussions 71

3.4. Summary 96

3.5. Bibliography 97

4. Phase change behavior of multiple layer of ultrathin $Ge_2Sb_2Te_5$ film and its application to multi-color changeable optical coating 103

4.1. Introduction 103

4.2. Experimental 106

4.3. Results and Discussions 108

4.4. Summary 122

4.5. Bibliography 123

5. Conclusion 125

Curriculum Vitae 127

List of publications 130

Abstract (in Korean) 142

List of Figures

Fig 1-1. Comparison of Se and Si in amorphous structures (left), electron distributions of the atoms in solids (center), and energy levels in the isolated atoms and solids (right)[1]. 2

Fig 1-2. Typical current-voltage curve of a phase-change material[4]............. 4

Fig 1-3. Ternary phase diagram depicting different phase-change alloys, their year of discovery as a phase-change alloy and their use in different optical storage products[4]. 9

Fig 1-4. Typical schemes for phase transition of phase change materials in optical storage or non-volatile electronic memory[4]. 11

Fig 1-5. Schematic image of the crystal structure of the rocksalt-like phase of, for example, Ge2Sb2Te5 or Ge1Sb2Te4. Local distortions are not depicted[4]... 12

Fig 1-6. Formation energies for a) Ge and b) Sb vacancies for different concentrations of vacancies[15]. 14

Fig 1-7. Fragments of the local structure of GST around Ge atoms in the

crystalline (left) and amorphous (right) states[17]. 15

Fig 1-8. Schematics for the energy distribution of electrons in the amorphous chalcogenide film (a) at equilibrium (no applied electric field) and (b) under off-equilibrium conditions at high electric field[34]. . 20

Fig 2-1. (a) Schematic diagram of the device structure and measurement setup. (b) SEM image of the crossbar structure, with the inset showing a magnified image of the juction area. (c) XRD spectra clearly showing the amorphous nature of the deposited GST. 33

Fig 2-2. Bright-field TEM images of the Te-rich layer formed at the bottom electrode interface for (a) Ti/GST/Pt and (b) Pt/GST/Pt, repectively. (c) EDS line scan of the area marked with a yellow arrow in (b) clearly showing the presence of a Te-rich layer. 35

Fig 2-3. (a) BRS I-V characteristics of the Pt/GST/Pt and Ti/GST/Pt samples. The inset shows the compliance current dependence of the LRS current. (b) Dependence of the resistance on the active areas in both the high- and low-resistance states. 38

Fig 2-4. (a) Endurance characteristics of Pt/GST/Pt. (b) Cumulative probability

of resistance distribution of the cell. (c) Retention characteristic of the Pt/GST/Pt in both the HRS and LRS, measured at 85oC. (d) Extrapolation of the retention time measured at various temperatu res, indicating a 10-year retention capabilitiy at 85°C......... 41

Fig 2-5. (a) Cross-sectional STEM image of Pt/GST/Pt. (b) HRTEM ima ge of the filament region. (c) Fast Fourier Transformed micr ograph of the crytsalline filament, (d) corresponding simulate d diffraction pattern of tellurium for the [101] zone axis an d (e) corresponding Inverse Fast Fourier Transformed microg raph of the crytalline filament. 44

Fig 2-6. (a) Cross-sectional bright-field TEM image and (b) dark-field T EM image of the vicinity of the filament region for Ti/GST /Pt. The inset of (b) shows the selected area diffraction patt ern of the filament region. 46

Fig 2-7. (a) LogI-logV plot of the LRS measured at the temperature ran ge of 30-80°C. (b) Arrhenius plot of the LRS showing temp eature dependence and implying the semiconducting nature o

f the LRS. (c) Ln(J/E) versus $E^{1/2}$ plot of the HRS indicatin g that Poole-Frenkel conduction dominates HRS. The inset s hows the activation energy of the conduction calculated fro m (d) the Arrhenius plot of HRS. 49

Fig 2-8. Schematic representation of the bipolar resistive switching mech anism. (a) Pristine state. (b) SET operation. (c) LRS. (d) R ESET operation. (e) HRS. 51

Fig 3-1. Schematics of ALD apparatus utilized in the experiments. 65

Fig 3-2. Cycle configurations of the deposition process where Ch denotes chalcogenide precursors, namely $[(CH_3)_3Si]_2Te$ and $[(CH_3)_3Si]_2Se$. 67

Fig 3-3. Schematic diagram of the measurement system for pulse response measurement... 69

Fig 3-4. Schematic diagram of fabricated device using single hole patterned substrate with 2μm hole diameter... 70

Fig 3-5. Ternary diagram of various Ge-Sb-Te films deposited by combining $GeTe_2$ and Sb_2Te_3... 72

Fig 3-6. Saturation curve of the precursors for each binary films. 74

Fig 3-7. (a) Pseudo-ternary and (b) 3D quaternary diagram of deposited films with various compositions by combining $GeTe_2$, Sb_2Te_3, and Sb_2Se_3 binary films. 75

Fig 3-8. (a), (b), (c) Representative pulse response characteristics and (d) extracted current-voltage characteristics of threshold switching device measured in GST (Sb 8.4%) sample. 79

Fig 3-9. Threshold switching behaviors observed by pulse response and current-voltage curves of measured samples. 81

Fig 3-10. The cycling endurance characteristics with respect to $GeTe_2$: Sb_2Te_3 ratio. 83

Fig 3-11. (a) Threshold field and (b) optical bandgap with respect to $GeTe_2$: Sb_2Te_3 ratio. 84

Fig 3-12. (a) Measured and calculated current-voltage curve of GST samples and (b) fitted values regarding the distribution of localized state. 86

Fig 3-13. XRD results of annealed samples with various Se concentrations. 89

Fig 3-14. (a) The cycling endurance characteristics with respect to Se concentration and (b) enhanced endurance up to 10^5 by serially connected external resistor. 90

Fig 3-15. (a) Threshold field and (b) optical band with respect to Se concentration. 92

Fig 3-16. (a) Measured and calculated current-voltage curve of GSST samples and (b) fitted values regarding the distribution of localized state. 93

Fig 4-1. (a) Schematics depicting operation mechanism for selective crystallization and multiple optical state. (b) False color TEM image of the fabricated optical coating with two distinct GST layers separated by Ta_2O_5 which functions as a thermal/diffusion barrier. Only half of the image was colored for clarity. (c) Measured optical constants of GST film by spectroscopic ellipsometry. 109

Fig 4-2. Photograph of c/c samples annealed at 260℃ (a) & (b), α/c samples annealed at 210℃ (c) & (d), and α / α samples as-fabricated (e) &

(f). (a), (c), (e) has 150nm thick ITO layers while (b), (d), (f) has 200nm thick ITO layers...112

Fig 4-3. The measured reflectance spectra for (a) ITO 150nm samples and (b) ITO 200nm samples. Simulated reflectance spectra for (d) ITO 150nm and (e) 200nm, respectively. The measured ΔR values for (c) ITO 150nm and (f) 200nm...114

Fig 4-4. (a) Simulated reflectance spectra for multi-layer with all amorphous configuration. (b) ΔR between all amorphous and all crystalline configuration with increasing number of layers. (c) Simulated reflectance spectra for all crystalline configuration. (d) ΔR with respect to ITO spacer thickness variation for all crystalline configuration. 117

Fig 4-5. (a) Schematic of measurement setup for CAFM. (b) Optical microscope image (Scale bar: 10μm) and (c) CLSM image (Scale bar: 5μm) of recorded..119

List of Tables

Table 3-1. Detailed deposition conditions for the deposition process........... 66

Table 3-2. Process flow for device fabrication.. 70

Table 3-3. Determined precursor injection and purge time and deposition temperature according to the measured saturation curve for each precursors. 74

Table 3-4. Composition of deposited films with respect to cycle ratio.......... 75

Table 3-5. The composition and thickness of each samples in two experimental set. 77

List of Abbreviations

PCRAM	Phase-Change Random Access Memory
PCM	Phase-Change Material
ReRAM	Resistive switching Random Access Memory
ECM	Electro-Chemical Metallization
LRS	Low Resistance State
HRS	High Resistance State
OTS	Ovonic Threshold Switching
XRD	X-ray Diffraction
SEM	Scanning Electron Microscopy
XRF	X-ray Fluorescence
TEM	Transmission Electron Microscopy
HRTEM	High Resolution Transmission Electron Microscopy
FFT	Fast Fourier Transform
STEM	Scanning Transmission Electron Microscopy
EDS	Energy Dispersion Spectroscopy
FIB	Focused ion beam
BRS	Bipolar Resistive Switching
CBA	Cross Bar Array
MIT	Metal-Insulator Transition
MIEC	Mixed Ion-Electron Conductor
FAST	Field Assisted Super-linear Threshold
NDR	Negative Differential Resistance
PVD	Physical Vapor Deposition
CVD	Chemical vapor deposition

ALD	Atomic layer deposition
SE	Spectroscopic Ellipsometry

1. Introduction

1.1. Electrical switching behavior in chalcogenide

Chalcogenide materials are compounds consisting of at least one chalcogen element and one or more electropositive elements. Chalcogenide, which commonly refers sulfides, selenides, and tellurides rather than oxides, covalently bonded with other elements such as Ge, As, Sb in multicomponent systems are actively studied because of their prominent optical and electrical properties for various application.

The characteristic feature of chalcogenide mostly comes from its electronic configuration of chalcogen elements. The number of valence electrons in these atoms is 6 with a common outer electron configuration of s^2p^4. In the s^2p^4 configuration, the energy of the p-state is higher than the energy of the s-state, so the p-state is responsible of chemical bond. According to the Hund rule, the four electrons in the p state produce one filling orbital (p_z) and two half-filled orbitals (p_x and p_y). The paired p_z electrons, oftenly referred as lone pair electrons, form top of the valence band. Its non-bonding p electron feature designate the chalcogenide as a lone-pair electron semiconductor. Thus, its electronic structure is markedly different from that in the conventional sp^3 semiconductor such as Si or Ge. Also, the electrons in p_x and p_y orbitals produce covalent bonds with neighboring atoms. As a results, chalcogen atoms can form

	Structure	Electron distribution	Energy level atom solid
Se		p	p σ^* LP σ
Si		sp^3	p sp^3 s σ^* σ

Fig 1-1. Comparison of Se and Si in amorphous structures (left), electron distributions of the atoms in solids (center), and energy levels in the isolated atoms and solids (right)[1].

twofold bonding with neighboring atoms, which follows 8-N rule[2] where N=6 in this case.

Chalcogenide materials exhibit various kind of resistive switching behavior. Since S. Ovshinsky first reported reversible resistance switching phenomenon in chalcogenide materials in 1968[3], extensive study regarding the nature of electrical switching and its application to rewritable storage such as optical discs and electronic nonvolatile random access memories have been conducted[4-6]. Most widely known electrical switching phenomenon in chalcogenide is memory switching, which facilitate the application of chalcogenide to optically rewritable storage or non-volatile memory. These device application rely on the reversible change in the resistance and the optical reflectivity that results from the transition between crystalline and amorphous phase. The reversible changes could be rapidly and repeatedly induced by either an electrical pulse or a laser pulse. Rapid and precise phase change is the most crucial feature of this material class, making them focused for their application in the high-density electronic and optical memory fields in the past decades.

Among these applications, phase change random access memory (PCRAM) appears to be a highly promising non-volatile type of random access memory, which is the highly required feature of the next-generation computer system. The most extensively studied material for PCRAM application is the undoped

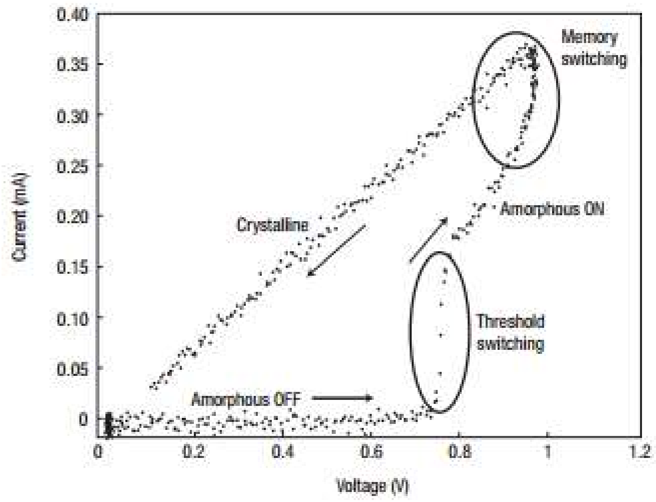

Fig 1-2. Typical current-voltage curve of a phase-change material[4].

or doped (with nitrogen, oxygen, silicon, etc.) $Ge_2Sb_2Te_5$ compound[6], the resistance of which could be switched via its amorphization and crystallization, mainly due to the Joule heating effect when intense/short and mild/long electrical pulses, respectively, are applied to it.

Resistance switching random access memory (ReRAM) is another class of feasible non-volatile random access memory, where the resistance switching (RS) effect of which could be mostly ascribed to the repeated formation and rupture of the local conduction path, typically called the conducting filament (CF)[7-8]. Modulation of the interfacial Schottky barrier according to the defect accumulation and depletion near one of the electrodes in a metal/insulator/metal (MIM) system could be another representative RS mechanism[9]. The CFs in many RS systems are usually composed of percolated defect paths, a distinctive conducting phase[10], or a metal bridge[11]. In the case of a nanoscale metal bridge that connects the two metal electrodes in the MIM system, the bridge is composed of an active metal, such as Cu and Ag, which comprises one of the two electrodes, whereas the other is an inert metal. This type of ReRAM is conventionally called an electrochemical metallization (ECM) cell[7]. Chalcogenides also play an important role as the electrolytes in the ECM cell. The binary sulfides and selenides as well as ternary glassy chalcogenide including telluride commonly adopted as fast transport channels. Because the operation of the ECM cell does not depend on the (local) melting and subsequent amorphization of the chalcogenides, it does not require an

excessively high reset (switching from a low-resistance state (LRS) to a high-resistance state (HRS)) current, which was the most significant problem in PCRAM.

Ovonic Threshold Switching (OTS) is another characteristic feature of chalcogenide glasses. It is an electric field-driven, repeatable and non-destructive resistive switching phenomenon that disappears when applied field is removed[12]. The current-voltage curve of OTS device measured with current sweep mode is generally S shaped switching rapidly from an initial high resistance OFF state into highly conductive dynaminc ON state once the applied voltage exceeds the threshold voltage, V_{th}[13]. OTS is essential for operation of PCRAM since it allows high current flow and subsequent Joule heating by reducing its resistance in amorphous (RESET) state. Also, strong non-linear and volatile current-voltage characteristic with simple two terminal structure makes it for an ideal access device for 1S1R crossbar array, commonly combined with oxide-based ReRAM or chalcogenide-based PCRAM[14].

In this thesis, three kind of electrical resistive switching behaviors of chalcogenide, especially for Ge-Sb-Te ternary based material system, are studied. First, based on detailed observation and characterization of polarity-dependent electrolyte switching behavior in $Ge_2Sb_2Te_5$ ternary system, new model that can account for the switching, different from conventional phase change mechanism or active metal ion migration, is established. Second, the

effect of compositional variation on the switching characteristics, especially for critical threshold field and cycling endurance characteristics was intensively studied for $GeTe_2$-Sb_2Te_3-Sb_2Se_3 pseudo-ternary system. Finally, phase change induced by electric field and consequent switching in optical properties and its application are presented.

1.1.1. Phase change behavior

Alloy of chalcogenide features good glass-forming ability and fast crystallization simultaneously, leading to rapid phase transition induced by heating and melt-quenching. The phase transition accompanies large change in optical and electrical properties. Owing to this fast phase transition, chalcogenide compounds are often called phase change materials (PCM) and have long been used as key materials in optical storage media (CD-ROM, DVD, Blu-ray disks). First material adopted is tellurium-based $Ge_{15}Te_{85}$ doped with Sb, S, and P. After, material systems with fast crystallization and distinc contrast between optical and electrical properties such as GeTe, $Ge_{11}Te_{60}Sn_4Au_{25}$ are discovered, which leads to the discovery of pseudobinary lying on tie line of GeTe-Sb_2Te_3 such as $Ge_1Sb_4Te_7$, $Ge_1Sb_2Te_4$, $Ge_2Sb_2Te_5$. Another materials system known to exhibit fast phase transition is doped Sb_2Te where Ag, In, Ge are chosen as dopant. The most widely known material among doped Sb2Te is $Ag_5In_5Sb_{60}Te_{30}$ (AIST), which is employed as rewritable optical storage such as DVD-RW. Aforementioned material systems as well as various kind of commercialized chalcogenide compounds are shown in Fig 1-3.

Among these phase change mateirals, compounds lying on tie line of GeTe-Sb_2Te_3 such as $Ge_1Sb_2Te_4$ and $Ge_2Sb_2Te_5$, also known as GST, has attracted wide attention since its characteristics is suitable for next-generation nonvolatile memory such as PcRAM. For pseudobinary of GeTe and Sb_2Te_3, increasing GeTe contents leads to enhanced stability of amorphous phase and

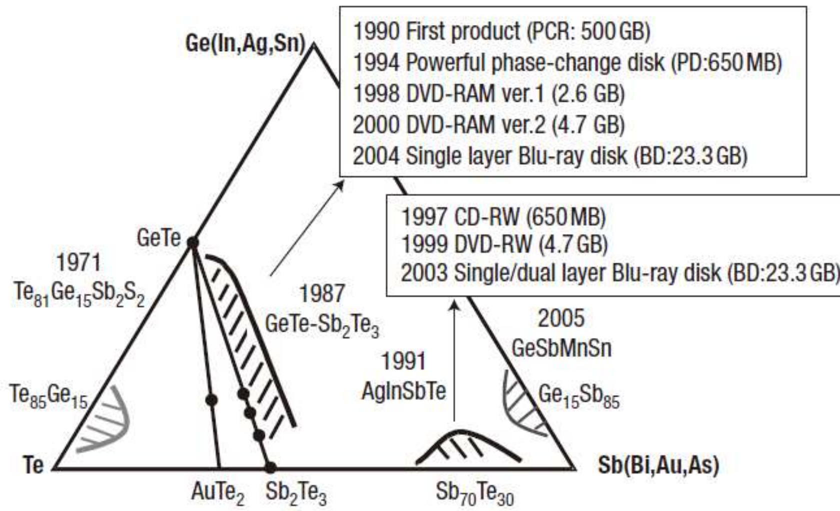

Fig 1-3. Ternary phase diagram depicting different phase-change alloys, their year of discovery as a phase-change alloy and their use in different optical storage products[4].

resultant slower crystallization speed while increasing Sb_2Te_3 contents results in faster crystallization speed and reduced amorphous stability, which results in spontaneous crystallization of amorphous phase. Thus, $Ge_2Sb_2Te_5$, which lies on the center of tie line, is considered the most suitable material for non-volatile memory application with its moderate and sufficient crystallization and amorphous stability.

The phase transition is usually induced by heating from laser irradiation in optical storage or applying electric pulse in non-volatile memory. Fig 1-4 shows typical procedure of phase transition. For the transition to amorphous phase , intense, short pulse is applied for melting and rapid cooling at rates higher than 10^9 K s^{-1}. To obtain crystal phase, long pulse with intermediate power is applied so that local heating raises the temperature above crystallization temperature.

The FCC structure of crystalline phase is depicted in Fig 1-5. GST has rock-salt structure where Te occupies one lattice while Ge and Sb occupies another lattice. In case of freuquently used phase change material such as $Ge_1Sb_2Te_4$ or $Ge_2Sb_2Te_5$, the ratio of Ge+Sb : Te is not unity so that Te lattice is fully occupied while Ge and Sb lattice inevitably has vacancy site. In ideal rock-salt structure each atoms must have sixfold bonding and hence they should have six valence electron. Since Ge has four valence electron and Sb has five, insufficient electrons are provided by afformentioned Te orbital facing towards

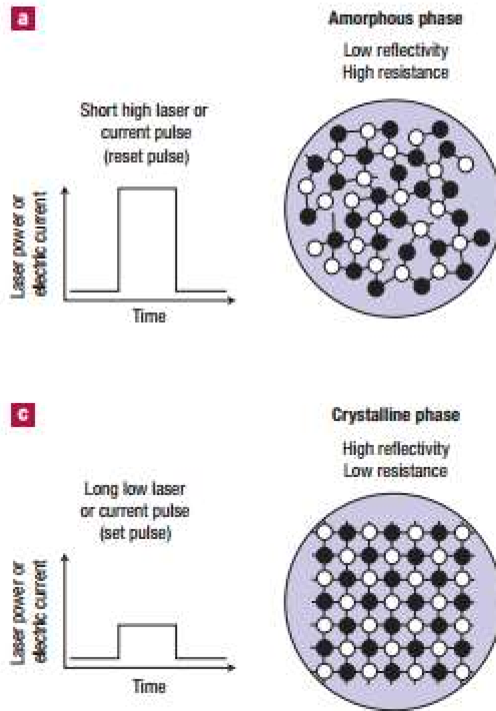

Fig 1-4. Typical schemes for phase transition of phase change materials in optical storage or non-volatile electronic memory[4].

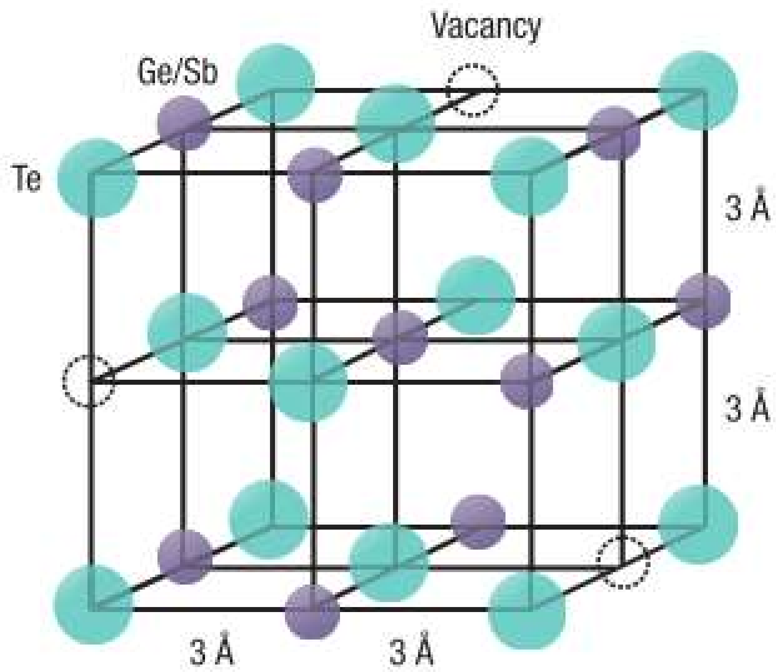

Fig 1-5. Schematic image of the crystal structure of the rocksalt-like phase of, for example, Ge2Sb2Te5 or Ge1Sb2Te4. Local distortions are not depicted[4].

vacancy site. From this point of view, the vacancy site in GST is considered to be inherent and essential. This is confirmed by first-principle calculation[15] shown in Fig 1-6 claiming that a certain level of vacancy concentration rather lowers the formation energy level down to negative value and stabilize the structure.

Along with high concentration of vacancy, considerable distortion in crystal lattice is another feature of GST. Extended X-ray Absorption Fine Structure (EXAFS) reveals that the crystal structure of GST has considerable local distortion as well as the difference in atomic arrangement between crystalline and amorphous phase[16].

Amorphous phase is characterized by the lack of long-range periodical orderness while short-range ordering maintain similar arrangement with crystalline phase. According to EXAFS by Kolobov et al[17], Ge atom forms tetrahedral bonding in amorphous phase while it forms octahedral bonding in crystalline phase as shown in Fig 1-7. The transition of atomic bonding between amorphous and crystalline is named ‘umbrella flip’ and the fast transition of phase change material can be attributed to this transition of atomic bonding which achieve structural change effectively without breaking strong covalent bonding. However, it is still controversial whether four-fold Ge environment in amorphous phase is tetrahedral or distorted octahedral (four-fold coordinated) configuration due to disagreement between various research regarding

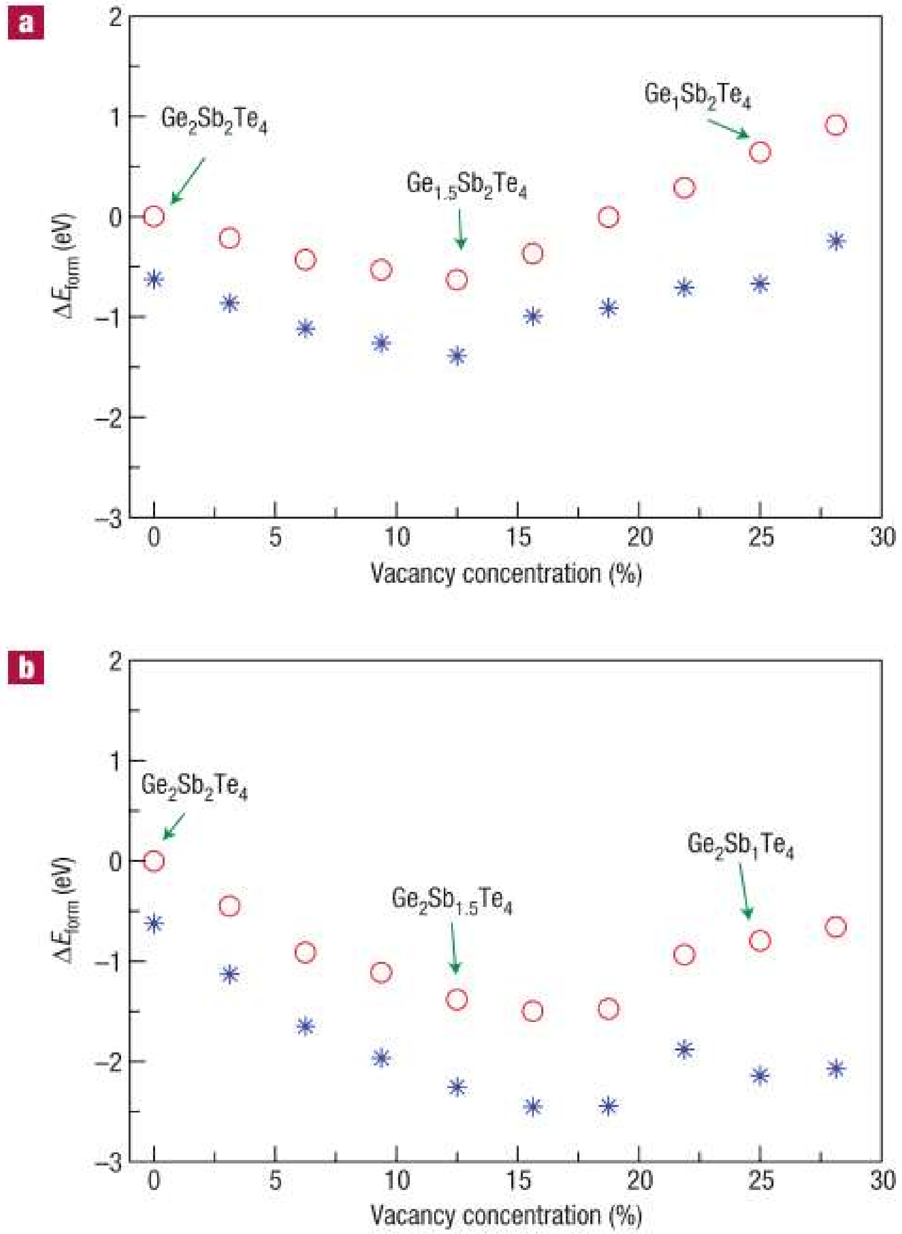

Fig 1-6. Formation energies for a) Ge and b) Sb vacancies for different concentrations of vacancies[15].

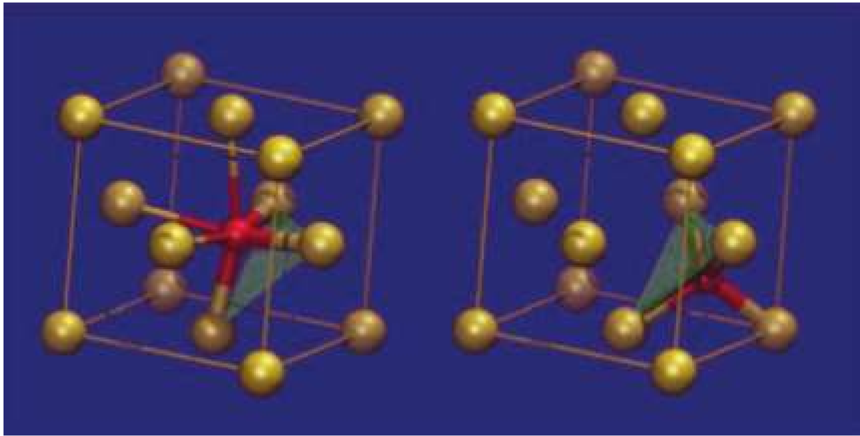

Fig 1-7. Fragments of the local structure of GST around Ge atoms in the crystalline (left) and amorphous (right) states[17].

modelling simulation. While, average number of neighboring atoms of Sb and Te are still in debate concerning the coordination number is how close to 8-N rule.

1.1.2. Solid electrolytic switching behavior

Electric field polarity-dependent resistance switching, which is differ from phase change mechanism that is induced by polarity-independent Joule heating, has been reported in some chalcogenide[18-23]. The solid electrolyte characteristics of chalcogenide and high ionic conductivity enabled this kind of switching, which is called ion / electrolytic switching. The resistance switching is originated from forming a filamentary conduction path between the electrodes in the chalcogenide medium by one polarity and rupture of previously formed conductive filament by reverse polarity. Various materials systems including Ag-saturated chalcogenide containing Ag - S, [18-19] Ag - Ge - Se, [11, 20] Ag - Ge - Te[22], , Ag - In - Sb - Te[23] has been demonstrated. This kind of switching is more appealing for memory applications than phase change-dependent switching by the following points. Firstly it requires lower voltage for switching and secondly it does not accompany significant change of structure and the effects such as compsitional separation or void formations can be prohibited, providing enhanced reliability. Recent study by Pandian et al. reported polarity-dependent switching in Ag- or Cu-free Ge-Sb-Te system[24-25]. The switching was attributed to the formation and rupture of Sb filament under application of voltage in $Ge_2Sb_{2+x}Te_5$ having excss Sb with respect to the stoichiometric composition $Ge_2Sb_2Te_5$. It was shown that nonuniform distribution of elements, excess Sb in this case, plays a crucial role for this kind of switching. Similar switching behaviors in non-doped $Ge_2Sb_2Te_5$

in inert electrode system were also reported by Woo et al., which also can be attributed to formation and rupture of filament that is originated from segregation of excess elements[26]. Recent study by Ciocchini et al. reported the polarity-dependent switching in amorphous GST with stoichiometric composition, which can be attributed to local depletion of chemical species by ion migration in the solid state induced by elevated temperature and high electric field[27].

1.1.3. Ovonic threshold switching behavior

Ovonic threshold switching refers increase in conductivity when high field is applied observed for many chalcogenide materials in their amorphous phase showing negative differential resistance (NDR) behvaior. Various theoretical models are suggested to explain the threshold switching phenomeon. Thermally induced instabilities[28], impact ionization and Shockely-Hall-Read recombination[29-30], polaron instabilities[31] and field induced crystallization[32-33] have been proposed. Recently, Ielmini el al. suggested that threshold switching can be attributed to an instability of voltage-current due to non-equilibrium distribution of electron excited by high fields application[34]. The noneqilibrium condition and resulting threshold switching can be explained by modified Poole-Frenkel conduction, or oftenly referred as trap-limited conduction[12], schematically shown in Fig 1-8. As applied field increases, barrier height for electron hopping decreases, which results in dramatically increases conductivity. This model has successfully expalined threshold switching behavior in accordance with experimentally observed current-voltage characteristics.

Current density J in amorphous chalcogenide can be expressed by so-called thermally assisted hopping or trap-limited conduction mechanism

$$J = 2qN_t \frac{\Delta z}{\tau_0} e^{-\frac{E'_c - E_{F0}}{kT}} \sinh\left(\frac{qF\Delta z}{2kT}\right)$$

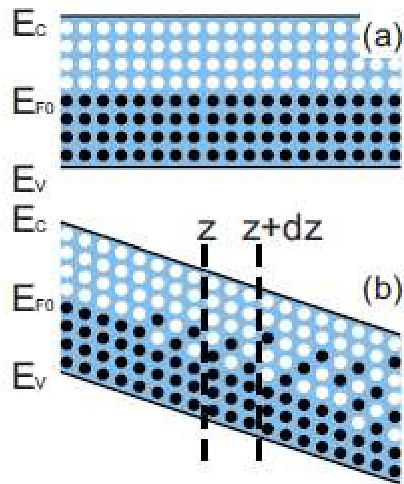

Fig 1-8. Schematics for the energy distribution of electrons in the amorphous chalcogenide film (a) at equilibrium (no applied electric field) and (b) under off-equilibrium conditions at high electric field[34].

where q is the elementary charge, N_T (cm^{-3}) is the density of traps between E_{F0} and E'_C and Δz is the average distance between localized states.

Nonequillibrium condition of electron distribution can be expressed by the average excess energy for electrons at one point z along the transport direction and it can be given by the difference between the quasi-Fermi level, E_F. The balance between energy gain and loss by electric field and inelastic scattering, respectively, can be expressed by

$$\frac{dE_F}{dz} = qF - \frac{qn_T}{J}\frac{E_F - E_{F0}}{\tau_{rel}}$$

where E_F and E_{F0} is quasi-Fermi level and equilibrium Fermi level, respectively and n_T is the trapped electron concentration where it is assumed that the trap distribution N_T is uniform in energy.

Combining two equations by replacing the equilibrium Fermi level E_{F0} in first equation by quasi-Fermi level E_F allows to describe nonequilibrium condutions at threshold switching. By this model, threshold switching can be explained by the collaps of the elctric field as a result of non-equilibrium, high-energy distribution of trapped electrons.

1.2. Objective and Chapter Overview

The objective of this dissertation is focused on the analysis of electrical switching behavior of chalcogenide films including Ge and Sb and its application.

Chapter 2 covers bipolar resistive switching behavior without obvious phase change in amorphous $Ge_2Sb_2Te_5$ thin film, which also known as conventional material for Phase Change Memory (PCM).

Chapter 3 covers Ovonic Threshold Switching behavior of Ge-Sb-Te ternary and Ge-Sb-Se-Te quaternary films. The effect of composition on switching parameter and reliability are analyzed.

Chapter 4 covers electrically-induced phase change behavior in ultrathin (<10 nm) $Ge_2Sb_2Te_5$ films and change in reflection spectrum as well as its application on optical storage and nanoscale display is examined.

Finally, in chapter 5, the conclusion of the dissertation is presented.

1.3. Bibliography

1. Tanaka, K.; Shimakawa, K., *Amorphous chalcogenide semiconductors and related materials*. Springer Science & Business Media.(2011)

2. Mott, N. F.; Davis, E. A., *Electronic processes in non-crystalline materials*. OUP Oxford.(2012)

3. Ovshinsky, S. R., *Physical Review Letters* **21** (20), 1450-1453 (1968)

4. Wuttig, M.; Yamada, N., *Nat Mater* **6** (11), 824-832 (2007)

5. Burr, G. W.; Breitwisch, M. J.; Franceschini, M.; Garetto, D.; Gopalakrishnan, K.; Jackson, B.; Kurdi, B.; Lam, C.; Lastras, L. A.; Padilla, A.; Rajendran, B.; Raoux, S.; Shenoy, R. S., *Journal of Vacuum Science & Technology B* **28** (2), 223-262 (2010)

6. Raoux, S.; Wełnic, W.; Ielmini, D., *Chemical Reviews* **110** (1), 240-267 (2010)

7. Waser, R.; Dittmann, R.; Staikov, G.; Szot, K., *Advanced Materials* **21** (25-26), 2632-2663 (2009)

8. Waser, R.; Aono, M., *Nat Mater* **6** (11), 833-840 (2007)

9. Yang, J. J.; Pickett, M. D.; Li, X.; OhlbergDouglas, A. A.; Stewart, D. R.; Williams, R. S., Memristive switching mechanism for metal//oxide//metal nanodevices. In *Nat Nano*, Nature Publishing Group: 2008; Vol. 3, pp 429-433.

10. Kwon, D.-H.; Kim, K. M.; Jang, J. H.; Jeon, J. M.; Lee, M. H.; Kim, G. H.; Li, X.-S.; Park, G.-S.; Lee, B.; Han, S.; Kim, M.; Hwang, C. S., *Nat Nano* **5** (2), 148-153 (2010)

11. Kozicki, M. N.; Mira, P.; Mitkova, M., *Nanotechnology, IEEE Transactions on* **4** (3), 331-338 (2005)

12. Ielmini, D.; Zhang, Y., *Journal of Applied Physics* **102** (5), 054517 (2007)

13. Burr, G. W.; Shenoy, R. S.; Virwani, K.; Narayanan, P.; Padilla, A.; Kurdi, B.; Hwang, H., *Journal of Vacuum Science & Technology B, Nanotechnology and Microelectronics: Materials, Processing, Measurement, and Phenomena* **32** (4), 040802 (2014)

14. Lee, J. H.; Kim, G. H.; Ahn, Y. B.; Park, J. W.; Ryu, S. W.; Hwang, C. S.; Kim, H. J., *Applied Physics Letters* **100** (12), 123505 (2012)

15. Wuttig, M.; Lusebrink, D.; Wamwangi, D.; Welnic, W.; Gillesen, M.; Dronskowski, R., *Nat Mater* **6** (2), 122-128 (2007)

16. Matsunaga, T.; Yamada, N., *Proc. 16th Symp. PCOS2004 1–4*, (2005)

17. Kolobov, A. V.; Fons, P.; Frenkel, A. I.; Ankudinov, A. L.; Tominaga, J.; Uruga, T., *Nat Mater* **3** (10), 703-708 (2004)

18. Hirose, Y.; Hirose, H., *Journal of Applied Physics* **47** (6), 2767-2772 (1976)

19. Terabe, K.; Nakayama, T.; Hasegawa, T.; Aono, M., *Journal of Applied Physics* **91** (12), 10110-10114 (2002)

20. Kozicki, M. N.; Mitkova, M.; Park, M.; Balakrishnan, M.; Gopalan, C., *Superlattices and Microstructures* **34** (3–6), 459-465 (2003)

21. Kozicki, M. N.; Mira, P.; Mitkova, M., *IEEE Transactions on Nanotechnology* **4** (3), 331-338 (2005)

22. Kim, C.-J.; Yoon, S.-G.; Choi, K.-J.; Ryu, S.-O.; Yoon, S.-M.; Lee, N.-Y.; Yu, B.-G., *Journal of Vacuum Science & Technology B: Microelectronics and Nanometer Structures Processing, Measurement, and Phenomena* **24** (2), 721-724 (2006)

23. You, Y.; Hayato, S.; Sumio, H., *Japanese Journal of Applied Physics* **45** (6R), 4951 (2006)

24. Pandian, R.; Kooi, B. J.; Oosthoek, J. L. M.; Dool, P. v. d.; Palasantzas, G.; Pauza, A., *Applied Physics Letters* **95** (25), 252109 (2009)

25. Pandian, R.; Kooi, B. J.; Palasantzas, G.; De Hosson, J. T. M.; Pauza, A., *Advanced Materials* **19** (24), 4431-4437 (2007)

26. Woo, J.; Jung, S.; Siddik, M.; Cha, E.; Sadaf, S. M.; Hwang, H., *Applied Physics Letters* **99** (16), 162109 (2011)

27. Ciocchini, N.; Laudato, M.; Boniardi, M.; Varesi, E.; Fantini, P.; Lacaita, A. L.; Ielmini, D., *Scientific Reports* **6**, 29162 (2016)

28. Warren, A. C., *IEEE Transactions on Electron Devices* **20** (2),

123-131 (1973)

29. Adler, D.; Shur, M. S.; Silver, M.; Ovshinsky, S. R., *Journal of Applied Physics* **51** (6), 3289-3309 (1980)

30. Pirovano, A.; Lacaita, A. L.; Benvenuti, A.; Pellizzer, F.; Bez, R., *IEEE Transactions on Electron Devices* **51** (3), 452-459 (2004)

31. Emin, D., *Physical Review B* **74** (3), 035206 (2006)

32. Karpov, I. V.; Mitra, M.; Kau, D.; Spadini, G.; Kryukov, Y. A.; Karpov, V. G., *Applied Physics Letters* **92** (17), 173501 (2008)

33. Karpov, I. V.; Mitra, M.; Kau, D.; Spadini, G.; Kryukov, Y. A.; Karpov, V. G., *Journal of Applied Physics* **102** (12), 124503 (2007)

34. Ielmini, D., *Physical Review B* **78** (3), 035308 (2008)

2. Bipolar resistive switching behavior of $Ge_2Sb_2Te_5$ thin films without phase change

2.1. Introduction

Alloys and compounds composed of Ge, Sb, and Te are the major materials of phase-change random access memory (PCRAM) and optically rewritable discs [1]. These device applications rely on the reversible change in the resistance and the optical reflectivity, respectively, of the chalcogenides, depending on the phases of the material, i.e., crystalline or amorphous [2-4]. The reversible changes could be rapidly and repeatedly induced by either an electrical pulse, for PCRAM, or a laser pulse, for optical discs. Rapid and precise phase change is the most crucial feature of this material class, making them focused for their application in the high-density electronic and optical memory fields in the past decades. Among these applications, PCRAM appears to be a highly promising non-volatile type of random access memory, which is the highly required feature of the next-generation computer system. The most extensively studied material for PCRAM application is the undoped or doped (with nitrogen, oxygen, silicon, etc.) $Ge_2Sb_2Te_5$ compound, the resistance of which could be switched via its amorphization and crystallization, mainly due to the Joule heating effect when intense/short and mild/long electrical pulses, respectively, are applied to it [5]. The resistivity of an amorphous material is 10^3-10^4 times higher than that of a crystalline material. However, the mass-

production of PCRAM using the $Ge_2Sb_2Te_5$ compound as the active memory element has been deterred mainly due to the too high current needed to amorphize the material, which is higher than the current handling capability of the cell selector (transistor or diode) [6].

Resistance switching random access memory (ReRAM) is another class of feasible non-volatile random access memory, where the resistance switching (RS) effect of which could be mostly ascribed to the repeated formation and rupture of the local conduction path, typically called the conducting filament (CF) [7-9]. Modulation of the interfacial Schottky barrier according to the defect accumulation and depletion near one of the electrodes in a metal/insulator/metal (MIM) system could be another representative RS mechanism [10]. The CFs in many RS systems are usually composed of percolated defect paths, a distinctive conducting phase11, or a metal bridge [12]. In the case of a nanoscale metal bridge that connects the two metal electrodes in the MIM system, the bridge is composed of an active metal, such as Cu and Ag, which comprises one of the two electrodes, whereas the other is an inert metal. This type of ReRAM is conventionally called an electrochemical metallization (ECM) cell [8]. Chalcogenides also play an important role as the electrolytes in the ECM cell. Because the operation of the ECM cell does not depend on the (local) melting and subsequent amorphization of the chalcogenides, it does not require an excessively high reset (switching from a low-resistance state (LRS) to a high-resistance state (HRS)) current, which was

the most significant problem in PCRAM. Nevertheless, the adoption of Ag or Cu as the active metallic element could pose a problem with contamination control in mass-production lines for semiconductor device fabrication, although Cu wiring in the back-end-of-the-line process is already in mass production. However, in the case of Cu metallization, the electric-field-induced Cu migration is completely suppressed. Adoption of actively migrating metallic species is always a concern for high reliability. According to this concern, recent studies reported on the chalcogenide-based ReRAM cell, wherein the formation and rupture of the Sb-based CF formed inside the Sb-rich crystalline Ge-Sb-Te alloys are responsible for the repeated switching [13-16]. Sb is a cation-like species in Ge-Sb-Te alloys, so it can be ionized and migrated according to the electric field under a sufficiently high electric bias condition, which is in a similar fashion as ECM. However, the problem of the high consumption of switching power persisted in this case, which could be ascribed to the relatively inactive migration of Sb.

Meanwhile, it is considered that Te could be similarly utilized with opposite polarity according to the bias direction, because Te is an anion-like species in the same material. Te has a much lower melting point than Sb (449.5°C vs. 630.6°C, respectively), and Te also has semiconducting properties, so CF formation of Te could be considered another viable method of introducing the fast and low-power-consuming ReRAM from the Ge-Sb-Te alloy system. Another critical aspect of the Ge-Sb-Te alloy system is its

amorphousness when it is as-prepared using the ca. sputtering process, as in this study, which could be a critical way to ensure the uniformity of the switching parameters, due to the structural homogeneity in the atomic scale, unlike in a poly-crystalline material. The structural stability of the chalcogenides adopted in the ReRAM cell is another critical aspect, because the material is under serious thermal, electrical, and even mechanical stresses during the device fabrication and repeated switching operation. The thermochemical studies of the Ge-Sb-Te alloy system with various chemical compositions revealed that the stoichiometric compound without vacancy sites in the structure (such as $Ge_2Sb_2Te_4$ in the rock-salt structure) is energetically unstable with respect to the $Ge_2Sb_2Te_5$ compound, wherein 20% of the cation sites is occupied with vacancy, which is normally very unstable in other materials [17]. $Ge_1Sb_2Te_4$ is another example of a material with such chemical stability and with a very high vacancy concentration. In contrast, a material with an excessively high vacancy concentration, such as $Ge_2Sb_2Te_7$, the cation site vacancy concentration of which is as high as 40%, is also unstable, and may be decomposed to $Ge_2Sb_2Te_5$ and Te during the device fabrication or repeated operation. The significant segregation of Te might be detrimental to its stable reset operation.

Therefore, this study carefully examined the RS behavior, in crossbar geometry, of an amorphous $Ge_2Sb_2Te_5$ (GST) thin film deposited via the sputtering process at room temperature to ensure its amorphous structure. All

the subsequent processes for the crossbar pattern fabrication were carefully controlled to prevent the crystallization of the GST layer. The two different types of inert electrode materials (Ti and Pt) were adopted to ensure that the RS effect in these memory cells would not be related to the ECM effect, but to the Te filament formation and rupture. Detailed structural and electrical characterizations were performed to confirm that the RS mechanism is related to the Te CF formation and rupture, and not to the overall structural change between the amorphous and crystalline phases of the GST material, nor to the electrode metal migration. It was found that the interface region between GST film and bottom Pt interface region became enriched with Te, which provided the system with electrochemical asymmetry and Te source for Te CF formation. When the sample was tested using a pulse switching method to induce the usual PCRAM-type switching, it was not possible. This can be understood from the much higher required current (75 A, calculated from the reported reset current density value [18] for a device with a similar geometry) than the maximum current of the pulse switching setup (~1 A) for the reset of crystalline $Ge_2Sb_2Te_5$ even with the smallest electrode area in this work (16 μm^2). This also suggests that the usual phase change mechanism cannot account for the RS phenomenon observed in this case.

2.2. Experimental Procedures

MIM-structured crossbar-type devices with various junction areas (4×4, 6×6, 8×8, and 10×10 μm^2) were fabricated on a wet oxidized Si substrate. A 50nm-thick Pt bottom electrode was deposited using the electron beam evaporation method and patterned into the line patterns via conventional photolithography and the lift-off process. A $Ge_2Sb_2Te_5$ film was deposited via DC sputtering from a stoichiometric $Ge_2Sb_2Te_5$ target. After the GST film deposition, a 40nm-thick top electrode was fabricated using the same process as that for the bottom electrodes. Two different metals (Ti and Pt) were used for the top electrode. A Pt layer was deposited on the Ti top electrode in a single batch without breaking the vacuum to prevent surface oxidation of Ti. The Ti/$Ge_2Sb_2Te_5$/Pt (denoted as Ti/GST/Pt) and Pt/$Ge_2Sb_2Te_5$/Pt (denoted as Pt/GST/Pt) structures were used to measure the electrical characteristics. During the entire fabrication process, each step was carefully controlled to avoid any heating or chemical damaging/etching effect on the GST film to prevent the crystallization and any other form of unintended manipulation of the as-deposited phase of the film. Fig 2-1 (a) and (b), and the inset of (b), show the schematic of the device structure, the scanning electron microscopy (SEM, Hitachi, S-4800) image of the fabricated crossbar-type devices, and the magnified image of the active area, respectively. The structural characterization of the GST layer using X-ray diffraction (XRD, PANalytical, X'Pert PRO MPD) revealed the amorphous nature of the GST film, as shown in Fig 2-1 (c). The film composition was

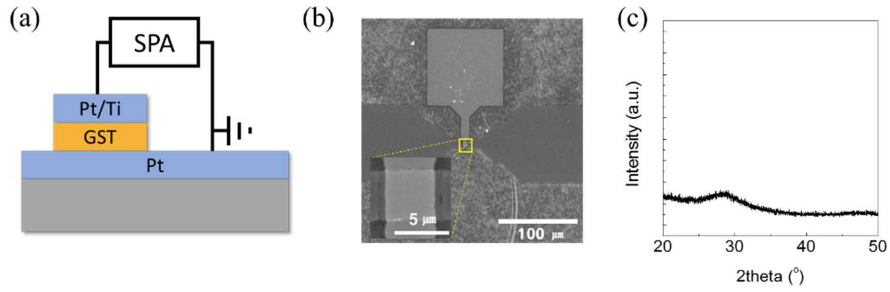

Fig 2-1. (a) Schematic diagram of the device structure and measurement setup. (b) SEM image of the crossbar structure, with the inset showing a magnified image of the juction area. (c) XRD spectra clearly showing the amorphous nature of the deposited GST.

confirmed to be close to Ge:Sb:Te = 2:2:5 (Ge, 22.2 %; Sb, 23.9%; and Te, 53.9%), using X-ray fluorescence spectroscopy (XRF, Thermo Scientific, ALR Quant'X EDXRF). The electrical characterization was performed with a semiconductor parameter analyzer (SPA, Hewlett-Packard, HP 4145B) in the DC current - voltage (I-V) sweep mode. During the electrical measurement, the electric bias was applied to the top electrode, and the bottom electrode was grounded. Also, the current was limited by the compliance current of the control circuit to prevent the crystallization of the GST matrix. A 200kV transmission electron microscope (TEM, JEOL, and JEM-2100F) was used for high-resolution transmission electron microscopy (HRTEM) / scanning transmission electron microscopy (STEM) imaging, and energy-dispersive spectroscopy (EDS) was used for the chemical characterization of the pristine and conducting filament region. The TEM sample was fabricated with a focused ion beam (FIB, FEI Helios 650) from the repeatedly switched cell.

Fig 2-2 (a) and (b) show the bright-field TEM images of the pristine regions near bottom electrode of Ti/GST/Pt and Pt/GST/Pt, respectively. A thin, bright layer is located between the GST and the bottom electrode in both samples. An EDS line scan along the yellow arrow in Fig 2-2 (b) confirmed this as the Te-rich layer [denoted with red dash lines in Fig 2-2 (c)]. This Te-rich layer plays a critical role for the overall asymmetric bipolar resistive switching (BRS) behavior by providing the active ionic species, Te anion in this case.

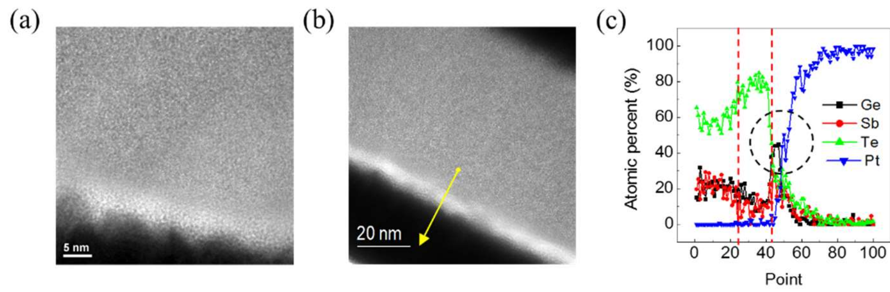

Fig 2-2. Bright-field TEM images of the Te-rich layer formed at the bottom electrode interface for (a) Ti/GST/Pt and (b) Pt/GST/Pt, repectively. (c) EDS line scan of the area marked with a yellow arrow in (b) clearly showing the presence of a Te-rich layer.

Note that a sharp, narrow Ge peak was observed between the Te-rich layer and the Pt electrode [denoted with a black dashed circle in Fig 2-2 (c)]. One possible scenario for the formation of the Te-rich layer involves the intermixing of Ge with Pt to leave a Te-rich (Ge-deficient) layer behind, possibly due to the difference between the standard free energy of formation of Pt-Ge (-101.07 kJ/mol[19, 20]) and that of Pt-Te (-75.21 kJ/mol[21]). The formation of the Pt-Ge compound is deemed unlikely under the GST film deposition at room temperature. However, the bombardment of highly energetic sputtered atoms can supply enough energy to overcome the high energy barrier during the deposition, and the formation of this compound can be reasonably expected. Therefore, the Te-rich layer could be initiated near the bottom Pt electrode. In contrast, the formation of such layer between GST and the top electrode is highly unlikely because evaporated Pt atoms are much less energetic than sputtered atoms. The formation of the Te-rich layer at the bottom electrode interface during the fabrication process leads to the asymmetry of the structure of the system, which could induce asymmetric switching behavior for such nominally symmetrical structure as Pt/GST/Pt.

2.3. Results and Discussions

The typical BRS behaviors of the two samples are shown in Fig 2-3 (a), which were obtained from the memory cells with a 4×4μm^2 area. The pristine sample showed highly insulating behavior, so the sample required an electro-formation step to allow observation of the BRS behavior. After the initial positive sweep up to the electroforming voltage (denoted with Arrow 1), the current suddenly increased to the compliance value, and the device was switched to the low-resistance state (LRS). At this state, the device maintains its resistance during the backward sweep, so it shows a high current value under both positive and negative biases (denoted with Arrow 2). The subsequent negative sweep switched the device into the high-resistance state (HRS), and the current suddenly dropped to a very low value (RESET, denoted with Arrow 3). The current level of the HRS was identical to that of the pristine state, which remained low during the forward sweep until the voltage reached a certain value. At this voltage, the device was switched again to the LRS (SET) (denoted with Arrow 4). The set current level (0.5 mA) is much higher than other ECM cells based on the migration of Ag or Cu (~25 μA) [8]. This could be due to the generally larger conducting filament diameter (could be as large as ~10 – 20 nm, see Fig 2-5) compared with the much smaller value of general ECM involving Ag or Cu (< ~ 5 nm), which could be attributed to the relatively long application of set bias during the set sweep as can be seen in Fig 2-3 (a). In the inset in Fig 2-3 (a), the LRS current shows a linear increase with respect to the

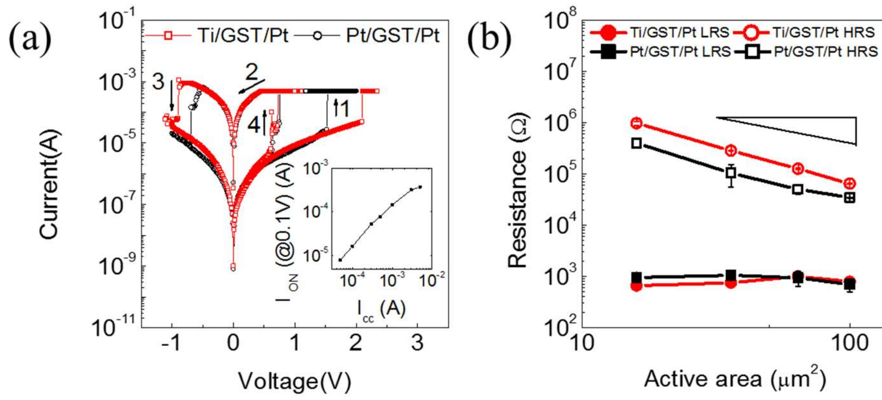

Fig 2-3. (a) BRS I-V characteristics of the Pt/GST/Pt and Ti/GST/Pt samples. The inset shows the compliance current dependence of the LRS current. (b) Dependence of the resistance on the active areas in both the high- and low-resistance states.

compliance current increase. This can be used to achieve multi-level resistance values by adjusting the compliance current. Notably, the RESET behavior in this case is far from the conventional switching behavior of GST that involves phase change, where RESET is induced by amorphization via melt-quenching. This can be achieved only by an extremely short electric current pulse for fast melting and subsequent quenching, with a sufficiently high current density (~10^7 A cm^{-2}) [18]. Since the current-voltage characteristics were obtained in the DC sweep mode with a much lower current density, the RESET process obviously does not involve amorphization.

It is noteworthy that the SET (and electroforming) process was possible only under a positive bias, whereas the RESET process was possible only under a negative bias for both samples. Any attempt to yield a negative SET or a positive RESET failed to switch the resistance state. Especially, the electroforming process was never successfully implemented under the negative bias even after several attempts, which means this switching behavior is polarity-dependent. This polarity dependence can also prove that resistive switching does not involve phase change, since phase change is achieved by the Joule heating effect, and, thus, should be polarity-independent. As shown in Fig 2-2, such polarity-dependent BRS behavior was originated from the difference between the top and bottom electrode interfaces that resulted from the sputter-deposition of the GST layer on the Pt bottom electrode for both samples. In other words, nominally symmetrical MIM structure (GST

sandwiched by Pt deposited using the same deposition method) is actually not symmetric due to the unexpected effect was induced during the fabrication, which caused the asymmetry of the structure.

Fig 2-3 (b) shows the resistance change in both the high- and low-resistance states with respect to the active electrode junction area for the two samples. The HRS current shows linear dependence on the active electrode area, whereas the LRS current remained almost constant over the entire electrode area range for both types of samples. When the resistive switching has a filamentary nature, the magnitude of the LRS current should be independent of the device area [8]. This suggests that the bipolar switching behavior of the Pt/GST/Pt system is due to the formation and rupture of the localized conducting filament. Accordingly, the LRS current increase with respect to the compliance current increase shown in the inset of Fig 2-3 (a) can be understood in the filamentary switching model. That is, a stronger and less resistive filament is formed, or more filaments are formed, by a higher compliance current. Also, further reduction of the electrode area will further improve the ON/OFF ratio, since R_{OFF} is proportional to the active area, but R_{ON} is not.

The reliability characteristics were examined for both the Ti/GST/Pt and Pt/GST/Pt samples. Since the two samples show almost identical reliability characteristics, the results for Pt/GST/Pt were selected and discussed in detail. As can be seen in Fig 2-4 (a), stable switching endurance in the DC sweep mode

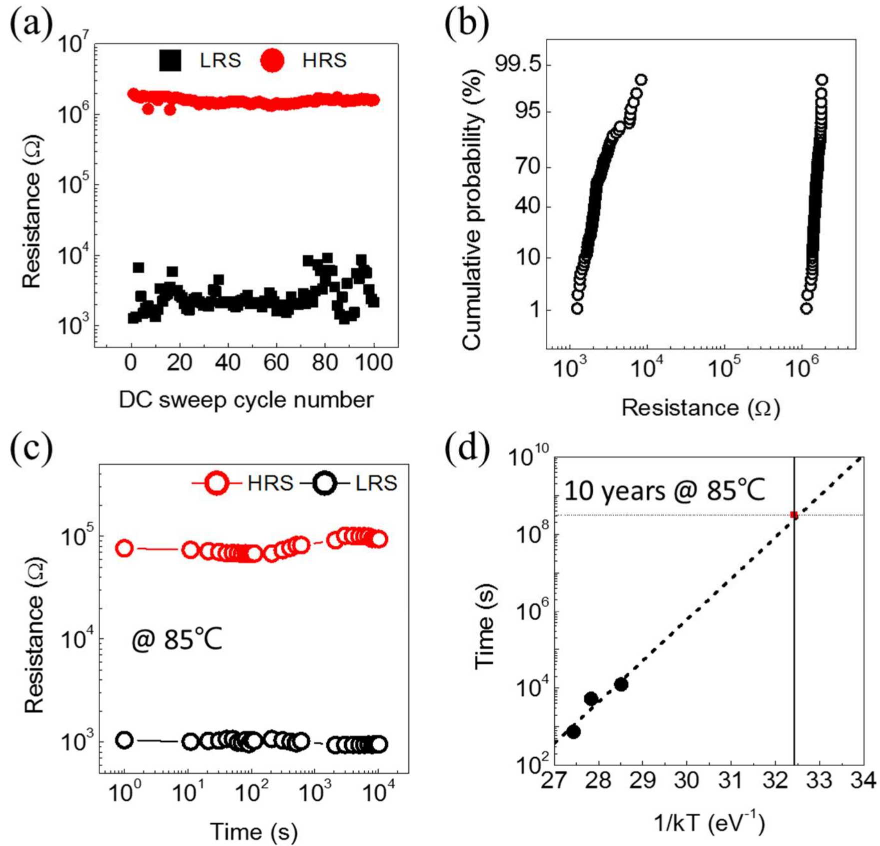

Fig 2-4. (a) Endurance characteristics of Pt/GST/Pt. (b) Cumulative probability of resistance distribution of the cell. (c) Retention characteristic of the Pt/GST/Pt in both the HRS and LRS, measured at 85oC. (d) Extrapolation of the retention time measured at various temperatures, indicating a 10-year retention capabilitiy at 85°C.

with at least 100 cycles was achieved. The resistance ratio of the HRS to the LRS was more than 100. The resistance of the HRS showed excellent uniformity, whereas the resistance of the LRS showed a slight fluctuation from 10^3 Ω to 10^4 Ω as shown in Fig 2-4 (b). Fig 2-4 (c) shows stable retention characteristics up to 10^4 s at 85°C, without considerable resistance degradation. To test the ultimate retention time of the LRS, the retention time (the time when the resistance ratio decreased to 10) was measured at higher temperatures (130-150°C), and the results were plotted according to the Arrhenius form (Fig 2-4 (d)). The best-linear-fitting of the data according to the general Arrhenius equation revealed an activation energy of 1.07 eV, which is high enough to withstand the thermal disturbance effect in the operating temperature range. The extrapolation of the best-linear-fitted graph shows an excellent retention time, which guarantees data retention up to 10 years at 85°C.

The polarity-dependent and filamentary nature of the switching is the characteristic feature of the ECM effect. Actually, binary or ternary glasses of chalcogenides, such as selenides or tellurides, are the frequently adopted solid electrolytes for the ECM cells, because they could be generally fast ion conductors due to their relatively open structures [22]. However, most chalcogenides in ECM cells are accompanied by an electrochemically active electrode, e.g., Ag or Cu, or doped with those metals. Since both electrodes consist of Pt or Ti, which are generally considered 'inert electrode' materials

[23], and because the GST layer in this case contains no metallic dopant at all, there might be no active metallic species involved.

TEM observation of both the Pt/GST/Pt and Ti/GST/Pt sample was carried out for the LRS cell after several resistive switching cycles to identify the structural and chemical properties of the conducting filament and the surrounding matrix. Due to the localized nature of the possible CFs in the relatively large memory cell, an extensive search for the region where a distinctive feature could be found was made. Fig 2-5 (a) shows the cross-sectional bright-field STEM (BF-STEM) image of the Pt/GST/Pt cell showing the vicinity of the characteristic features, which appeared to be crystalline among the other parts that remained amorphous in the bright-field image (the diffraction contrast). In the BF-STEM image, a bright region was found to have been extended between the top and bottom electrodes. This region was believed to be coincident with the conducting filament in this LRS cell. To confirm the local composition, EDS spectra were taken from the area near the filament. According to the EDS results, the composition of the filament region was confirmed to be Te-rich (Ge:Sb:Te ~ 6:9:85), whereas the amorphous matrix far from the filament region remained almost stoichiometric (Ge:Sb:Te ~ 22:21:57). HRTEM and Fast Fourier Transformed (FFT) micrographs of the HRTEM for the nearby region were examined extensively to determine the crystallographic structure of the filaments and the remaining part of the GST films. Fig 2-5 (b) shows the crystalline nature of the filament, which connects the top and bottom

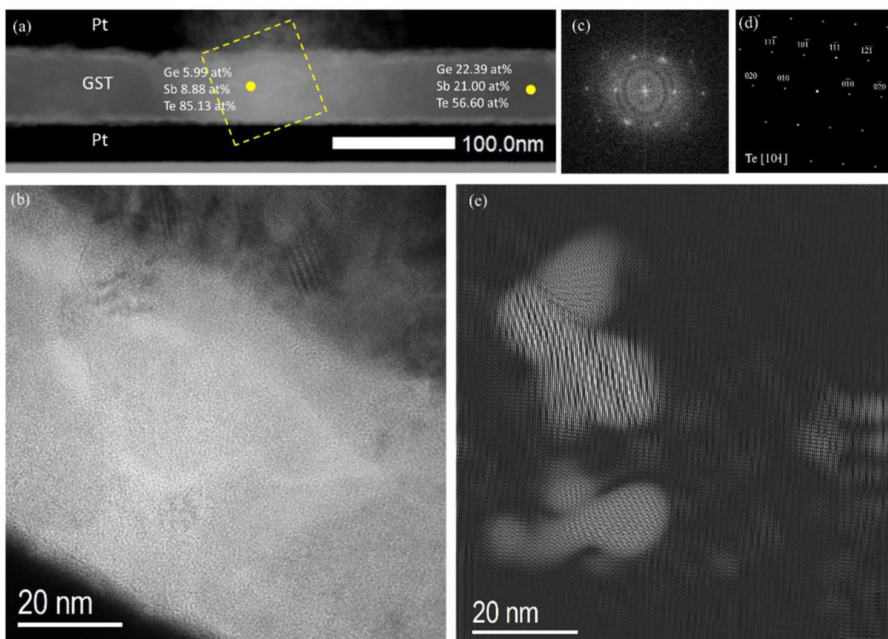

Fig 2-5. (a) Cross-sectional STEM image of Pt/GST/Pt. (b) HRTEM image of the filament region. (c) Fast Fourier Transformed micrograph of the crytsalline filament, (d) corresponding simulated diffraction pattern of tellurium for the [101] zone axis and (e) corresponding Inverse Fast Fourier Transformed micrograph of the crytalline filament.

electrodes and is surrounded by the amorphous matrix. The crystal structure of the filament is confirmed from the fast-Fourier transformation (FFT) image from this region, as shown in Fig 2-5 (c), which coincides very nicely with the simulated [101] zone axis diffraction pattern of tellurium [P3121 space group, see Fig 2-5 (d)]. The measured d-spacing of each diffraction spot is also very consistent with the reported d-spacing value of each plane of tellurium. The presence and shape of crystalline Te filament bridging top and bottom electrode can be confirmed by the Inverse Fast Fourier Transformed micrographs (IFFT) of Te as shown in Fig 2-5 (e). The IFFT image showed that the Te-filament is actually an aggregation of smaller Te particles. In the nearby area, other crystalline Te particles could be seen, suggesting that these Te-particles are the embryos for Te-filament formation. This is consistent with the observation shown in Fig 2-6 (b) below. Thus, it can be concluded that the formation of the filament (electroforming and SET) is achieved by the electric-field-driven migration and recrystallization of tellurium in the amorphous GST matrix that bridges the top and bottom electrodes. This tellurium filament can also be observed in the Ti/GST/Pt sample. Fig 2-6 (a) shows the cross-section bright-field TEM image of the Ti/GST/Pt sample, where the distinctive region in the amorphous matrix was observed. This observation also required extensive search over a large area of the TEM specimen due to the localized nature of these regions. The electron diffraction pattern obtained from this region (inset

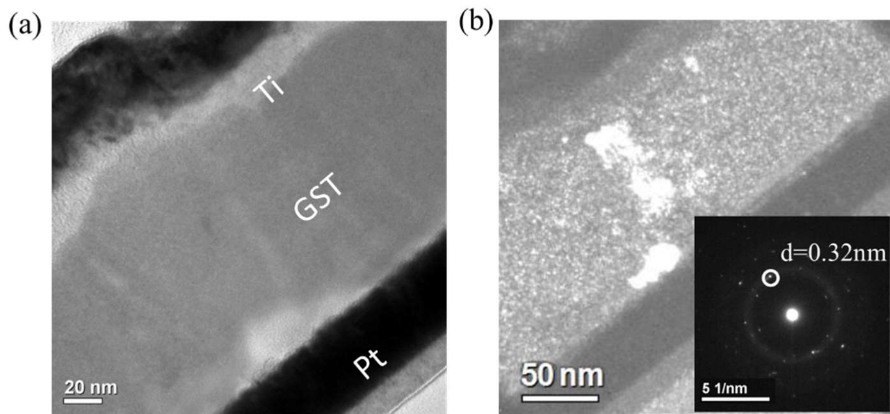

Fig 2-6. (a) Cross-sectional bright-field TEM image and (b) dark-field TEM image of the vicinity of the filament region for Ti/GST/Pt. The inset of (b) shows the selected area diffraction pattern of the filament region.

of Fig 2-6 (b)) showed a diffraction spot with a d-space of 0.32 nm (marked with a circle), which corresponds to the (101) plane of tellurium. The dark-field image from this spot is shown in Fig 2-6 (b). The agglomerated tellurium phase that bridges the top and bottom electrodes is also clearly shown. Also, the broad amorphous ring pattern shown in the electron diffraction pattern indicates that the surrounding GST matrix remains in the amorphous phase after switching many times. The EDS analysis in mapping mode, however, failed to detect the Te filament because of the involvement of the matrix phase over or below the region of interest, of which composition must be Te-deficient. Another interesting finding from the dark-field image is that numerous small particles are embedded in the apparently amorphous matrix, which are also believed to be Te clusters. These Te-clusters appear to be the embryos or nuclei of the Te CFs. Therefore, it was revealed that the bipolar resistive switching for the two devices can be attributed to the same mechanism, i.e., the formation and rupture of the tellurium filament. The formation of the Te-clusters might be attributed to the local chemical modification due to sufficiently large voltage (~2V) of the electroforming step, which can facilitate the subsequent filament formation. This result in the reduced voltage for the afterward SET process.

For further investigation of the nature of the conducting filament and the surrounding matrix, the electrical conduction mechanisms for each resistance state were analyzed in the Pt/GST/Pt sample. To achieve this, the I-V characteristics of each state were measured at the temperature range of 307-357

K, and the results were analyzed by fitting them into the various electrical conduction mechanisms. Fig 2-7 (a) shows the log-log plot of the I-V curves for both the LRS cell and the HRS cell. The LRS curve shows Ohmic-like behavior with a slight resistance decrease (current increase) as the temperature increases, as shown in Fig 2-7 (b). This negative temperature coefficient of resistance (TCR) implies that the conducting filament of the LRS is made of semiconducting elements, unlike the metallic nature of the conduction filament (Cu or Ag) in a general ECM system. The TEM analysis showed that the electrical conduction in the LRS was most probably due to the conduction through the Te filament. Tellurium is a well-known p-type semiconductor with much higher conductivity than amorphous GST [24]. Due to the nanoscale nature and possible involvement of various structural and compositional defects, quantitative comparison of the TCR estimated in Fig 2-7 (a) and the bulk TCR value of Te is improbable. Nevertheless, the coinciding of the electrical conduction behavior, which could be ascribed to the semiconducting material, with the Te-CF confirmed in the TEM strongly suggests that the BRS in these cases is due to the Te formation and rupture of the Te-CFs, depending on the bias polarity. The I-V curves of the HRS show non-Ohmic behavior with a marked resistance decrease as the temperature increased, as shown in Fig 2-7 (c) and (d). This result could be well-fitted into the Poole-Frenkel conduction mechanism, as shown in Fig 2-7 (c). The estimated dielectric constant value obtained via the fitting (30.6 at 273 K) coincided well with the reported value

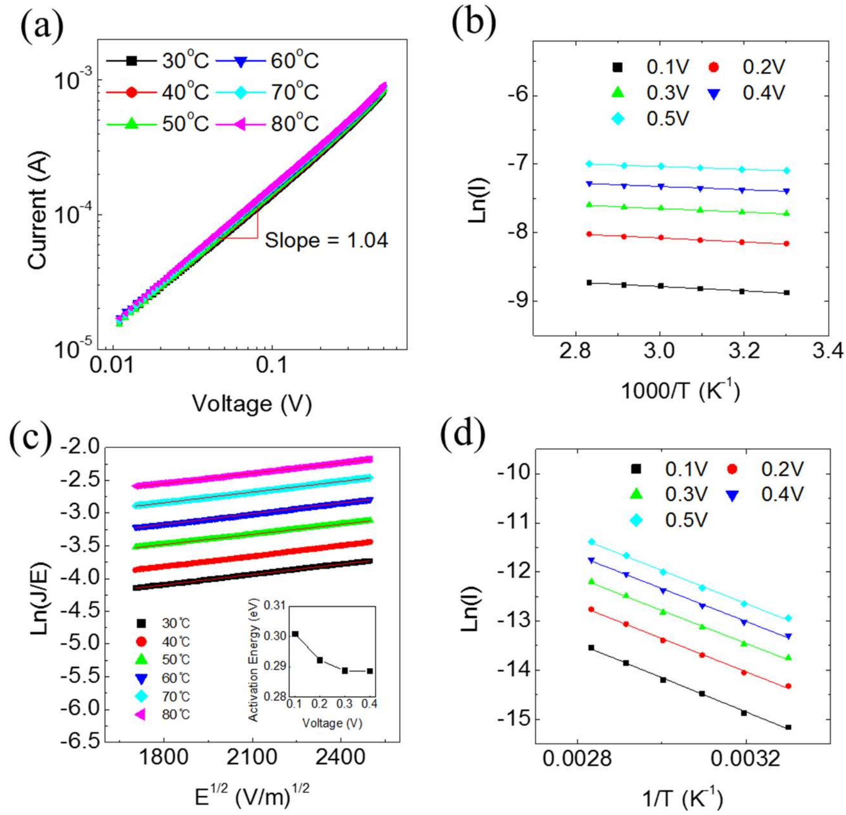

Fig 2-7. (a) LogI-logV plot of the LRS measured at the temperature range of 30-80°C. (b) Arrhenius plot of the LRS showing tempeature dependence and implying the semiconducting nature of the LRS. (c) Ln(J/E) versus $E^{1/2}$ plot of the HRS indicating that Poole-Frenkel conduction dominates HRS. The inset shows the activation energy of the conduction calculated from (d) the Arrhenius plot of HRS.

of the optical dielectric constant of the amorphous GST (28.8) [25], which confirms the validity of the fitting. Considering the reports from many studies that the conduction of amorphous GST follows the Poole-Frenkel mechanism under a sufficiently high electric field, it is reasonable to assume that the HRS current flows through the amorphous GST matrix, across the entire electrode area [26-28]. This assumption can be supported by the calculated activation energy (0.29-0.30 eV) of conduction shown in the inset of Fig 2-7 (c), which is consistent with the reported value for the Poole-Frenkel conduction in the amorphous GST [26].

Through the movement of the Te- ion from the Te-rich layer and the Te filament, the entire switching process can be accounted for by a mechanism very similar to the classical ECM switching mechanism, as schematically shown in Fig 2-8. The only differences are reduction of Te at the active Te electrode, while in cation-based ECM, there is oxidation of Ag or Cu at the active electrode, and reverse moving direction of electrons through the external wire. Here, electrons move from the inert to active electrode, while in cation-based ECM, they move from active to inert electrode. Fig 2-8 (a) presents the pristine state. There is a Te-rich layer between the amorphous (as-deposited) GST layer and the Pt bottom electrode (the thickness of the Te-rich layer is exaggerated in this schematic diagram). When a positive (negative) bias is applied to the top (bottom) electrode [Fig 2-8 (b)], the electrons are injected into the Te-rich layer from the bottom electrode, which causes the ionization of

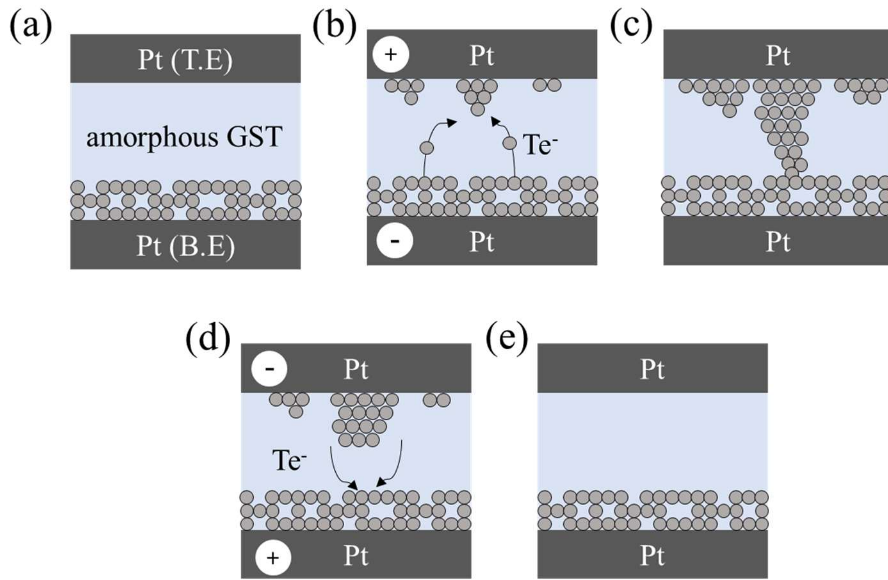

Fig 2-8. Schematic representation of the bipolar resistive switching mechanism. (a) Pristine state. (b) SET operation. (c) LRS. (d) RESET operation. (e) HRS.

Te. These negatively charged Te ions could migrate to the positive-biased top electrode under a high electric field, and form a filament. When the growing filament reaches the bottom electrode, the cell switches to the LRS [Fig 2-8 (c)]. When the bias polarity is reversed, the filament starts to resolve [Fig 2-8 (d)], and finally, the cell switches back into the HRS [Fig 2-8 (e)].

From this point of view, it can be understood that the Te-rich layer formed at the bottom interface plays a crucial role as an active electrode in the switching, whereas the top electrode should play the role of an inert electrode. As shown above, the sample with different top electrodes, i.e., Ti and Pt, showed almost identical electrical behavior, such as I-V characteristics, electrode area dependence, and order of magnitude of the resistance in both states, despite the marked difference in the work functions of the two metals (4.33 eV for Ti and 5.64 eV for Pt). This strongly indicates that the formation and rupture of Te-CFs are closely related to the bottom interface. From these experiments the following electrochemical reaction could be asserted to be responsible for the set and reset transitions.

For the set process;

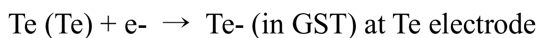
Te (Te) + e- → Te- (in GST) at Te electrode

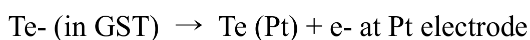
Te- (in GST) → Te (Pt) + e- at Pt electrode

For the reset process;

Te (Pt) + e- → Te- (in GST) at Pt electrode

Te- (in GST) → Te (Te) + e- at Te electrode

Such reactions are suggested based on the references on the counter charges and counter electrode reactions by Valov [29], and Tappertzhofen et al. [30].

The feasibility of switching via Te migration can be also confirmed by the diffusion coefficeint of Te in GST which reflects how mobile Te ion is in GST matrix. According to study regarding atomic migration in line structure GST cell by Yang et al., [31] the average value of diffusion coefficient of Te in GST is ~4×10^{-5} cm^2s^{-1}. Although this value was assumed to be in molten state migration, it is more reasonable to postulate that only partial region was melt while rest remained as amorphous phase considering large dimension (~20μm) of the tested cell and relatively low value of applied field (3650V/cm) in the study and hence the migration behavior in this case somewhat reflect the migration in amorphous phase. This can be supported by the diffusion coefficient calculated by molecular dynamics (MD) simulation in amorphous GeTe, which shares most of the properties with GST [32]. Comparable self-diffusion coefficient in amorphous phase to that in super-cooled liquid phase up to ~10^{-6} cm^2 s^{-1} at 500K was reported, implying similar order of magnitude of diffusion coefficient of Te in GST. Considering that the diffusion coefficient of Cu ion in SiO_2, well-known Cu:SiO_2 ECM system, is almost 10^{-10}~10^{-12} cm^2 s^{-1} at room temperature [33], it can be deduced that Te ion in GST is sufficiently

mobile for validity of proposed switching mechanism via formation and rupture of conductive filament by Te migration.

2.4. Summary

The bipolar switching behavior of amorphous GST was examined. The observed bipolar switching involves the polarity-dependent formation and rupture of a localized conducting filament, which can be attributed to the migration and recrystallization of tellurium ionized under a high electric field. The entire switching mechanism can be explained well by a model based on the typical ECM theory that the Te-rich layer is near the bottom Pt electrode interface and Te CFs are involved. Although the Te-rich layer near the bottom Pt electrode is supposed to have originated from the ion bombardment effect during the sputtering of GST on Pt, such thin Te layer can be alternatively formed by ca. deliberate deposition. The BRS performance required smaller reset power than the typical PCRAM operation with non-interacting TiN electrodes. In addition, the device performance as a feasible ReRAM was highly promising in terms of its resistance ratio, switching uniformity, and retention. This study surfaced not only new possibilities for the application of chalcogenide materials as next-generation non-volatile memory devices, but also for further understanding of the solid electrolytic resistive switching behavior of chalcogenide materials.

2.5. Bibliography

1. Wuttig, M.; Yamada, N., *Nat Mater* **6** (11), 824-832 (2007)

2. Ovshinsky, S. R., *Physical Review Letters* **21** (20), 1450-1453 (1968)

3. Feinleib, J.; deNeufville, J.; Moss, S. C.; Ovshinsky, S. R., *Applied Physics Letters* **18** (6), 254-257 (1971)

4. Ovshinsky, S. R.; Fritzsche, H., *Electron Devices, IEEE Transactions on* **20** (2), 91-105 (1973)

5. Lencer, D.; Salinga, M.; Grabowski, B.; Hickel, T.; Neugebauer, J.; Wuttig, M., *Nature Materials* **7** (12), 972-977 (2008)

6. Burr, G. W.; Breitwisch, M. J.; Franceschini, M.; Garetto, D.; Gopalakrishnan, K.; Jackson, B.; Kurdi, B.; Lam, C.; Lastras, L. A.; Padilla, A.; Rajendran, B.; Raoux, S.; Shenoy, R. S., *Journal of Vacuum Science and Technology B* **28** (2), 223-262 (2010)

7. Waser, R.; Aono, M., *Nat Mater* **6** (11), 833-840 (2007)

8. Waser, R.; Dittmann, R.; Staikov, G.; Szot, K., *Advanced Materials* **21** (25-26), 2632-2663 (2009)

9. Kim, K. M.; Choi, B. J.; Hwang, C. S., *Nanotechnology* **22** (25), 254002 (2011)

10. Yang, J. J.; Pickett, M. D.; Li, X.; OhlbergDouglas, A. A.; Stewart, D. R.; Williams, R. S., *Nature Nanotechnology*, **3**, 429-433 (2008)

11. Kwon, D.-H.; Kim, K. M.; Jang, J. H.; Jeon, J. M.; Lee, M. H.; Kim,

G. H.; Li, X.-S.; Park, G.-S.; Lee, B.; Han, S.; Kim, M.; Hwang, C. S., *Nature Nanotechnology* **5** (2), 148-153 (2010)

12. Kozicki, M. N.; Mira, P.; Mitkova, M., *Nanotechnology, IEEE Transactions on* **4** (3), 331-338 (2005)

13. Pandian, R.; Kooi, B. J.; Oosthoek, J. L. M.; van den Dool, P.; Palasantzas, G.; Pauza, A., *Applied Physics Letters* **95** (25), - (2009)

14. Pandian, R.; Kooi, B. J.; Palasantzas, G.; De Hosson, J. T. M.; Pauza, A., *Advanced Materials* **19** (24), 4431-4437 (2007)

15. Woo, J.; Jung, S.; Siddik, M.; Cha, E.; Sadaf, S. M.; Hwang, H., *Applied Physics Letters* **99** (16), 162109-3 (2011)

16. Pandian, R.; Kooi, B. J.; Palasantzas, G.; De Hosson, J. T. M.; Pauza, A., *Applied Physics Letters* **91** (15), - (2007)

17. Wuttig, M.; Lusebrink, D.; Wamwangi, D.; Welnic, W.; Gilleszen, M.; Dronskowski, R., *Nat Mater* **6** (2), 122-128 (2007)

18. Lbibb, R.; Castanet, R., *Journal of Alloys and Compounds* **189** (1), 23-29 (1992)

19. Lbibb, R.; Castanet, R., *Journal of Alloys and Compounds* **199** (1–2), 165-170 (1993)

20. Grønvold, F.; Thurmann-Moe, T.; Westrum, E. F.; Chang, E., *The Journal of Chemical Physics* **35** (5), 1665-1669 (1961)

21. Yoshihisa, F., *Japanese Journal of Applied Physics* **49** (10R), 100001 (2010)

22. Ribes, M.; Bychkov, E.; Pradel, A., *Journal of Optoelectronics and Advanced Materials* **3** (3), 665-674 (2001)

23. Ilia, V.; Rainer, W.; John, R. J.; Michael, N. K., *Nanotechnology* **22** (25), 254003 (2011)

24. Capers, M. J.; White, M., *Thin Solid Films* **15** (1), 5-14 (1973)

25. Park, J.-W.; Eom, S. H.; Lee, H.; Da Silva, J. L. F.; Kang, Y.-S.; Lee, T.-Y.; Khang, Y. H., *Physical Review B* **80** (11), 115209 (2009)

26. Ielmini, D.; Zhang, Y., *Journal of Applied Physics* **102** (5), 054517 (2007)

27. Nardone, M.; Simon, M.; Karpov, I. V.; Karpov, V. G., *Journal of Applied Physics* **112** (7), 071101 (2012)

28. Beneventi, G. B.; Guarino, L.; Ferro, M.; Fantini, P., *Journal of Applied Physics* **113** (4), 044506 (2013)

29. Valov, I., *ChemElectroChem*, **1**, 26-36 (2014)

30. Tappertzhofen, S.; Valov, I.; Tsuruoka, T.; Hasegawa, T.; Waser, R.; Aono, M.;, *ACS Nano*, **7**, 6396-6402 (2013)

31. Yang, T.; Park, I.; Kim, B.; Joo, Y., *Applied Physics Letters* **95** (3), 032104 (2009)

32. Sosso, G. C.; Behler, J.; Bernasconi, M., *Physica Status Solidi (a)* **213** (2), 329 (2016)

33. Tappertzhofen, S.; Mundelein, H.; Valov, I.; Waser, R., *Nanoscale* **4**, 3040 (2012)

3. Ovonic threshold switching behavior of Ge-Sb-Se-Te thin films deposited by Atomic layer deposition

3.1. Introduction

Passive matrix cross-bar array (CBA) have been considered as a leading candidate due to the high degree of cell integration as well as cost-effectiveness enabled by implementation of a resistive layer consist of simple two-terminal metal-insulator-metal (MIM) structure and consequent effective cell dimension of $4F^2$ [1-4]. However, significant leakage problem from unselected cell of low-resistance state often referred as 'sneak current', causing reading / writing disturbance during operation, has been considered as primary obstacle for the application of CBA [3-4]. The selector device, which exhibits strong non-linear current-voltage characteristics, has been proposed to solve the sneak current problem by suppress the current flow through unselected cell [5]. Volatile resistive switching with high selectivity and two-terminal simple structure is the key properties of the selector device and various type of switching satisfying this condition such as diode [6-10], Metal-Insulator Transition (MIT) [11-13], Mixed Ion-Electron Conductor (MIEC) [14-15], Field Assisted Super-linear Threshold (FAST) [16-17] has been studied for the selector device application. Among them, Ovonic threshold switching (OTS) has been considered as the

ideal candidate for selector device application due to its polarity-independent, highly non-linear current-voltage characteristics as well as two-terminal simple MIM structure [18-21].

Ovonic threshold switching is characterized by sudden transition to low resistance state at a critical voltage called threshold voltage with negative differential resistance (NDR) behavior, retaining its low resistance state until applied voltage is maintained even at the level far less than threshold voltage, so called minimum holding voltage [22]. When the applied voltage is reduced below minimum holding voltage, recovery transition to its original high resistance state occurs. It should be distinguished from commonly occurred high field electrical breakdown in terms of its repeatable and non-destructive nature. The current-voltage characteristic observed in current sweep mode generally exhibits S-shaped NDR behavior, so called voltage snapback phenomena [5].

Since the original work by S. Ovshinsky reported first threshold switching in chalcogenide glass containing Si, Ge, As, and Te [23], most of the researches regarding threshold switching behavior is focused on chalcogenide materials, particularly for selenide and telluride [18, 20, 24]. Threshold switching behavior is enabled by the characteristic feature of amorphous chalcogenide, namely small bandgap width and high density of localized state near 10^{19} cm^{-3}, which distinguish itself from conventional semiconductor such as Si [25].

For the application as a selector device, it is essential to suppress any long-range structural rearrangement such as crystallization. The group IV and V elements are usually incorporated, acting as cross-linking elements that stabilize the amorphous phase. The stability of amorphous phase is directly related to the cycling endurance, which is one of the key requirement for selector device. The most frequently used elements for amorphous stabilization is Si, Ge in group IV and As in group V [18, 21, 23]. While As is considered to have the strongest glass-forming ability, its pronounced toxicity make it inappropriate for the device fabrication, requiring the alternative environment-friendly glass-former.

Deposition of chalcogenide thin films for either selector or conventional phase change materials are usually conducted by physical vapor deposition (PVD) such as sputtering or chemical vapor deposition (CVD) [26]. Recent researches have been reported atomic layer deposition (ALD) of chalcogenide [27-29], mostly focused on the deposition of Ge-Sb-Te ternary materials for phase change application. Due to excellent step coverage as well as precise controllability of thickness and composition, atomic layer deposition has great benefits for selector device as well, particularly for vertical structure 3D 1S1R (1 Selector, 1 Resistor) device with high aspect ratio.

In this study, ovonic threshold switching behavior and the composition effect on its switching parameter and cycling endurance is evaluated in Ge-Sb based

chalcogenide films deposited by atomic layer deposition. Based on $GeTe_2$: Sb_2Te_3 pseudo-binary film deposition process reported by author's group [27], Sb_2Se_3 deposited from novel Se precursors is incorporated. The binary ratio effect in $GeTe_2$: Sb_2Te_3 pseudo-binary and $GeTe_2$: Sb_2Te_3 : Sb_2Se_3 pseudo-ternary was examined.

3.2. Experimental

Ge-Sb-Te and Ge-Sb-Se-Te films were deposited by a ALD reactor with 12-inch-diametered shower head and 8-inch-wafer scale compatible substrate heater (CN-1, Plus-200). Fig 3-1 shows the schematic diagram of ALD system. Four precursors were used for deposition. The Ge precursor was $Ge(OC_2H_5)_4$, the Sb precursor was $Sb(O_C2H_5)_3$, the Te precursor was $[(CH_3)_3Si]_2Te$, and the Se precursor was $[(CH_3)_3Si]_2Se$. Ge, Sb, and Te precursors were heated to 40°C while Se precursors were heated to 30°C due to its high vapor pressure. The precursors were carried to the process module by Ar carrier gas at a flow rate of 50 sccm. For purge process, 200 sccm of Ar gas was used. Additional 150 sccm Ar gas was injected to process chamber during the precursor injection step to compensate for the difference of Ar gas flow rate between precursor injection and purge step. The working pressure of process chamber was maintained in a range of 3.0 ± 0.2 Torr during deposition. Detailed conditions for the deposition process are summarized in Table 3-1. Overall deposition cycle configuration is shown in Fig 3-2. Precursor injection pulse and purge pulse comprises precursor sub-cycle. Combination of two precursor sub-cycles, Ge – Te, Sb – Te, Sb – Se in this case, constitutes one binary cycle. Blending those binary cycles in arbitrary ratio compose super-cycle. Repeating this super-cycle results in the deposition of ternary, or quaternary films.

X-ray fluorescence spectroscopy (XRF, Thermo Scientific, ALR Quant'X

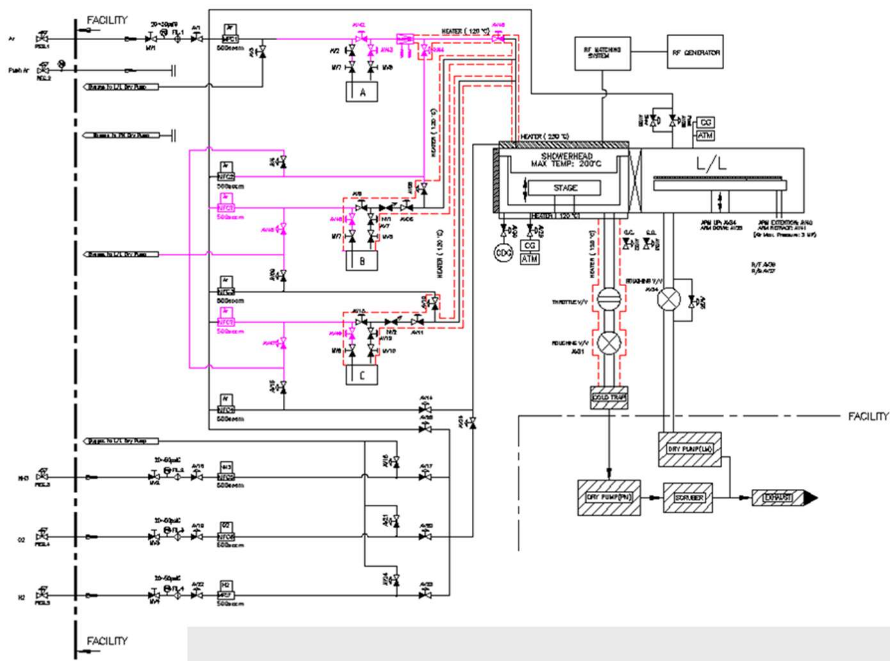

Fig 3-1. Schematics of ALD apparatus utilized in the experiments.

Sub. Temp (^{o}C)	Canister Temp (^{o}C)				Carrier Gas (Ar, sccm)	Purge Gas (Ar, sccm)	Pres. (Torr)
	Ge-OEt	Sb-OEt	MeSi-Te	MeSi-Se			
50 – 100	40	40	40	30	50	200	3.5

Table 3-1. Detailed deposition conditions for the deposition process.

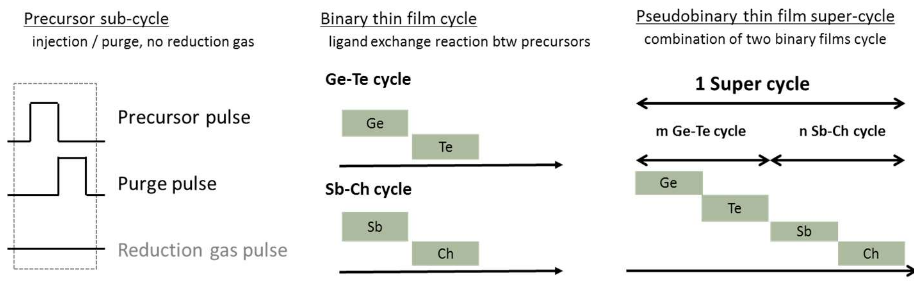

Fig 3-2. Cycle configurations of the deposition process where Ch denotes chalcogenide precursors, namely $[(CH_3)_3Si]_2Te$ and $[(CH_3)_3Si]_2Se$.

EDXRF) was used to measure the composition and layer density of deposited films. X-ray diffraction (XRD, PANalytical, X'pert PRO MPD) was used to confirm the crystallization of films annealed at various temperature to verify the crystallization temperature. Spectroscopic Ellipsometer (SE, J.A.Woollam, ESM-300) was used to measure optical constant to determine optical band gap by drawing Tauc plot. Electric pulse application and the observation of response were achieved by Pulse generator (Agilent, 81110A) and Oscilloscope (Tektronix, TDS 684C) using measurement setup depicted in Fig 3-3.

Ge-Sb-Te and Ge-Sb-Se-Te films for XRD and SE measurement were deposited on thermally oxidized Si substrate. The samples for electrical characterization is fabricated on single hole-patterned substrate by photolithography using process step shown in Table 3-2. The structure of fabricated sample is schematically depicted in Fig 3-4. The diameter of hole-patterned bottom electrode was 2μm.

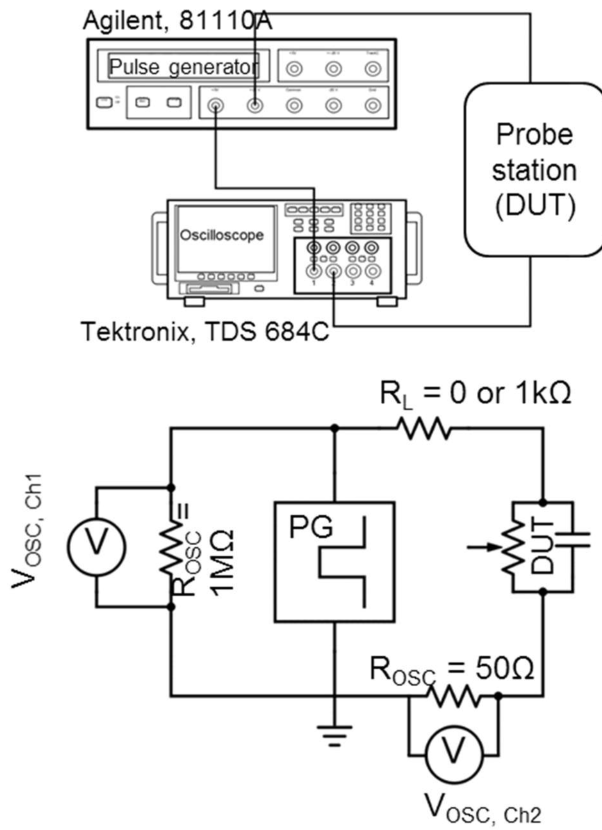

Fig 3-3. Schematic diagram of the measurement system for pulse response measurement.

Process flow		
No	Process	Recipe
1	PR Strip / Organic cleaning	Acetone 10min / Methanol 1min / IPA 2min / DIW 2min
2	Native oxide etching	BOE 6:1, 10s
3	Chalcogenide deposition	Target thickness ~ 30nm at ALD system
4	BEC pad etching	Photo at MA-6 Aligner (Karl Suss) GST etching by HNO_3 : H_2O = 1:2, 10s
5	TE / BEC fabrication	Photo at MA-6 Aligner (Karl Suss) Metal deposition by E-gun evaporator Lift-off

Table 3-2. Process flow for device fabrication.

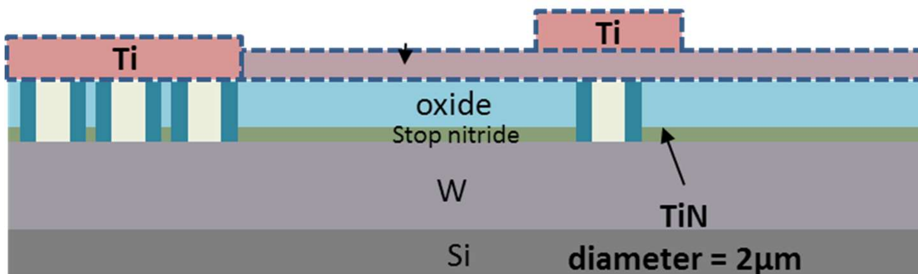

Fig 3-4. Schematic diagram of fabricated device using single hole patterned substrate with 2μm hole diameter.

3.3. Results and Discussions

Binary $GeTe_2$ and Sb_2Te_3 films were deposited by Atomic layer deposition process early developed by author's group [27]. The ligand exchange between $[(CH_3)Si]_2Te$ and stable alkoxy-Ge ($Ge(OC_2H_5)_4$) / alkoxy-Sb ($Sb(OC_2H_5)_3$ metalorganic precursors according to expected reaction in Equation 3-1 and 3-2 results in the deposition of $GeTe_2$ and Sb_2Te_3 films, respectively.

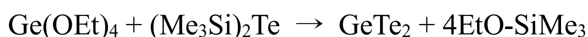

$$Ge(OEt)_4 + (Me_3Si)_2Te \rightarrow GeTe_2 + 4EtO\text{-}SiMe_3$$

Equation 3-1

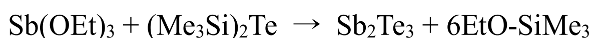

$$Sb(OEt)_3 + (Me_3Si)_2Te \rightarrow Sb_2Te_3 + 6EtO\text{-}SiMe_3$$

Equation 3-2

Combining two binary layers enables the deposition of various composition lying on the $GeTe_2$-Sb_2Te_3 tie line as shown in Fig 3-5. Binary Sb_2Se_3 films were deposited using novel $[(CH_3)Si]_2Se$ Se precursor. Similar reaction mechanism between ($Sb(OC_2H_5)_3$ and $[(CH_3)Si]_2Se$ as Sb_2Te_3 deposition in equation 3-3 is expected since Se precursor has same ligand as Te precursors.

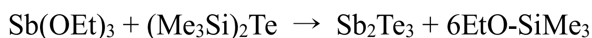

$$Sb(OEt)_3 + (Me_3Si)_2Te \rightarrow Sb_2Te_3 + 6EtO\text{-}SiMe_3$$

Equation 3-3

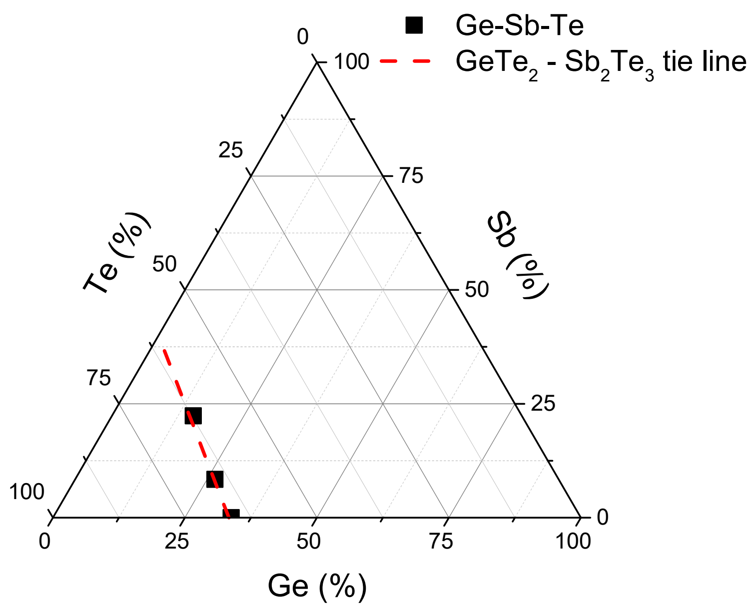

Fig 3-5. Ternary diagram of various Ge-Sb-Te films deposited by combining $GeTe_2$ and Sb_2Te_3.

Saturation curve of each binary cycles are shown in Fig 3-6. Except the injection and purge curve of Ge precursor, all precursors show stable growth saturation, or self-limited behavior, which is the unique feature of atomic layer deposition, implying that ideal atomic layer deposition were achieved. The non-ideal behavior of Ge precursors is due to its physisorption type behavior and detailed explanation can be found in previously report by author's group. Despite its non-ideal behavior, highly conformal film in terms of thickness and composition in the hole with extremely high aspect ratio was successfully deposited, ensuring the compatibility of 3D structure [30]. The injection and purge time of each precursor were determined according to the saturation curve in Fig 3-6. Detailed injection and purge time of each precursor are shown in Table 3-3. Stoichiometric compositions were achieved for every deposited binary films implying the expected ligand exchange reaction occurs appropriately.

Incorporation of binary Sb_2Se_3 into $GeTe_2$-Sb_2Te_3 ternary resulted in deposition of quaternary Ge-Sb-Se-Te films which is comprised of combination of three binary films – $GeTe_2$, Sb_2Te_3, and Sb_2Se_3. Various compositions can be deposited by changing the ratio of binary cycle as shown in pseudo-ternary diagram Fig 3-6 (a), quaternary 3D diagram in Fig 3-6(b) and Table 3-4. Note that cycle ratio and actual composition ratio of binaries are not linearly proportional despite composition changes in accordance with cycle ratio change.

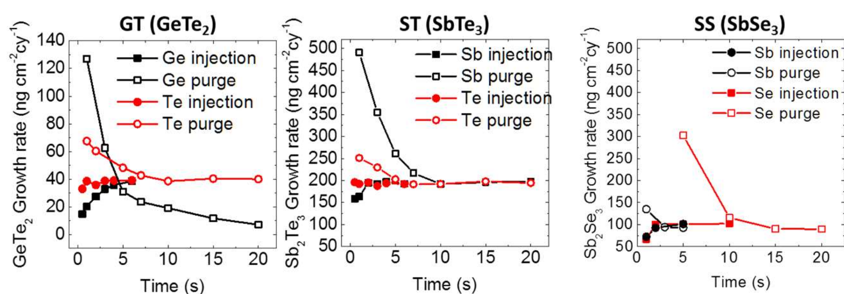

Fig 3-6. Saturation curve of the precursors for each binary films.

Precursor	Injection (s)	Purge (s)	Stage T (ºC)
$Ge(OEt)_4$	6	5	70
$Sb(OEt)_3$	2	5	
$(Me_3Si)_2Te$	1	10	
$(Me_3Si)_2Se$	3	15	

Table 3-3. Determined precursor injection and purge time and deposition temperature according to the measured saturation curve for each precursors.

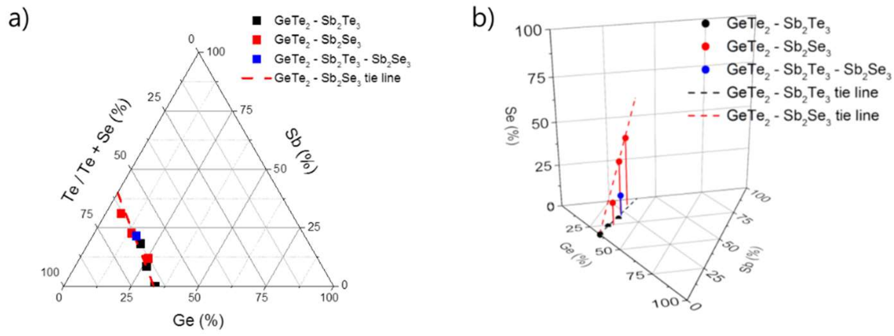

Fig 3-7. (a) Pseudo-ternary and (b) 3D quaternary diagram of deposited films with various compositions by combining $GeTe_2$, Sb_2Te_3, and Sb_2Se_3 binary films.

Cycle ratio	**Ge (%)**	**Sb (%)**	**Se (%)**	**Te (%)**
GT	33.78	-	-	66.22
GT**6** ST**1**	26.50	8.41	-	65.10
GT**2** ST**1**	24.11	13.07	-	62.82
GT**1** ST**1**	15.41	22.35	-	62.24
GT**1** SS**2**	5.67	31.13	40.43	22.77
GT**1** SS**1**	13.84	22.63	31.22	32.32
GT**4** SS**1**	25.35	11.88	13.47	49.29
GT**2** ST**1** SS**1**	16.27	21.42	12.14	50.16

Table 3-4. Composition of deposited films with respect to cycle ratio.

It can be easily expected that compositional variation significantly influences the threshold switching parameter. Evaluation of the effect of composition on switching parameter will provide the proper methods of parameter engineering. In order to evaluate the effect of composition on threshold switching behavior, two experimental set were established. First set consists of three different compositions where the effect of $GeTe_2$: Sb_2Te_3 ratio was examined. In this set, variation of Te composition is not significant in comparison with variation of Ge and Sb. Thus, effect of Ge : Sb on threshold switching parameter can be evaluated. Second set consists of three different compositions where the effect of Se composition is examined while Ge/Sb ratio is unchanged. Se incorporation is achieved by replacing a total or a portion of Sb_2Te_3 binary with Sb_2Se_3 binary. Adjusting the ratio of Sb_2Te_3 and Sb_2Se_3 provides the methods of incorporating Se into films without breaking Ge : Sb ratio. Thus, in three composition in this set, Se : Te ratio is modulated while Ge and Sb composition remains almost constant so that the sole effect of Se can be observed. The compositions and thicknesses of each samples in both set are shown in Table 3-5.

Trapezoidal pulse (500 ns rise time, 500ns plateau time, and 500ns fall time) and its response was utilized to verify the threshold characteristics. The voltage applied to the device and current flowing through the device can be calculated by Equation 3-4 and 3-5 in the measurement setup shown in Fig 3-3.

Sample name	Composition				d (nm)
	Ge(%)	Sb(%)	Se(%)	Te(%)	
GST Sb0	33.78	-	-	66.22	17.89
GST Sb 8.4	26.5	8.41	-	65.10	34.38
GST Sb 22.35	15.41	22.35	-	62.24	31.47
GSST Se 0	15.41	22.35	-	62.24	31.47
GSST Se 12.1	16.27	21.42	12.14	50.16	34.41
GSST Se 31.2	13.84	22.63	31.22	32.32	42.31

Table 3-5. The composition and thickness of each samples in two experimental set.

$$\boldsymbol{V_{DUT}} = V_{Ch1} - \frac{V_{Ch2}}{50} \times (R_L + 1)$$

Equation 3-4

$$\boldsymbol{I_{DUT}} = \frac{V_{Ch2}}{50}$$

Equation 3-5

As shown in Fig 3-8, the input voltage and calculated voltage and current of the device can be shown in one pulse response graph and major switching parameter and current-voltage characteristics can be extracted by single measurement. First, threshold switching voltage (V_{th}) can be determined as shown in Fig 3-8 (a). At OFF state, most of the voltage is applied to the device. At certain voltage the current suddenly increases while the voltage applied to the device suddenly drops, where the threshold switching begins. The voltage at the beginning of threshold switching is defined as threshold voltage, or V_{th}. Switching time, or t_s, which is defined as the time between onset of threshold switching and complete transition to ON state, can be determined by time from sudden increase of current with more steep slope to transition into ohmic behavior with less slope as shown in Fig 3-8 (a). After the transition to ON state, the device maintains its low resistance state until the decreasing voltage reaches to holding voltage, or V_h, which defined as minimum voltage required to

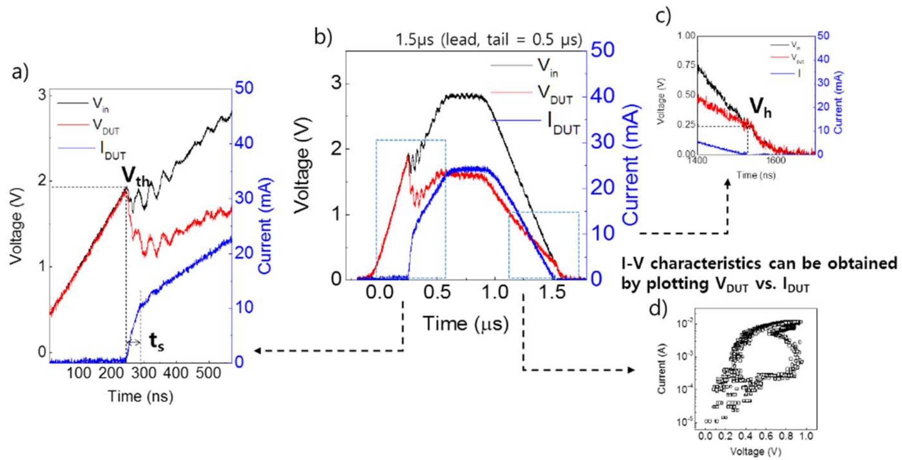

Fig 3-8. (a), (b), (c) Representative pulse response characteristics and (d) extracted current-voltage characteristics of threshold switching device measured in GST (Sb 8.4%) sample.

maintain low resistance state as shown in Fig 3-8 (c). Also, current-voltage curve can be obtained by simply plotting applied voltage versus flowing current as shown in Fig 3-8 (d). Among three major switching parameters, namely threshold voltage, switching time and holding voltage, holding voltage are known to be primarily dependent on the measurement setup or electrode materials rather than intrinsic properties of chalcogenide and switching time is known to be primarily dependent of applied voltage and the capacitance. Thus, threshold voltage will mainly be focused, which are known to be strongly dependent on material properties, especially on electronic structure, which is expected to be determined by compositional change.

The endurance characteristic was obtained by applying and SET pulse / READ pulse and measuring current separately. SET pulse for measuring ON state current was set to 500ns (200 ns rise time, 100ns plateau time, and 200ns fall time) and 2V, which exceeds every sample's threshold voltage in order to ensure stable switching and READ pulse was for measuring OFF state current was set to 0.2V with same pulse shape.

Threshold switching characteristics of every deposited films in GST set and GSST set are shown in Fig 3-9. Characteristic threshold switching behavior including sudden voltage drop and current increase is observed in every composition. Extracted current-voltage curves of every composition commonly shows clear negative differential resistance (NDR), or so-called voltage

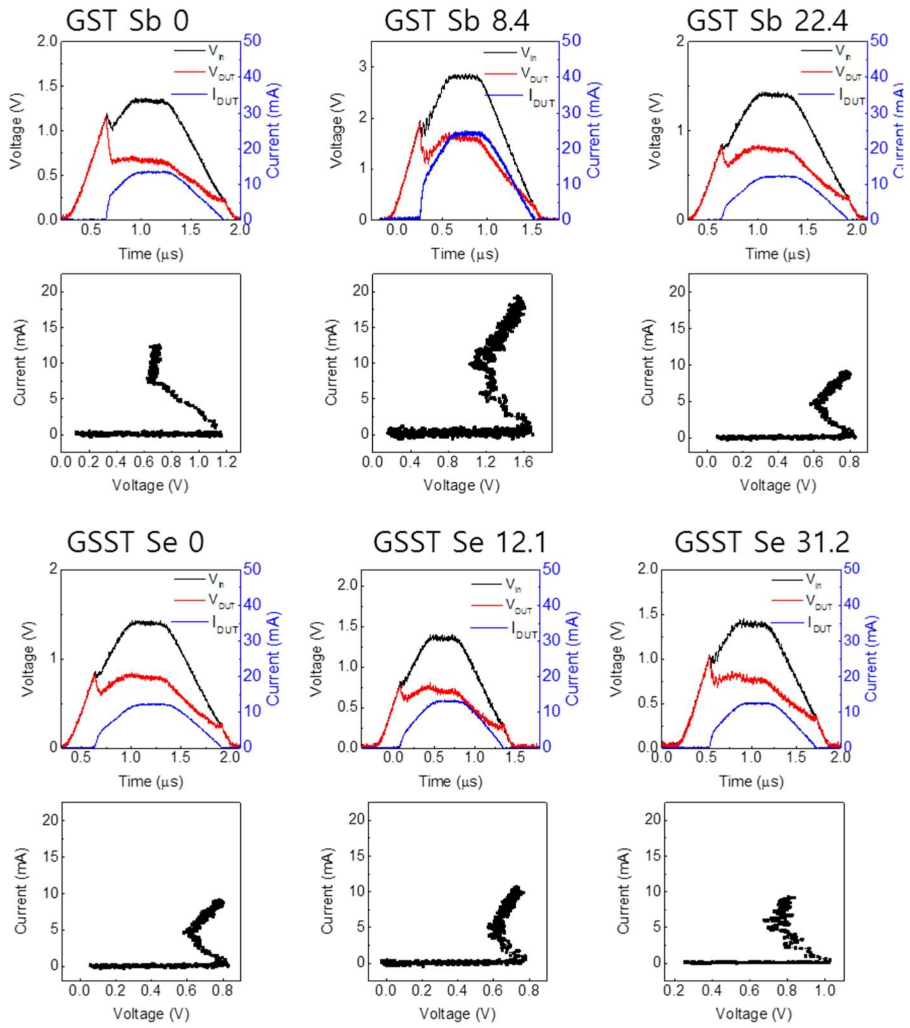

Fig 3-9. Threshold switching behaviors observed by pulse response and current-voltage curves of measured samples.

snapback phenomena, which is the unique characteristics of threshold switching.

First, the effect of composition on switching characteristics for GST set was analyzed to find out the optimal composition for threshold switching device. The endurance characteristic with respect to $GeTe_2$:Sb_2Te_3 ratio, or simply Sb concentration, is shown in Fig 3-10. There is no significant difference or enhancement by change in composition, implying that ratio of Ge:Sb does not affect the amorphous stability significantly. Also, every samples started to failed after few hundreds cycle, showing poor endurance characteristics for selector device application. This is somewhat predictable since the ternary of Ge-Sb-Te is originally adopted as phase change materials, which exhibit fast crystallization. Thus, enhancement of amorphous stability is required for the application of threshold switching device.

However, it was shown that ratio of Ge:Sb greatly affect to switching parameter in Fig 3-11 (a). Note that threshold electric field, or F_{th} is used instead of threshold voltage (V_{th}) to calibrate the influence of different the film thickness since V_{th} is known to be linearly dependent on the film thickness. In Fig 3-11 (a), it can be observed that both threshold field decreases as ratio of Sb_2Te_3, or more generally, Sb concentration increases. As stated above, threshold field is strongly dependent on the electronic structure of chalcogenide. Measured optical band gap is shown in Fig 3-11 (b). The reduction of optical

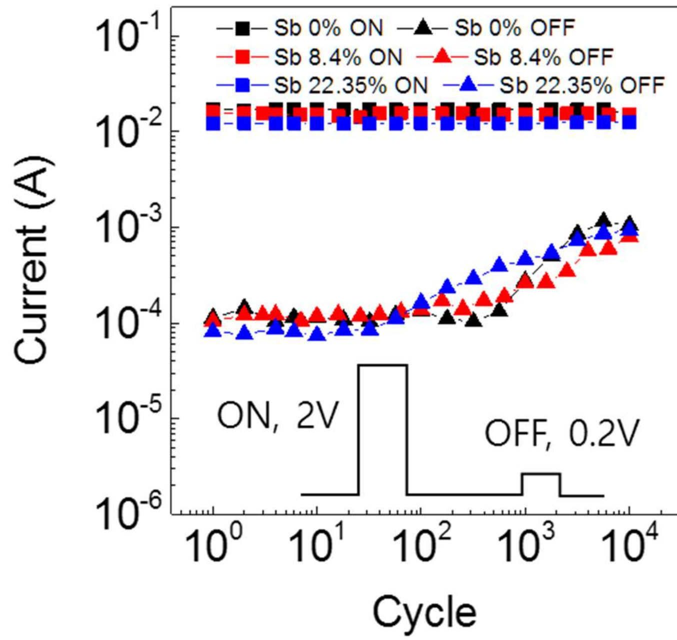

Fig 3-10. The cycling endurance characteristics with respect to $GeTe_2$: Sb_2Te_3 ratio.

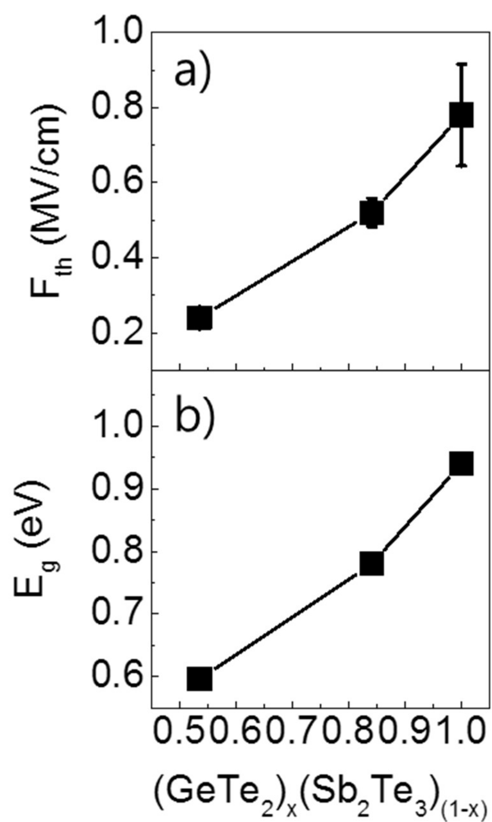

Fig 3-11. (a) Threshold field and (b) optical bandgap with respect to $GeTe_2$: Sb_2Te_3 ratio.

band gap by increasing Sb_2Te_3 ratio in $GeTe_2$-Sb_2Te_3 pseudo-binary follows similar tendency of the case of GeTe-Sb_2Te_3 pseudo-binary which also exhibits similar optical band gap reduction as ratio of Sb_2Te_3 increases. Threshold field seems to be decreased as optical band gap is reduced, which is in accordance with many researches including analytical simulation and experimental data regarding the optical band gap dependence of threshold voltage / field [20, 22].

The influences of optical bandgap to threshold field can be supported by simulation and fitting of measured and calculated of current-voltage curve shown in Fig 3-12. Simulation model was adopted from a study in analytical modeling of threshold switching by Ielmini [22]. Obtain current-voltage curve is well-fitted by calculated curve using measured optical bandgap. Despite the inaccuracy in estimation of density of localized state due to assumption of uniform distribution of localized state in this model, both density and average inter-distance of localized state remain almost unchanged with respect to compositional variation, which sufficiently proves that there is no significant change in distribution of the localized state. This implies that change in Ge:Sb ratio only causes the modulation of optical bandgap while distribution of the localized state is unaffected and the change in switching parameter can be accounted by sole effect of optical bandgap variation in this case.

The effect of Se concentration on switching characteristics is evaluated maintaining Ge:Sb ratio to be almost 15:22 where the lowest threshold field

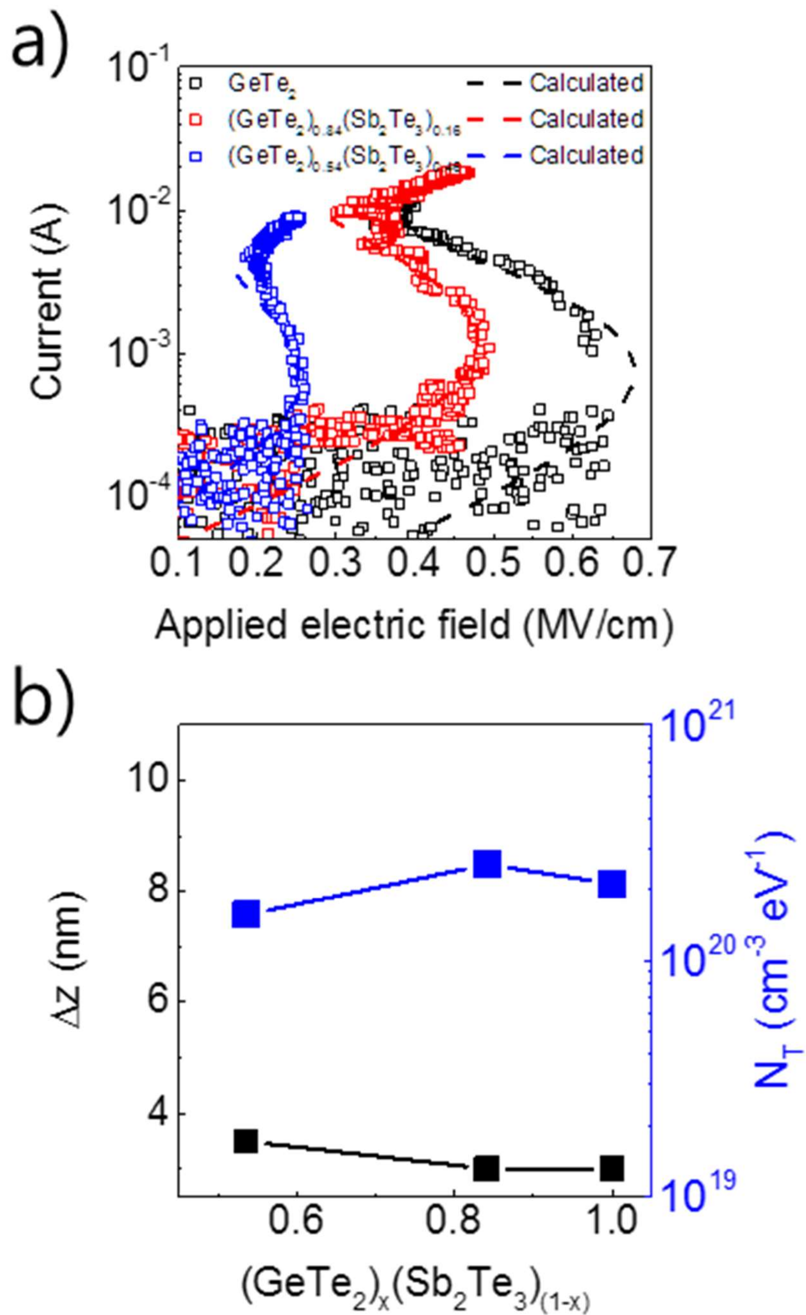

Fig 3-12. (a) Measured and calculated current-voltage curve of GST samples and (b) fitted values regarding the distribution of localized state.

was achieved. Since enhancement of amorphous stability is the major goal of incorporating Se, crystallization temperature was estimated by confirming crystallinity of films annealed in various temperature by X-ray diffraction. Fig 3-13 presents XRD patterns of samples annealed in different temperature at intervals of 50℃ for Se 0% sample and of 100℃ for Se 12.14% and 31.22%, respectively. XRD results shows that crystallization temperature is increased from nearly 150℃ to almost below 400℃ by incorporation of Se, implying amorphous stability is greatly enhanced. The enhancement of amorphous stability influenced the endurance characteristic of devices as shown in Fig 3-14 (a). Increasing Se concentration results in considerable improvement of cycling endurance up to 10^4 cycle. The improvement of endurance characteristic can be attributed to the better glass-forming ability of selenium compared to tellurium. The enhanced glass-forming ability contributes to both higher crystallization temperature and longer crystallization making the chalcogenide layer invulnerable to crystallization by high current flow and consequent Joule heating during ON state. Hence, amorphous phase can be maintained in longer cycle and the high resistance also can be retained. Serially connected 1kΩ external resistor as current limiter for extra reduction of ON current can further enhance the endurance up to 10^5 cycles as shown in Fig 3-15 (b), which guarantees highly promising cyclability for selector device application.

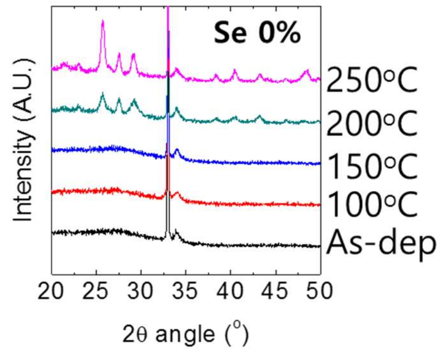

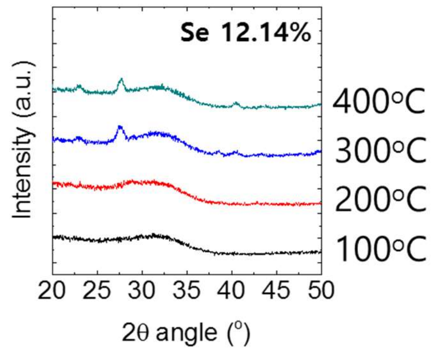

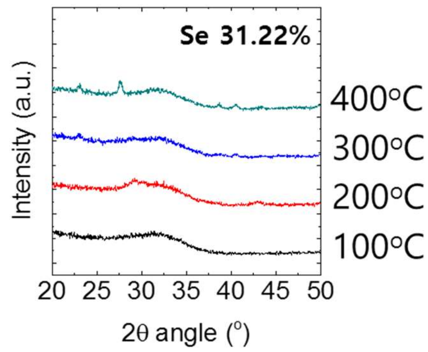

Fig 3-13. XRD results of annealed samples with various Se concentrations.

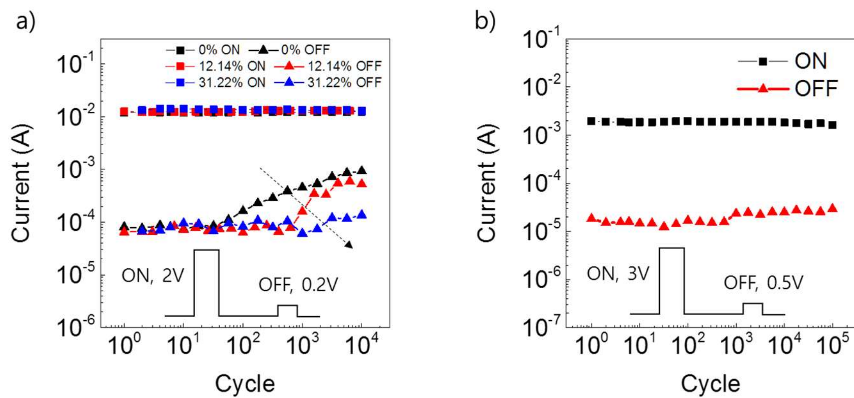

Fig 3-14. (a) The cycling endurance characteristics with respect to Se concentration and (b) enhanced endurance up to 10^5 by serially connected external resistor.

The effect of Se incorporation on the threshold field and optical bandgap was also examined. As shown in Fig 3-15 (a), threshold field does not follow same dependence to optical bandgap shown in Fig 3-15 (b) unlike the case in $GeTe_2$:Sb_2Te_3 pseudo-binary. In spite of significant change in optical bandgap up to 0.4eV, threshold field remains almost constant. The compensation of optical bandgap dependence on threshold field can be attributed to the change in distribution of localized state, which is considered to be another important factor that can greatly affect the threshold field as reported in selenide and telluride [31, 32]. It was reported that materials with similar band gaps such as GeTe, $Ge_2Sb_2Te_5$ and $Ge_{15}Te_{85}$ exhibit very different threshold fields due to the influence of localized states [31]. Thus, it can be deduced that the decrease in density of localized state counterbalanced the increase in threshold field by optical bandgap increase. This is confirmed by current-voltage curve fitting as shown in Fig 3-16, calculated by same method in Fig 3-12. Decrease in density of localized state and related increase in average distance between localized state were estimated by well-fitted current-voltage curve, reproducing the threshold fields originated from counterbalance effect of decreased distribution of localized state to increased optical bandgap.

In case of $GeTe_2$:Sb_2Te_3 pseudo-binary, the change in optical bandgap with respect to the ratio of $GeTe_2$: Sb_2Te_3 can be attributed to bonding energy difference between Ge-Te and Sb-Te. Chemical bonding of chalcogen atom, Te in this case, with atoms of IV group, Ge in this case, and V group, Sb in this

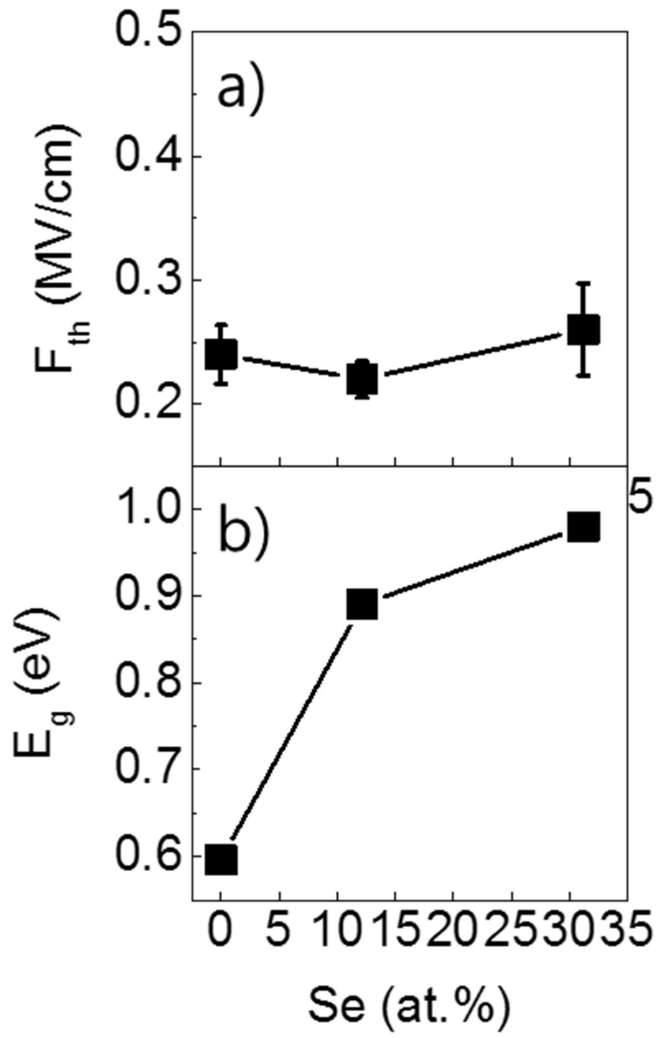

Fig 3-15. (a) Threshold field and (b) optical band with respect to Se concentration.

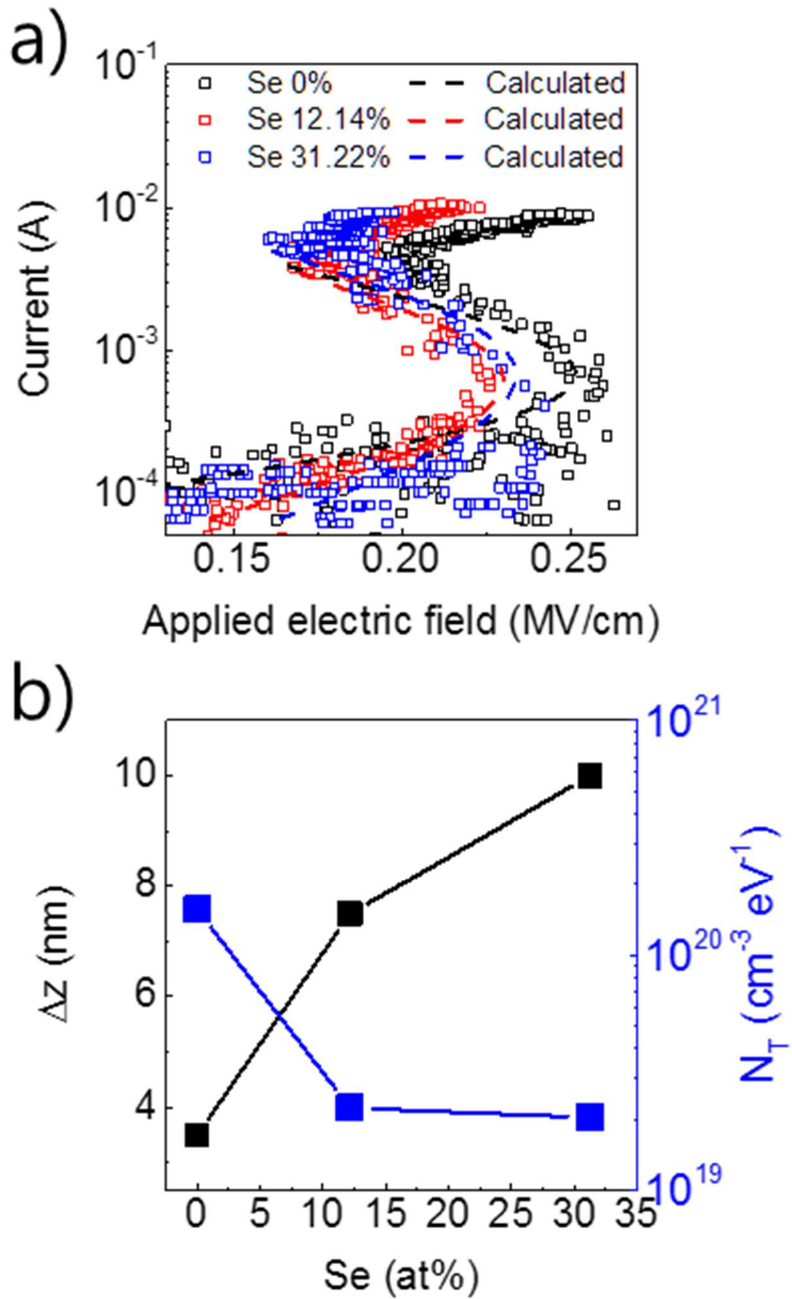

Fig 3-16. (a) Measured and calculated current-voltage curve of GSST samples and (b) fitted values regarding the distribution of localized state.

case forms a bonding molecular orbital (σ-state) and an anti-bonding molecular orbital (σ*-state) while the lone-pair electrons, or unpaired p electrons, forms non-bonding molecular orbital. Following tight binding model, the anti-bonding state in solid forms conduction band and non-bonding state forms top of the valence band while the bonding state, which have the lowest energies is located under the non-bonding state. Thus, observed optical bandgap is the difference between non-bonding state originated from the lone-pair electrons and anti-bonding state originated from the chemical bonding between Ge-Te and Sb-Te. It can be assumed that the change in valence band, which is originated from the lone-pair electrons of Te, is less significant than the change in conduction band or anti-bonding state between Ge-Te and Sb-Te since the compositional variation of Te is inconsiderable amount compared to the variation of Ge and Sb as can be seen in Table 3-5. Thus, the observed decrease in optical bandgap by increasing amount of Sb_2Te_3 can be attributed to the relative portion of weaker Sb-Te bond, or structural unit $SbTe_{2/3}$ (277.4 ± 3.8 kJ mol^{-1}) becomes dominant than stronger Ge-Te bond, or structural unit $GeTe_{4/2}$ (396.7 ± 3.3 kJ mol^{-1}). Following described tight binding model, the effect of Se incorporation on the change of optical bandgap can be accounted by similar manner. The covalent bond strength decreased with the periodicity, namely, Se forms more strong bond than Te. Thus, the increase in optical bandgap by Se incorporation can be understood to be a manifestation of

decrease in the energy separation between valence and conduction band, arising from stronger covalent bond strength.

While the origin of barely changed distribution of localized state in $GeTe_2$:Sb_2Te_3 pseudo-binary is obvious since the composition of Te which is the main source of localized states almost unchanged, the physics behind the tendency of decrease in density of localized states by Se incorporation in $GeTe_2$:Sb_2Te_3:Sb_2Se_3 pseudo-ternary is less clear due to different origin of localized states Selenide and Telluride. The localized states in Sulfides and Selenides, chalcogenide with lighter elements, can be well-explained by classical valence alternation pair model (VAP)[33]. On the other hands, the origin of localized states in Telluride is still controversial. In spite of some researches adopting VAP model to account localized state in telluride [34, 35], It is generally accepted that the localized states in Telluride cannot be solely accounted by VAP due to its more metallic nature and tendency to over-coordinate[36, 37]. It is claimed that various factors such as conduction / valence band tailing[31, 38] and Te interstitial [39] are responsible for high density of states in the gap .

3.4. Summary

In conclusion, the effect of binary film ratio in $GeTe_2$: Sb_2Te_3 pseudo-binary and $GeTe_2$: Sb_2Te_3 : Sb_2Se_3 pseudo-ternary system was evaluated. Variation in ratio of $GeTe_2$: Sb_2Te_3 leads to noticeable change in optical bandgap while the distribution of localized state barely affected, resulting change of threshold field. While, cycling endurance was not improved by adjusting binary ratio, showing poor endurance below 10^3 cycles, which is somewhat predictable since the ternary of Ge-Sb-Te is usually recognized as phase change material with high crystallization speed. In case of Se incorporation by increasing Sb_2Se_3 ratio in pseudo-ternary system, cycling endurance is significantly improved up to 10^5 cycles due to great glass-forming ability of Se. Meanwhile, threshold field was almost unchanged in contrast to evident increase in optical bandgap and decrease in density of localized state due to counterbalance effect to threshold field, as confirmed by I-V curve simulations.

3.5. Bibliography

1. Ziegler, M. M.; Stan, M. R. In *Design and analysis of crossbar circuits for molecular nanoelectronics*, Proceedings of the 2nd IEEE Conference on Nanotechnology, 2002; 2002; pp 323-327.

2. Goldstein, S. C.; Budiu, M., *SIGARCH Comput. Archit. News* **29** (2), 178-191 (2001)

3. Seok, J. Y.; Song, S. J.; Yoon, J. H.; Yoon, K. J.; Park, T. H.; Kwon, D. E.; Lim, H.; Kim, G. H.; Jeong, D. S.; Hwang, C. S., *Advanced Functional Materials* **24** (34), 5316-5339 (2014)

4. Kim, G. H.; Lee, J. H.; Ahn, Y.; Jeon, W.; Song, S. J.; Seok, J. Y.; Yoon, J. H.; Yoon, K. J.; Park, T. J.; Hwang, C. S., *Advanced Functional Materials* **23** (11), 1440-1449 (2013)

5. Burr, G. W.; Shenoy, R. S.; Virwani, K.; Narayanan, P.; Padilla, A.; Kurdi, B.; Hwang, H., *Journal of Vacuum Science & Technology B, Nanotechnology and Microelectronics: Materials, Processing, Measurement, and Phenomena* **32** (4), 040802 (2014)

6. Oh, J. H.; Park, J. H.; Lim, Y. S.; Lim, H. S.; Oh, Y. T.; Kim, J. S.; Shin, J. M.; Park, J. H.; Song, Y. J.; Ryoo, K. C.; Lim, D. W.; Park, S. S.; Kim, J. I.; Kim, J. H.; Yu, J.; Yeung, F.; Jeong, C. W.; Kong, J. H.; Kang, D. H.; Koh, G. H.; Jeong, G. T.; Jeong, H. S.; Kim, K. In *Full Integration of Highly Manufacturable 512Mb PRAM based on 90nm Technology*, 2006 International

Electron Devices Meeting, 11-13 Dec. 2006; 2006; pp 1-4.

7. Baek, I. G.; Kim, D. C.; Lee, M. J.; Kim, H. J.; Yim, E. K.; Lee, M. S.; Lee, J. E.; Ahn, S. E.; Seo, S.; Lee, J. H.; Park, J. C.; Cha, Y. K.; Park, S. O.; Kim, H. S.; Yoo, I. K.; Chung, U.; Moon, J. T.; Ryu, B. I. In *Multi-layer cross-point binary oxide resistive memory (OxRRAM) for post-NAND storage application*, IEEE InternationalElectron Devices Meeting, 2005. IEDM Technical Digest., 5-5 Dec. 2005; 2005; pp 750-753.

8. Lee, M. J.; Seo, S.; Kim, D. C.; Ahn, S. E.; Seo, D. H.; Yoo, I. K.; Baek, I. G.; Kim, D. S.; Byun, I. S.; Kim, S. H.; Hwang, I. R.; Kim, J. S.; Jeon, S. H.; Park, B. H., *Advanced Materials* **19** (1), 73-76 (2007)

9. Lee, M. J.; Park, Y.; Kang, B. S.; Ahn, S. E.; Lee, C.; Kim, K.; Xianyu, W.; Stefanovich, G.; Lee, J. H.; Chung, S. J.; Kim, Y. H.; Lee, C. S.; Park, J. B.; Baek, I. G.; Yoo, I. K. In *2-stack 1D-1R Cross-point Structure with Oxide Diodes as Switch Elements for High Density Resistance RAM Applications*, 2007 IEEE International Electron Devices Meeting, 10-12 Dec. 2007; 2007; pp 771-774.

10. Kang, B. S.; Ahn, S.-E.; Lee, M.-J.; Stefanovich, G.; Kim, K. H.; Xianyu, W. X.; Lee, C. B.; Park, Y.; Baek, I. G.; Park, B. H., *Advanced Materials* **20** (16), 3066-3069 (2008)

11. Imada, M.; Fujimori, A.; Tokura, Y., *Reviews of Modern Physics* **70** (4), 1039-1263 (1998)

12. Son, M.; Lee, J.; Park, J.; Shin, J.; Choi, G.; Jung, S.; Lee, W.; Kim,

S.; Park, S.; Hwang, H., *IEEE Electron Device Letters* **32** (11), 1579-1581 (2011)

13. Son, M.; Liu, X.; Sadaf, S. M.; Lee, D.; Park, S.; Lee, W.; Kim, S.; Park, J.; Shin, J.; Jung, S.; Ham, M. H.; Hwang, H., *IEEE Electron Device Letters* **33** (5), 718-720 (2012)

14. Gopalakrishnan, K.; Shenoy, R. S.; Rettner, C. T.; Virwani, K.; Bethune, D. S.; Shelby, R. M.; Burr, G. W.; Kellock, A.; King, R. S.; Nguyen, K.; Bowers, A. N.; Jurich, M.; Jackson, B.; Friz, A. M.; Topuria, T.; Rice, P. M.; Kurdi, B. N. In *Highly-scalable novel access device based on Mixed Ionic Electronic conduction (MIEC) materials for high density phase change memory (PCM) arrays*, 2010 Symposium on VLSI Technology, 15-17 June 2010; 2010; pp 205-206.

15. Virwani, K.; Burr, G. W.; Shenoy, R. S.; Rettner, C. T.; Padilla, A.; Topuria, T.; Rice, P. M.; Ho, G.; King, R. S.; Nguyen, K.; Bowers, A. N.; Jurich, M.; BrightSky, M.; Joseph, E. A.; Kellock, A. J.; Arellano, N.; Kurdi, B. N.; Gopalakrishnan, K. In *Sub-30nm scaling and high-speed operation of fully-confined Access-Devices for 3D crosspoint memory based on mixed-ionic-electronic-conduction (MIEC) materials*, 2012 International Electron Devices Meeting, 10-13 Dec. 2012; 2012; pp 2.7.1-2.7.4.

16. Jo, S. H.; Kumar, T.; Narayanan, S.; Nazarian, H., *IEEE Transactions on Electron Devices* **62** (11), 3477-3481 (2015)

17. Sung Hyun, J.; Kumar, T.; Narayanan, S.; Lu, W. D.; Nazarian, H. In

3D-stackable crossbar resistive memory based on Field Assisted Superlinear Threshold (FAST) selector, 2014 IEEE International Electron Devices Meeting, 15-17 Dec. 2014; 2014; pp 6.7.1-6.7.4.

18. Lee, J. H.; Kim, G. H.; Ahn, Y. B.; Park, J. W.; Ryu, S. W.; Hwang, C. S.; Kim, H. J., *Applied Physics Letters* **100** (12), 123505 (2012)

19. Anbarasu, M.; Wimmer, M.; Bruns, G.; Salinga, M.; Wuttig, M., *Applied Physics Letters* **100** (14), 143505 (2012)

20. Shin, S.-Y.; Choi, J. M.; Seo, J.; Ahn, H.-W.; Choi, Y. G.; Cheong, B.-k.; Lee, S., *Scientific Reports* **4**, 7099 (2014)

21. Lee, M.-J.; Lee, D.; Cho, S.-H.; Hur, J.-H.; Lee, S.-M.; Seo, D. H.; Kim, D.-S.; Yang, M.-S.; Lee, S.; Hwang, E.; Uddin, M. R.; Kim, H.; Chung, U. I.; Park, Y.; Yoo, I.-K., *Nature Communications* **4**, 2629 (2013)

22. Ielmini, D., *Physical Review B* **78** (3), 035308 (2008)

23. Ovshinsky, S. R., *Physical Review Letters* **21** (20), 1450-1453 (1968)

24. Yunmo, K.; Kyungjoon, B.; Hyunsang, H. In *Te-based amorphous binary OTS device with excellent selector characteristics for x-point memory applications*, 2016 IEEE Symposium on VLSI Technology, 14-16 June 2016; 2016; pp 1-2.

25. Kastner, M.; Adler, D.; Fritzsche, H., *Physical Review Letters* **37** (22), 1504-1507 (1976)

26. Burr, G. W.; Breitwisch, M. J.; Franceschini, M.; Garetto, D.; Gopalakrishnan, K.; Jackson, B.; Kurdi, B.; Lam, C.; Lastras, L. A.; Padilla, A.;

Rajendran, B.; Raoux, S.; Shenoy, R. S., *Journal of Vacuum Science & Technology B* **28** (2), 223-262 (2010)

27. Eom, T.; Choi, S.; Choi, B. J.; Lee, M. H.; Gwon, T.; Rha, S. H.; Lee, W.; Kim, M.-S.; Xiao, M.; Buchanan, I.; Cho, D.-Y.; Hwang, C. S., *Chemistry of Materials* **24** (11), 2099-2110 (2012)

28. Eom, T.; Gwon, T.; Yoo, S.; Choi, B. J.; Kim, M.-S.; Buchanan, I.; Ivanov, S.; Xiao, M.; Hwang, C. S., *Chemistry of Materials* **27** (10), 3707-3713 (2015)

29. Leskelä, M.; Pore, V.; Hatanpää, T.; Heikkilä, M.; Ritala, M.; Schrott, A.; Raoux, S.; Rossnagel, S., *ECS Transactions* **25** (4), 399-407 (2009)

30. Eom, T.; Gwon, T.; Yoo, S.; Choi, B. J.; Kim, M.-S.; Buchanan, I.; Xiao, M.; Hwang, C. S., Chemistry of Materials 26 (4), 1583-1591 (2014)

31. Luckas, J.; Krebs, D.; Grothe, S.; Carius, J.; Longeaud, C.; Wuttig, M., *Journal of Materials Research*, **28** (9), 1139 (2013)

32. Ahn, H.; Jeong, D.; Cheong, B.; Lee, H.; Lee, H; Kim, S.; Shin, S.; Kim, D.; Lee, S., *Applied Physics Letters*, **103**, 042908 (2013)

33. Kastner, M.; Adler, D.; Fritzsche, H., *Physical Review Letters*, **37** (22), 1504 (1976)

34. Pirovano, A.; Lacaita, A.L.; Benvenuti, A.; Pellizzer, F.; Bez, R., *IEEE Transactions on Electron Devices*, **51** (3), 452 (2004)

35. Nardone, M.; Simon, M.; Karpov, I.; Karpov, V., *Journal of Applied Physics*, **112** (7), 071101 (2012)

36. Robertson, J.; Xiong, K.; Peacock, P., *Thin Solid Films*, **515** (19), 7538 (2007)

37. Huang, B.; Robertson, J., *Journal of Non-crystalline Solids*, **358** (17), 2393 (2012)

38. Longeaud, C.; Luckas, J.; Krebs, D.; Carius, R.; Klomfass, J.; Wuttig, M., *Journal of Applied Physics*, **112** (11) 113714 (2012)

39. Huang, B.; Robertson, J., *Physical Review B*, **85** (12), 125305 (2012)

4. Phase change behavior of multiple layer of ultrathin $Ge_2Sb_2Te_5$ film and its application to multi-color changeable optical coating

4.1. Introduction

The high contrast in optical constant between crystalline and amorphous phases is the key property of phase change materials (PCMs) for its application in optically rewritable data storage device [1-5]. Due to its unique optical contrast, it is also widely used in various optical switching applications such as variable-focal-length lenses [6], surface plasmon waveguide [7], broadband perfect absorber [8], or tunable mid-infrared antenna[9]. In a recent study by Hosseini et al. [10], a novel concept of non-volatile color changing device based on high optical contrast of PCM has been introduced. The device comprises an ultrathin PCM film sandwiched between two transparent conducting electrodes with a reflective metal layer underneath. The bottom transparent electrode and the reflective metal functions as an interference layer and a mirror, respectively. This corresponds to the combination of the Fabry-Perot type interference effect and the so-called strong interference effect [11] which originate from the strong resonant behavior as a result of non-trivial interface phase shifts in highly absorbing ultrathin dielectric films. Fabry-Perot type interference determines the color of the device wherein the thickness of the interference layer governs the condition of constructive and destructive interferences, resulting from the

path difference of incident light reflected from the surface and the interface. In addition, ultrathin PCM layer serves as a highly absorbing dielectric layer that induces strong interference effect depending on its phase [12]. The phase transition of ultrathin PCM layer causes change in its optical constant, which leads to alteration of strong resonant behavior. The high optical constant between the two phases allows large shift in the position of the absorption peak and produces large color contrast. The fast reversibility between crystalline and amorphous phases by short time scale (~few tens of ns) electric pulses is another attributing property of PCM [4]. This enables the optoelectronic approach for micro- or nano-scale pixelated display device which holds great potential in ultrafast display or artificial retina [10].

In this study, the multi-color changeable optical coating via stacking multiple layers of ultrathin PCM film is presented. The variety of color appearances is dependent on large optical attenuation and interface phase shifts (also known as strong interference effect) of the highly absorbing PCM films with sub-wavelength thickness. The color is determined by different interference effect originating from two distinct sources: Fabry-Perot type interference from the layer consisting of optical cavity with highly reflective metal and strong interference from the highly absorbing dielectric layer. The highly absorbing dielectric film structure is composed of multiple layers of ultrathin PCM film that are separated by the thermal/diffusion barrier layer instead of single PCM film, and it is the key component of the optical device allowing multiple color

appearances in this work. Varying combination of conditions in attenuation and phase shift is achieved through stacking of multiple PCM films with selective phase transition of each PCM layer. The barrier layer guarantees the phase transition of each individual layer without any thermal or chemical disturbance between adjacent layers. Specifically, it was demonstrated that the reflective static optical coating whose color can be changed can be realized by stacking more than one layer of ultrathin (< 10nm) PCM on the substrate, consisting of transparent interference layer (indium tin oxide, ITO) and highly reflective metal (Pt). Diverse colors can be attained by combining different thicknesses of transparent interference layer and selective phase transition of PCM layers. While the thickness control of interference layer is obvious, detailed explanation of controlling the phase of the multi-layer PCM will be discussed below.

4.2. Experimental

100nm Pt mirror layer was deposited on the thermally oxidized (100 nm) Si substrate by electron-beam evaporator. ITO spacer was deposited by DC sputtering with 20W sputtering power. $Ge_2Sb_2Te_5$ layers were deposited by ALD method with showerhead type 8-inch wafer diameter compatible ALD tool using $Ge(OEt)_4$, $Sb(OEt)_3$, $(Me_3Si)_3Sb$, and $(Me_3Si)_2Te$ precursors, where Et and Me represent the ethyl and methyl group. The composition of GST layer was confirmed by X-ray fluorescence (Thermo scientific). Ta_2O_5 layer was deposited by another ALD tool using $Ta(N^tBu)(NEt_2)_2Cp$ and H_2O as the Ta-precursor and oxygen source, respectively. Bu represents buthyl group whereas Cp denotes cycloropentadienyl group. The structural properties were analyzed by transmission electron microscopy (JEOL, JEM-2100F). TEM sample was prepared by focused ion beam (FEI, Helios 650). The optical constants of films were measured by spectroscopic ellipsometry (J.A.Woolam, ESM-300). Relatively thick (~30nm) GST film deposited by the same ALD process on Si substrate was used for the measurement. The reflectance spectra of the samples were measured by UV-Vis spectrophotometer (Varian Inc., Cary 5000) in reflection mode using wavelengths between 350nm and 750nm. Transfer-matrix method using MATLAB code developed and used by McGehee[20] was employed for reflectance spectra simulations. Atomic force microscopy (JEOL, JSPM-5200) and Pt/Ir coated Si conductive tip were used for electrically drawing patterns in conductive AFM mode. Magnified images were obtained

by confocal laser scanning microscope (Carl Zeiss, LSM710) using 633nm laser.

4.3. Results and Discussions

The mechanism of selective crystallization is schematically depicted in Fig 4-1 (a). When multiple PCMs with different crystallization temperatures (T_c) are separated by a thin thermal barrier, it is possible to attain multiple state of phases by controlling the intensity of the external stimuli (i.e., heat, current, or laser). The different crystallization temperatures can be obtained, for instance, by doping of impurity such as nitrogen [13] or changing the thickness of the film [14-15]. For the PCM film thinner than ~10 nm, T_c is significantly increased with decreasing film thickness [16]. For this work, $Ge_2Sb_2Te_5$ (GST) film grown by an atomic layer deposition (ALD) technique was utilized as the PCM owing to its accurate thickness control down to sub-nm over a large-area substrate [17]. Furthermore, incorporating such ultrathin PCM film is suitable for the color device since the efficiency of the color changing is enhanced below 20 nm [10]. The doping in ALD was not attempted for this experiment on account of its complicated process even though the doping of GST with impurity has been exploited in semiconductor memory devices [18]. Consequently, two ultrathin GST films with different thicknesses (8 nm and 5 nm) were implemented as the top and bottom layers (TL and BL) to realize multi-state phase combinations. For the initial state, the two GST films are at amorphous (as-deposited) phase. When a moderate external stimulus, such as low annealing temperature, is applied, only the thicker film with lower T_c will be selectively crystallized given that two films are separated by a thermal

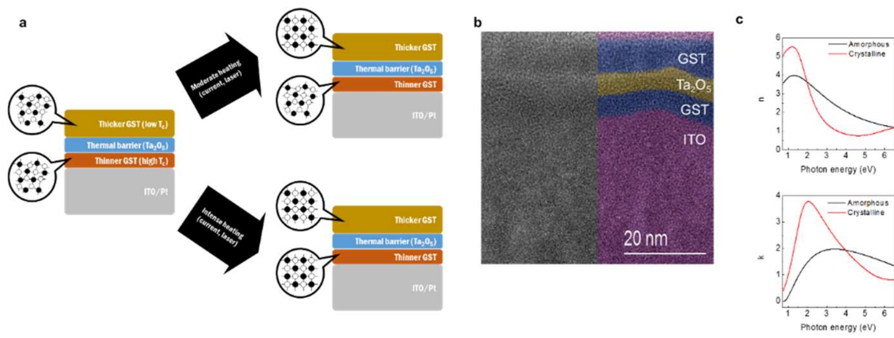

Fig 4-1. (a) Schematics depicting operation mechanism for selective crystallization and multiple optical state. (b) False color TEM image of the fabricated optical coating with two distinct GST layers separated by Ta_2O_5 which functions as a thermal/diffusion barrier. Only half of the image was colored for clarity. (c) Measured optical constants of GST film by spectroscopic ellipsometry.

barrier, 6 nm-thick Ta_2O_5 film, in this case. Due to high contrast in optical constant between amorphous and crystalline phases in GST film, the crystallization of only one layer will bring about a significant change in the optical properties of the device. When an intense external stimulus, such as high annealing temperature, is applied, both films will be crystallized and optical properties of the device will be substantially changed again, generating a different color. With this collective operation scheme, n+1 different optical states can be achieved by n different layers of phase change materials since individual access of each layer is impossible. For example, only top and bottom electrodes are necessary to address three states in double layer system (amorphous/amorphous, amorphous/crystalline, and crystalline/crystalline), where the highest current will induce amorphization of both layers for the first state, and low and medium current will crystallize one or both layers for second and third state, respectively.

To evaluate the feasibility of multi-state color changing, the devices with two GST layers deposited on ITO (150 nm and 200 nm)/ Pt substrate were fabricated and annealed at different temperatures to induce selective crystallization. Fig 4-1 (b) shows a false color cross-sectional image of the device configuration using a bright field transmission electron microscopy (TEM). The thickness of two different GST layers and Ta_2O_5 is 5 nm, 8 nm, and 6 nm, respectively. The flat and uniform deposition of ultrathin GST film was obtained by ALD process, which was critical in achieving the desired optical

properties. The details of ALD process is reported elsewhere [19]. Fig 4-1 (c) shows the measured optical constants of GST film deposited by the ALD process. Ta_2O_5 film was deposited by another ALD method to also ensure sufficiently smooth and uniform film at a temperature of 150ºC; the temperature was low enough to dissuade the crystallization of BL GST. Through careful observation of color variation in the device, with regards to change in temperature, the crystallization temperature of the thinner and thicker GST films was found to be around 200ºC and 250ºC, corresponding to the first and the second notable color changes. Under these circumstances, the annealing condition was determined to be 210ºC for only TL and 260ºC for both TL and BL in air for 30 min. When considering the crystallization temperature of bulk GST (~150℃), this seems abnormally high. The measured composition as well as the measured optical constants in Fig 4-1 © clearly indicates that deposited film is GST, which suggests there may be other reasons for the discrepancy in crystallization temperature. One possible explanation is the influence of interface layer such as ITO and Ta_2O_5 since GST is a nucleation-dominant material and its crystallization is strongly dependent on its interface material [16] as the film thickness is reduced to sub-nm level while the proportion of the surface becomes dominant. Fig 4-2 shows a photograph of annealed samples taken with a digital camera wherein six samples, named as (a) – (f), are shown. Samples a, c, and e are the devices with the 150nm thickness ITO layer whereas samples b, d, and f are the devices with 200 nm thickness ITO layer. Samples a

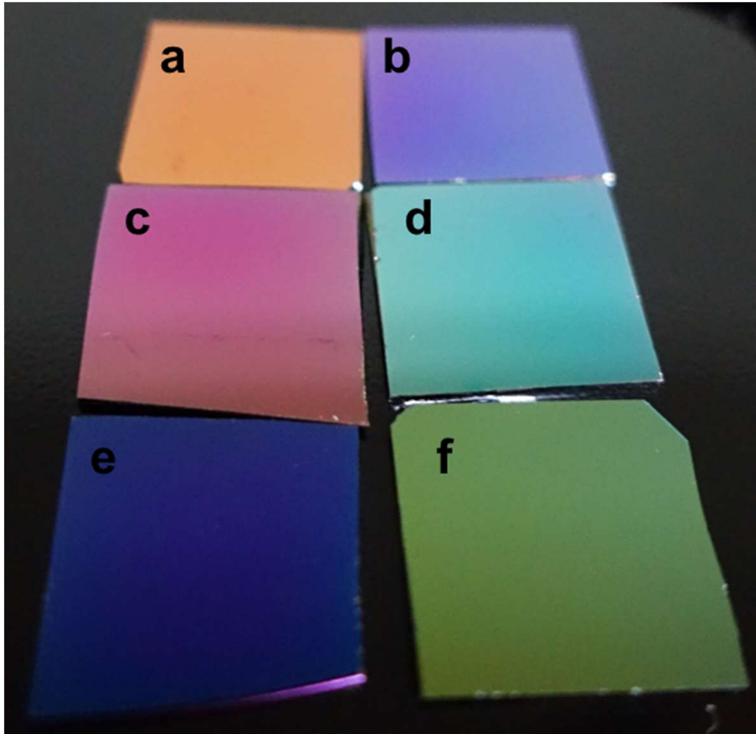

Fig 4-2. Photograph of c/c samples annealed at 260℃ (a) & (b), α/c samples annealed at 210℃ (c) & (d), and α / α samples as-fabricated (e) & (f). (a), (c), (e) has 150nm thick ITO layers while (b), (d), (f) has 200nm thick ITO layers.

and b, having been annealed at 260ºC, are composed of two crystallized GST layers (denoted as c/c). For samples c and d, one amorphous (thin) GST layer with one crystallized (thick) GST layer (denoted as α/c) were obtained at annealing temperature of 210ºC. Samples e and f contain two amorphous GST layers since they were as-fabricated (denoted as α/α). As illustrated in the photograph, the selective phase transition of each GST layer resulted in clearly distinguishable color change. In addition, samples with dissimilar ITO thickness featured completely different colors even with the same configuration of GST layers. This implies that the change in ITO thickness results in the alteration of color which would be modulated afterwards by the phases of the GST layers.

The change in reflectance was measured by an optical spectrometer to quantify the multiple color states and its color changing tendencies. Fig 4-3 (a) and (b) display measured reflectance of the samples with different ITO spacer layer thicknesses of 150nm and 200nm for the α/α, α /c, and c/c configurations. Note that the difference in thicknesses of ITO spacer layer resulted in shifting the position of maxima and minima of the reflectance spectra. In Fig 4-3 (a), the reflectance curves and its shift tendency with respect to the selective crystallization of each GST layer for ITO 150nm sample are presented. When both GST layers are amorphous, the first reflectance maxima appear at the wavelength range between 425nm and 450nm. The selective crystallization of thick GST layer leads to a shift of reflectance curve towards the region of

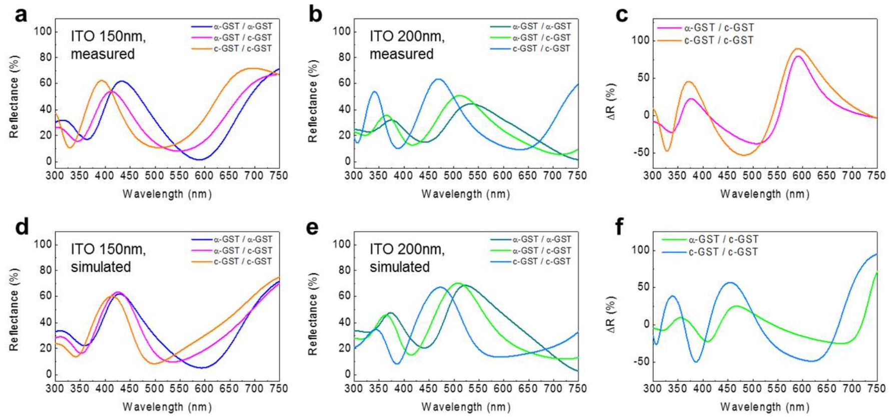

Fig 4-3. The measured reflectance spectra for (a) ITO 150nm samples and (b) ITO 200nm samples. Simulated reflectance spectra for (d) ITO 150nm and (e) 200nm, respectively. The measured ΔR values for (c) ITO 150nm and (f) 200nm.

shorter wavelengths. When both GST layers are crystallized, the reflectance curve is further shifted to shorter wavelengths. The same behavior is also shown in the samples with 200nm-thick ITO as illustrated in Fig 4-3 (b). The calculated reflectance spectra using transfer-matrix method [20] can be seen in Fig 4-3 (d) and 4-3 (e). The optical constant of each layer was obtained by spectroscopic ellipsometry while the thickness of each layer was determined by the TEM measurement. Despite slight discrepancy of the absolute values of reflectance spectra between the measured and the simulated curves, possibly due to the inaccuracy in the simulation of the multi-layered structure as well as probable thermal and chemical interferences, the tendency of shifting towards shorter wavelengths can be clearly demonstrated, corroborating the experimental results.

The shift of reflectance curve by phase transition of GST layers results in a significant contrast in reflectance at a given wavelength, and is defined as ΔR (%) = $100 \times (R_x - R_{\alpha/\alpha}) / (R_x + R_{\alpha/\alpha})$, where $R_{\alpha/\alpha}$ stands for the reflectance of the α/α sample and R_x represents the reflectance for c/c sample ($R_{c/c}$) or α/c sample ($R_{\alpha/c}$). ΔR between α/c and α / α samples with 150 nm-thick ITO was 80 % at its peak while between α/α and c/c samples was even high as 90% at the wavelength near 580nm (Fig 4-3 (c)). Similar ΔR was also attained from the samples with 200 nm-thick ITO layer (Fig 4-3 (f)). This suggests that successive phase transition of the ultrathin GST layer can contribute to notable change in reflectance and concomitant color alteration.

As it was verified in Fig 4-3, optical simulations provided a reasonable match with the experimental results. Therefore, additional simulations were carried out to validate the feasibility of various color expressions by stacking more than two layers of GST film. The thickness of the thinnest GST layer was set to 2nm and the thickness of each additional GST layers being stacked was incremented by 2nm with respect to the previous GST layer, guaranteeing significant crystallization temperature difference[14-16]. Every GST layers was separated by 5nm thick Ta_2O_5 layer, which was taken into consideration for the optical simulations. As it was previously stated, n GST layer always equals n+1 color state; hence, increase in number of GST layers may lead to further expressible colors. Moreover, increasing the number of GST layer corresponds to increase in total GST thickness which can cause reduction appertaining to the contrast in total reflectance of color changing [10,12]. This trade-off tendency is well-portrayed in Fig 4-4. The increase in number of amorphous GST layer rarely reduces the reflectance as it can be seen in Fig 4-4 (a). Instead, more amorphous GST layers caused reflectance peak shifts toward longer wavelength region, making it possible to exhibit a larger variation of expressible color. This can be confirmed by the change in reflectance of all amorphous state in regards to all crystalline state for multi-layer of GST as shown in Fig 4-4 (b). In contrast, as displayed in Fig 4-4 (c), increase in number of crystalline GST layer led to a general decrease in absorption peak intensity around 350nm and 500nm wavelength region, wherein renders the characteristic color of device to

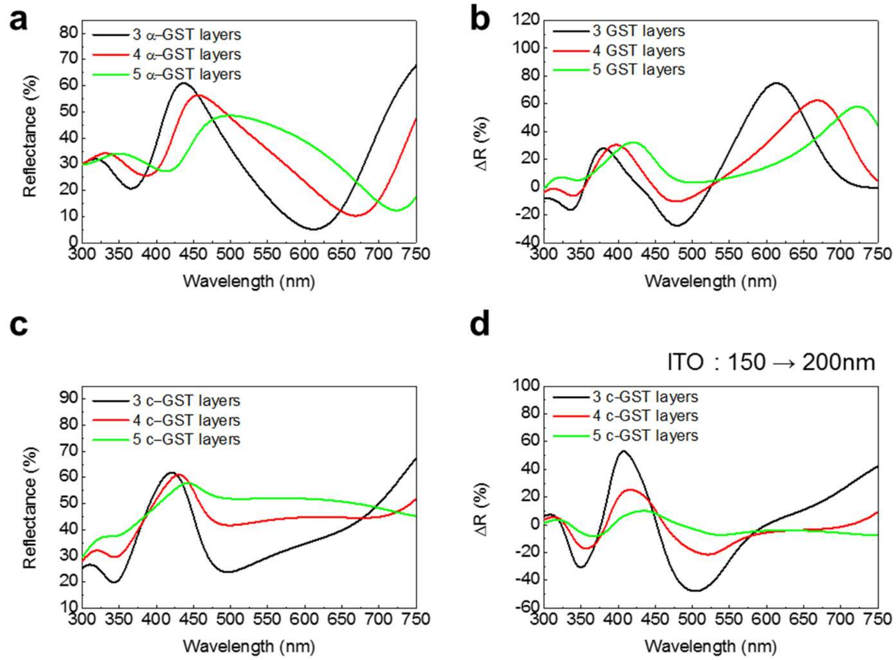

Fig 4-4. (a) Simulated reflectance spectra for multi-layer with all amorphous configuration. (b) ΔR between all amorphous and all crystalline configuration with increasing number of layers. (c) Simulated reflectance spectra for all crystalline configuration. (d) ΔR with respect to ITO spacer thickness variation for all crystalline configuration.

disappear and converge into a metallic silver color. For example, stacking of 5 crystalline GST layers produced almost same level of reflectance in the whole visible wavelength region. It indicates that at some point the contrast in color will be reduced to an indistinguishable level, making it impractical to add more GST layers. This can be observed when ITO layer thickness was altered from 150nm to 200nm as shown in Fig 4-4 (d). In this case, when there were 3 crystalline GST layers, ΔR of 60% was achieved by altering the thickness of ITO. However, the addition of 2 extra crystalline GST layers resulted in lowering the ΔR below 10%.

For the application in nanoscale optoelectronic display and optical storage devices, the practicality of multi-state optical recording with micrometer scale was demonstrated by using conductive atomic force microscopy (CAFM) [21]. Fig 4-5 (a) shows the schematic setup of CAFM test. By applying bias to the ITO spacer layer that acts as bottom electrode while the Pt/Ir-coated Si CAFM tip is grounded, current can flow from the tip to the bottom ITO through the GST layers in the absence of top electrode. It should be noted that the top transparent electrode was not deposited or considered in previous optical measurement/simulation in order to be coherent with CAFM results. When the current is high enough to induce sufficient Joule heating, the selected region could be crystallized and the image would be recorded. Simple square patterns were drawn on the double GST layer device with 150nm ITO spacer layer. After the writing process, confocal laser scanning microscope (CLSM) with 633nm

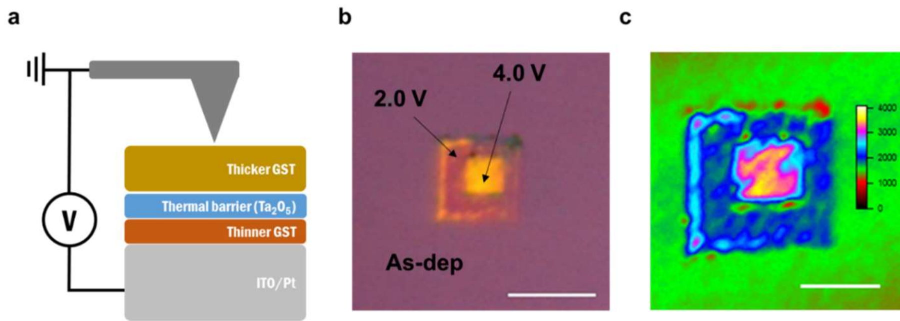

Fig 4-5. (a) Schematic of measurement setup for CAFM. (b) Optical microscope image (Scale bar: 10μm) and (c) CLSM image (Scale bar: 5μm) of recorded.

laser was used to observe the recorded patterns. Square patterns with 9×9μm^2 and 3.5×3.5μm^2 were recorded with applied voltages of 2.0V and 4.0V, respectively, to achieve different optical state by selective crystallization. The speed of the tip scan was 3.54 μm/s. 9×9 μm^2 pattern was recorded initially by 2.0V bias and 3.5×3.5 μm^2 pattern was recorded afterward by 4.0V bias at the center of 9×9 μm^2 square. Fig 4-5 (b) and (c) illustrate the optical microscope and CLSM images of recorded patterns. The mismatch in color impression of corresponding optical state between Fig 4-2 and Fig 4-5 (b) may originate from the condition of optical microscope or the difference in circumstance of illumination. Therefore, the similarity in color does not necessarily mean the same optical state. The patterns showed obvious reflectance change from the background, and the change in reflectance also varied accordingly with the bias voltage. As stated by previous discussions on the correlation between the reflectance and crystallization of the two GST layers, it can be inferred that thicker GST layer was crystallized at 2.0V bias whereas both GST layers were crystallized at 4.0V bias. These results indicate the feasibility of very fine scale image recording despite the data presented in Fig 4-5 are not in optimal quality due to the relatively uncontrolled environment of the laboratory.

One concern about the role of thermal barrier Ta_2O_5 layer in such optoelectronic operation is its possible thermal insulation effect during the reset (amorphization) process, which will adversely interfere with the amorphization during actual device operation. Nonetheless, in actual device structure, the two

GST layers must be in contact with both the top and the bottom electrodes, which may play a role as the heat-dissipation paths and enhance the amorphization. Even though the reset-back process in the device of this study was not feasible due to its thermally unfavorable structure design, further structural or material modifications, having been extensively explored in phase change memory field, can be adopted to further mitigate such possible problem. Under such circumstance, the unfavorable aspect of the thermal barrier layer could be minimized.

4.4. Summary

In summary, optical coating which can express multiple colors through external stimuli was demonstrated. It was shown that the multi-layered optical coating can express multiple colors by either heating (annealing) or applying current even in micrometer scale. The measured spectra of multi-colored devices are in good agreement with simulated reflectance spectra. Additional simulation results revealed that increase in number of GST layer leads to increase in variety of expressible colors. However, there is a limitation in the number of acceptable layers due to decrease in reflectance peak intensity. The multiple optical state of GST layer can be utilized not only for optical coating or optoelectronic display devices, but also for the optical storage that can effectively increase the data density via multi-level recording.

4.5. Bibliography

1. Chen, M.; Rubin, K. A.; Barton, R. W., *Appl. Phys. Lett.* **49** (9), 502-504 (1986)

2. Noboru, Y.; Eiji, O.; Nobuo, A.; Ken'ichi, N.; Ken'ichi, N.; Masatoshi, T., *Jpn. J. Appl. Phys.* **26** (S4), 61 (1987)

3. Afonso, C. N.; Solis, J.; Catalina, F.; Kalpouzos, C., *Appl. Phys. Lett.* **60** (25), 3123-3125 (1992)

4. Wuttig, M.; Yamada, N., *Nat. Mater.* **6** (11), 824-832 (2007)

5. Huang, B.; Robertson, J., *Phys. Rev. B* **81** (8), 081204 (2010)

6. Wang, Q.; Rogers, E. T. F.; Gholipour, B.; Wang, C.-M.; Yuan, G.; Teng, J.; Zheludev, N. I., *Nat Photon* **10** (1), 60-65 (2016)

7. Rudé, M.; Simpson, R. E.; Quidant, R.; Pruneri, V.; Renger, J., *ACS Photonics* **2** (6), 669-674 (2015)

8. Cao, T.; Wei, C.-w.; Simpson, R. E.; Zhang, L.; Cryan, M. J., *Scientific Reports* **4**, 3955 (2014)

9. Michel, A.-K. U.; Chigrin, D. N.; Maß, T. W. W.; Schönauer, K.; Salinga, M.; Wuttig, M.; Taubner, T., *Nano Letters* **13** (8), 3470-3475 (2013)

10. Hosseini, P.; Wright, C. D.; Bhaskaran, H., *Nature* **511** (7508), 206-211 (2014)

11. Kats, M. A.; Blanchard, R.; Genevet, P.; Capasso, F., *Nat. Mater.* **12** (1), 20-24 (2013)

12. Schlich, F. F.; Zalden, P.; Lindenberg, A. M.; Spolenak, R., *ACS Photonics* **2** (2), 178-182 (2015)

13. Gyanathan, A.; Yeo, Y.-C., *J. Appl. Phys.* **110** (12), 124517 (2011)

14. Raoux, S.; Jordan-Sweet, J. L.; Kellock, A. J., *J. Appl. Phys.* **103** (11), 114310 (2008)

15. Simpson, R. E.; Krbal, M.; Fons, P.; Kolobov, A. V.; Tominaga, J.; Uruga, T.; Tanida, H., *Nano Letters* **10** (2), 414-419 (2010)

16. Cheng, H.-Y.; Raoux, S.; Chen, Y.-C., *J. Appl. Phys.* **107** (7), 074308 (2010)

17. George, S. M., *Chem. Rev.* **110** (1), 111-131 (2010)

18. Horii, H.; Yi, J. H.; Park, J. H.; Ha, Y. H.; Baek, I. G.; Park, S. O.; Hwang, Y. N.; Lee, S. H.; Kim, Y. T.; Lee, K. H.; Chung, U. I.; Moon, J. T. In *A novel cell technology using N-doped GeSbTe films for phase change RAM*, Tech. Dig. VLSI Symp., 10-12 June 2003; 2003; pp 177-178.

19. Eom, T.; Gwon, T.; Yoo, S.; Choi, B. J.; Kim, M.-S.; Buchanan, I.; Ivanov, S.; Xiao, M.; Hwang, C. S., *Chem. Mater.* **27** (10), 3707-3713 (2015)

20. Burkhard, G. F.; Hoke, E. T.; McGehee, M. D., *Adv. Mater.* **22** (30), 3293-3297 (2010)

21. Bhaskaran, H.; Sebastian, A.; Pauza, A.; Pozidis, H.; Despont, M., *Rev. Sci. Instrum.* **80** (8), 083701 (2009)

5. Conclusion

In this thesis, electrical switching phenomenon in amorphous chalcogenide, particularly for Ge-Sb-Te ternary or Ge-Sb-Te-Se quaternary system were studied. Among various electrical switching behavior observed in chalcogenide, solid electrolytic switching behavior and ovonic threshold switching behavior are focused. In addition, change in optical properties of amorphous chalcogenide by induced electric field and its application as a color-changeable optical device is presented.

Detailed mechanism study for solid electrolytic switching behavior in $Ge_2Sb_2Te_5$ ternary system revealed that anomalous polarity-dependent resistive switching behavior without active metal can be attributed to forming and rupture of conductive filament due to migration of ionized Te in high electric field. The feasibility of application on ReRAM device is promising in terms of its device performance such as resistance ratio or reliability.

Intensive study on compositional variation effect on ovonic threshold switching behavior in atomic-layer-deposited Ge-Sb-Se-Te quaternary system provide the method of parameter engineering, particularly for threshold field, as well as switching endurance, satisfying the requirement for the selector device in 1S1R CBA architecture. Adjusting ratio of Ge/Sb leads to change in threshold field while effect on switching endurance is ignorable. Increase in Se contents leads to improvement in switching endurance while threshold field

rarely changed in spite of significant change in electronic structure, which can be attributed to counterbalance between optical bandgap and distribution of localized state.

Finally, change in optical properties and consequent color change in double-stacked multi-layer device adopting amorphous $Ge_2Sb_2Te_5$ with different thickness is presented. Multiple color expression enabled by adjusting the degree of external stimuli are reproduced by transfer-matrix method optical simulation and shown to be scaled down to micrometer size.

This study not only suggests new applications of Ge,Sb-based chalcogenide, which is usually considered as phase change materials, for next-generation memory elements as well as optical device but also contributes further understanding of electrical switching behavior in amorphous chalcogenide.

Curriculum Vitae

Sijung Yoo

Department of Materials Science and Engineering

College of Engineering

Seoul National University

1 Gwanak-ro, Gwanak-gu, Seoul 151-742, Korea

E-mail: isobel@snu.ac.kr

Tel.: +82-2-880-8643

Fax.: +82-2-880-8643

I. Educations

2006. 3. - 2012. 2. B.S.

Department of Materials Science and Engineering

Seoul National University, Seoul, Korea

2012. 3 – 2014. 2. M.S. Course

Department of Materials Science and Engineering

Seoul National University, Seoul, Korea

2014. 3 – 2019. 2. Ph.D. Course

Department of Materials Science and Engineering

Seoul National University, Seoul, Korea

II. Research Areas

1. **Resistive switching phenomenon**

- Resistive switching in oxide and chalcogenide thin films

2. **Thin film deposition for chalcogenide materials**

- Deposition of Ge-Sb-Te and Ge-Sb-Se-Te multicomponent system

3. **Microstructure analysis of thin film**

- Structural and chemical analysis through Transmission Electron Microscopy

4. **Resistive switching / Phase change memory device fabrication**

- Deposition / etching / lithography / electrical characterization

III. Experimental Skills

1. **Deposition methods**

- Atomic layer deposition for chalcogenide materials
- DC & RF magnetron sputtering
- E-beam evaporation for electrode
- Handling and maintenance of high vacuum equipment

2. **Sample preparation**

- Photo-lithography
- Conventional furnace annealing for ambient and vacuum annealing

- TEM sampling (Focused Ion Beam / Precision Ion Polishing System)

3. Analysis methods

- Transmission Electron Micrioscopy (JEOL JEM-2100F) for microstructure analysis of thin film
- X-Ray Fluorescence Analyzer (XRF, Thermo scientific, ART Quant'X EDXRF) for analysis of composition and layer density of film
- X-ray Diffractometer (PANalytical, X'Pert PRO MPD) for measurement of X-ray diffraction, X-ray reflection and reciprocal space mapping.
- Atomic Force Microscopy (AFM, JEOL, JSPM-5200) for analysis of the topography
- Spectroscopic Ellipsometer (SE, J.A. Woollam, M-2000) for analysis of optical properties and thicknesses of thin films
- Four-point probe for resistivity measurement of metals and conducting materials
- Pulse/pattern generator (Agilent, 81110A/81111A) and digital oscilloscope for pulse switching measurement
- HP4140B and HP4145B for I-V characterization

List of publications

1. Refereed Journal Articles (SCI)

1.1 Domestic

1.2. International

1. Taeyong Eom, Taehong Gwon, **Sijung Yoo**, Byung Joon Choi, Moo-Sung Kim, Iain Buchanan, Manchao Xiao, and Cheol Seong Hwang, "Influence of the Kinetic Adsorption Process on the Atomic Layer Deposition Process of $(GeTe_2)_{(1-x)}(Sb_2Te_3)_x$ Layers Using Ge^{4+}–Alkoxide Precursors", Chemistry of Materials, 4, 26, 1583-1591 (2014)
2. Woojin Jeon, **Sijung Yoo**, Hyo Kyeom Kim, Woongkyu Lee, Cheol Hyun An, Min Jung Chung, Cheol Jin Cho, Seong Keun Kim, and Cheol Seong Hwang, "Evaluating the Top Electrode Material for Achieving an Equivalent Oxide Thickness Smaller than 0.4 nm from an Al-Doped TiO_2 Film", ACS Applied Materials & Interfaces, 23, 6, 21632-21367 (2014)

3. Taeyong Eom, Taehong Gwon, **Sijung Yoo**, Byung Joon Choi, Moo-Sung Kim, Sergei Ivanov, Andrew Adamczyk, Iain Buchanan, Manchao Xiao, Cheol Seong Hwang, “Chemical interaction and ligand exchange between $[(CH_3)_3Si]_3Sb$ precursor and atomic layer deposited Sb_2Te_3 films”, Journal of Materials Chemistry C, 3, 1365-1370 (2015)
4. **Sijung Yoo**, Taeyong Eom, Taehong Gwon and Cheol Seong Hwang, “Bipolar resistive switching behavior of an amorphous $Ge_2Sb_2Te_5$ thin films with a Te layer”, Nanoscale, 7, 6340-6347 (2015)
5. Taeyong Eom, Taehong Gwon, **Sijung Yoo**, Byung Joon Choi, Moo-Sung Kim, Iain Buchanan, Sergei Ivanov, Manchao Xiao, and Cheol Seong Hwang, “Combined Ligand Exchange and Substitution Reactions in Atomic Layer Deposition of Conformal $Ge_2Sb_2Te_5$ Film for Phase Change Memory Application”, Chemistry of Materials, 10, 27, 3707-3713 (2015)
6. Xing Long Shao, Li Wei Zhou, Kyung Jean Yoon, Hao Jiang, Jin Shi Zhao, Kai Liang Zhang, **Sijung Yoo**, and Cheol Seong Hwang, “Electronic resistance switching in the Al/TiO_x/Al structure for forming-free and area-scalable memory”, Nanoscale, 7, 11063-11074 (2015)
7. Woongkyu Lee, **Sijung Yoo**, Woojin Jeon, Yeon Woo Yoo, Cheol Hyun An, Min Jung Chung, Han Joon Kim, SangWoon Lee, and Cheol Seong Hwang, “Reducing the nano-scale defect formation of atomic-layer-deposited $SrTiO_3$ films by adjusting the cooling rate of the crystallization annealing of the seed layer”, Thin Solid Films, 589, 723-729 (2015)

8. An Quan Jiang, Xiang Jian Meng, David Wei Zhang, Min Hyuk Park, **<u>Sijung Yoo</u>**, Yu Jin Kim, James F. Scott, and Cheol Seong Hwang, "Giant Dielectric Permittivity in Ferroelectric Thin Films: Domain Wall Ping Pong", Scientific Reports, 5, 14618 (2015)
9. Woongkyu Lee, **<u>Sijung Yoo</u>**, Kyung Jean Yoon, In Won Yeu, Hye Jung Chang, Jung-Hae Choi, Susanne Hoffmann-Eifert, Rainer Waser, and Cheol Seong Hwang, "Resistance switching behavior of atomic layer deposited $SrTiO_3$ film through possible formation of $Sr_2Ti_6O_{13}$ or $Sr_1Ti_{11}O_{20}$ phases", Scientific Reports, 6, 20550 (2016)
10. **<u>Sijung Yoo</u>**, Taehong Gwon, Taeyong Eom, Sanggyun Kim, and Cheol Seong Hwang, "Multicolor Changeable Optical Coating by Adopting Multiple Layers of Ultrathin Phase Change Material Film", ACS Photonics, 3, 7, 1265 (2016)
11. Jung Ho Yoon, **<u>Sijung Yoo</u>**, Seul Ji Song, Kyung Jean Yoon, Dae Eun Kwon, Young Jae Kwon, Tae Hyung Park, Hye Jin Kim, Xing Long Shao, Yumin Kim, and Cheol Seong Hwang, "Uniform Self-rectifying Resistive Switching Behavior via Preformed Conducting Paths in a Vertical-type Ta_2O_5/HfO_{2-x} Structure with a Sub-μm^2 Cell Area", ACS Appl. Mater. Interfaces, 20, 8, 18215 (2016)
12. Taehong Gwon, Taeyong Eom, **<u>Sijung Yoo</u>**, Han-Koo Lee, Deok-Yong Cho, Moo-Sung Kim, Iain Buchanan, Manchao Xiao, Sergei Ivanov, and Cheol Seong Hwang, "Atomic Layer Deposition of GeTe Films Using $Ge[N[Si(CH_3)_3]_2]_2$, $[(CH_3)_3Si]_2Te$, and Methanol", Chemistry of Materials, 28, 19, 7158-7166 (2016)

13. Kyung Jean Yoon, Gun Hwan Kim, **Sijung Yoo**, Woorham Bae, Jung Ho Yoon, Tae Hyung Park, Dae Eun Kwon, Yeong Jae Kwon, Hae Jin Kim, Yu Min Kim, and Cheol Seong Hwang, "Double-Layer-Stacked One Diode-One Resistive Switching Memory Crossbar Array with an Extremely High Rectification Ratio of 10^9", Advanced Electronic Materials, DOI: 10.1002/aelm.201700152 (2017)
14. Taehong Gwon, Taeyong Eom, **Sijung Yoo**, Chanyoung Yoo, Eui-sang Park, Sanggyun Kim, Moo-Sung Kim, Iain Buchanan, Manchao Xiao, Sergei Ivanov, and Cheol Seong Hwang, "Atomic Layer Deposition of GeTe and Ge–Sb–Te Films Using $HGeCl_3$, $Sb(OC_2H_5)_3$, and $\{(CH_3)_3Si\}_2Te$ and Their Reaction Mechanisms", Chemistry of Materials, DOI:10.1021/acs.chemmater.7b01236 (2017)
15. Taehong Gwon, Ahmed Yousef Mohamed, Chanyoung Yoo, Eui-sang Park, Sanggyun Kim, **Sijung Yoo**, Han-Koo Lee, Deok-Yong Cho,, and Cheol Seong Hwang, "Structural Analyses of Phase Stability in Amorphous and Partially Crystallized Ge-Rich GeTe Films Prepared by Atomic Layer Deposition", ACS Appl. Mater. Interfaces, DOI: 10.1021/acsami.7b12946 (2017)
16. Yumin Kim, Young Jae Kwon, Dae Eun Kwon, Kyung Jean Yoon, Jung Ho Yoon, **Sijung Yoo**, Hae Jin im, Tae Hyung Park, Jin-Woo Han, Kyung Min Kim, and Cheol Seong Hwang, "Nociceptive Memristor", Advanced Materials, 30, 8, 1704320 (2018)

17. **Sijung Yoo**, Chanyoung Yoo, Eui-Sang Park, Woohyun Kim, Yoon Kyeung Lee and Cheol Seong Hwang, “Chemical Interactions in Atomic Layer Deposition of Ge-Sb-Se-Te Films and Their Ovonic Threshold Switching Behavior”, J. Mater. Chem. C., 6, 5025-5032 (2018)

18. Woohyun Kim, **Sijung Yoo**, Chanyoung Yoo, Eui-Sang Park, Jeongwoo Jeon, Young Jae Kwon, Kyung Seok Woo, Han Joon Kim, Yoon Kyeung Lee and Cheol Seong Hwang, “Atomic layer deposition of GeSe films using $HGeCl_3$ and $[(CH_3)_3Si]_2Se$ with the discrete feeding method for the ovonic threshold switch”, Nanotechnology, 29, 365202 (2018)

19. Woongkyu Lee, Cheol Hyun An, **Sijung Yoo**, Woojin Jeon, Min Jung Chung, Sang Hyeon Kim, and Cheol Seong Hwang, “Electrical Properties of ZrO2/Al2O3/ZrO2-Based Capacitors with TiN, Ru, and TiN/Ru Top Electrode Materials”, Phys. Status Solidi RRL, 12, 10, 1800356 (2018)

20. Hehe Zhang, **Sijung Yoo**, Stephan Menzel, Carsten Funck, Felix Cüppers, Dirk J. Wouters, Cheol Seong Hwang, Rainer Waser, and Susanne Hoffmann-Eifert, “Understanding the Coexistence of Two Bipolar Resistive Switching Modes with Opposite Polarity in Pt/TiO2/Ti/Pt Nanosized ReRAM Devices”, ACS Appl. Mater. Interfaces, 10, 35, 29766–29778 (2018)

2. CONFERENCES

2.1 Domestic

1. Taeyong Eom, Taehong Gwon, **Sijung Yoo**, Seol Choi, Byung Joon Choi, Moo-sung Kim, Iain Buchanan, Manchao Xiao, and Cheol Seong Hwang, “Atomic layer deposition characteristics of $(GeTe2)_{(1-x)}(Sb_2Te_3)_x$ layers for Phase change memories”, 제 20회 한국 반도체 학술대회, 성우리조트, 2013년 2월 4일-6일, Oral
2. Taehong Gwon, Taeyong Eom, **Sijung Yoo**, Moo-Sung Kim, lain Buchanan, Manchao Xiao, and Cheol Seong Hwang, “A New Chemical Route for Vapor Phase Deposition of GeTe for Phase Change Memory”, 제 21 한국 반도체 학술대회, 한양대학교, 2014년 2월 24일-26일, oral
3. Taeyong Eom,Taehong Gwon, **Sijung Yoo,** MoσSung Kim, lain Buchanan, Manchao Xiao and Cheol Seong Hwang, “Kinetic Analysis of Atomic Layer Deposition Process of $(GeTe_2)_{(1-x)}(Sb_2Te_3)_x$ Layers for Phase Change Memories”, 제 21 한국 반도체 학술대회, 한양대학교, 2014년 2월 24일-26일, oral
4. **Sijung Yoo**, Taeyong Eom, Taehong Gwon, and Cheol Seong Hwang, “Bipolar Resistive Switching of $Ge_2Sb_2Te_5$ and $Ge_2Sb_2Te_7$ Thin Films without Involving Obvious Phase Change”, 제 21회 한국 반도체 학술대회, 한양대학교, 2014년 2월 24일-26일, poster

5. Taeyong Eom, Taehong Gwon, **Sijung Yoo**, Byung Joon Choi, Moo-Sung Kim, Lain Buchanan, Manchao Xiao, and Cheol Seong Hwang, “Conformal Formation of $Ge_2Sb_2Te_5$ film for phase change memories realized by controlling non-ideal behaviors of ALD”, 제 22회 한국반도체학술대회, 인천 송도컨벤시아, 2015년 2월 10일-12일, oral
6. Taehong Gwon, Taeyong Eom, **Sijung Yoo**, Moo-Sung Kim, Lain Buchanan, Manchao Xiao, and Cheol Seong Hwang, “Atomic Layer Deposition of chalcogenide novel Ge precursor”, 제 22회 한국반도체학술대회, 인천 송도컨벤시아, 2015년 2월 10일-12일, oral
7. **Sijung Yoo**, Taeyong Eom, Taehong Gwon, and Cheol Seong Hwang, “Bipolar resistive switching of amorphous $Ge_2Sb_2Te_5$ thin film without involving phase change”, 제 22회 한국반도체학술대회, 인천 송도컨벤시아, 2015년 2월 10일-12일, oral
8. Woojin Jeon, **Sijung Yoo**, Hyo Kyeom Kim, Woongkyu Lee, Cheol Hyun An, Min Jung Chung, and Cheol Seong Hwang, “Evaluating the top electrode material for achieving an equivalent oxide thickness smaller than 0.4nm from an Al-doped TiO_2 film”, 제 22회 한국반도체학술대회, 인천 송도컨벤시아, 2015년 2월 10일-12일, oral
9. **Sijung Yoo**, Taeyong Eom, Taehong Gwon and Cheol Seong Hwang, “Color-switchable optical coating by adopting multi-layers of ultrathin phase change material films”, 제 23회 한국반도체학술대회, 강원도 하이원리조트, 2016년 2월 22일-24일, oral

10. Kyung Jean Yoon, Yeong Jae Kwon, **Sijung Yoo**, Jung Ho Yoon, Hye Jin Kim, Dae Eum Kwon, Seul Ji Song, Tae Hyung Park and Cheol Seong Hwang, "Double Layer-Stacked 1D1R Crossbar Array Integrating Diode Selector with Rectification Ratio of ~10^9", 제 23회 한국반도체학술대회, 강원도 하이원리조트, 2016년 2월 22일-24일, oral
11. Taehong Gwon, Taeyong Eom, **Sijung Yoo**, Eui-sang Park, Sanggyun Kim, Moo-sung Kim, Iain Buchanan, Manchao Xiao, Sergei Ivanov and Cheol Seong Hwang, "Atomic Layer Deposition of GeTe and $Ge_xSb_yTe_z$ alloys using $Ge(N((CH_3)_3Si)_2)_2$ precursor", 제 23회 한국반도체학술대회, 강원도 하이원리조트, 2016년 2월 22일-24일, oral
12. Taehong Gwon, Taeyong Eom, **Sijung Yoo**, Eui-sang Park, Sanggyun Kim, Chanyoung Yoo, Han-Koo Lee, Deok-Yong Cho, Moo-sung Kim, Iain Buchanan, Manchao Xiao, Sergei Ivanov, and Cheol Seong Hwang, "Mechanism Study on The Atomic Layer Deposition of GeTe Films Using $Ge[N[Si(CH_3)_3]_2]_2$, $[(CH_3)_3Si]_2Te$, and Methanol", 제 24회 한국반도체학술대회, 강원도 대명비발디파크, 2017년 2월 13일-15일, oral
13. **Sijung Yoo**, Taeyong Eom, Taehong Gwon, Sanggyun kim, Euisang Park, Chanyoung Yoo and Cheol Seong Hwang, "Atomic layer deposition of 14-15-16 group ternary and quaternary thin films for Ovonic Threshold Switching selector device", 제 24회 한국반도체학술대회, 강원도 대명비발디파크, 2017년 2월 13일-15일, oral

14. Eui-sang Park, Taehong Gwon, **Sijung Yoo**, Chanyoung Yoo, Sanggyun Kim, Jaesun Jung, and Cheol Seong Hwang, "Atomic Layer Deposition of SnTe Phase-change Materials", 제 24회 한국반도체학술대회, 강원도 대명비발디파크, 2017년 2월 13일-15일, poster

15. Chanyoung Yoo, Taehong Gwon, **Sijung Yoo**, Eui-sang Park, Sanggyun Kim and Cheol Seong Hwang, "Atomic Layer Deposition of $TiTe_2$ Thin Films for Ti-Sb-Te Phase Change Memory Application", 제 24회 한국반도체학술대회, 강원도 대명비발디파크, 2017년 2월 13일-15일, poster

2.2 International

1. Taeyong Eom, Taehong Gwon, **Sijung Yoo**, Moo-Sung Kim, Manchao Xiao, lain Buchanan, and Cheol Seong Hwang, "Atomic layer deposition of $(GeTe_2)_{(1-x)}(Sb_2Te_3)_x$ pseudo-binary layers for phase change memories", ALD 2012, Dresden, Germany, June 17-20 (2012)

2. Taeyong Eom, Taehong Gwon, **Sijung Yoo**, Moo-Sung Kim, Manchao Xiao, Iain Buchanan, and Cheol Seong Hwang, "Investigation of Atomic Layer Deposition Properties of $(GeTe_2)_{(1-x)}(Sb_2Te_3)_x$ Pseudo-binary Compound for Phase Change Memory Application", Nature Conference 2012, Aachen, Germany, June 17-20 (2012)

3. Taehong Gwon, Taeyong Eom, **Sijung Yoo**, Moo-sung Kim, Iain Buchanan, Manchao Xiao, and Cheol Seong Hwang, "A new route for atomic layer deposition of GeTe film for phase change memory", ALD, San Diego Marriott Marquis & Marina, San Diego, United States, July 28-31 (2013), oral
4. Taeyong Eom, Taehong Gwon, **Sijung Yoo**, Moo-Sung Kim, Manchao Xiao, Iain Buchanan, and Cheol Seong Hwang, "Atomic layer deposition process and characterization of $(GeTe_2)_x(Sb_2Te_3)_ySb_z$ layers for phase change memories", ALD, San Diego Marriott Marquis & Marina, San Diego, United States, July 28-31 (2013), poster
5. Taeyong Eom, Taehong Gwon, **Sijung Yoo**, Moo-Sung Kim, Iain Buchanan, Manchao Xiao, and Cheol Seong Hwang, "Sub-atomic layer deposition using physically adsorbing precursor and kinetic analysis of deposition characteristics: Growth of $(GeTe_2)_{(1-x)}(Sb_2Te_3)_x$ layers using Ge^{4+} alkoxides", ALD 2014, Granvia Hotel, Kyoto, Japan, June 15-18 (2014), oral
6. Taehong Gwon, Taeyong Eom, **Sijung Yoo**, Moo-Sung Kim, Iain Buchanan, Manchao Xiao, and Cheol Seong Hwang, "New Chemical Routes for Vapor Phase Deposition of GeTe for Phase Change Memory", ALD 2014, Granvia Hotel, Kyoto, Japan, June 15-18 (2014), poster

7. Taeyong Eom, Taehong Gwon, **Sijung Yoo**, Byung Joon Choi, Moo-Sung Kim, Iain Buchanan, Manchao Xiao, and Cheol Seong Hwang, "Conformal formation of $(GeTe_2)_{(1-x)}[Sb_{(1-y)}Te_y]_x$ thin film for phase change memories application", 14th Annual Non-Volatile Memory Technology Symposium, Jeju, Korea, October 27-29 (2014), poster
8. Taehong Gwon, Taeyong Eom, **Sijung Yoo**, Moo-Sung Kim, Iain Buchanan, Manchao Xiao, and Cheol Seong Hwang, "New chemical methods for GeTe deposition for phase change memory application", 14th Annual Non-Volatile Memory Technology Symposium, Jeju, Korea, October 27-29 (2014), poster
9. **Sijung Yoo**, Taeyong Eom, Taehong Gwon, and Cheol Seong Hwang, "An analysis for bipolar resistive switching of $Ge_2Sb_2Te_5$ thin films without involving obvious phase change", 14th Annual Non-Volatile Memory Technology Symposium, Jeju, Korea, October 27-29 (2014), poster
10. Taeyong Eom, Taehong Gwon, **Sijung Yoo**, Moo-Sung Kim, lain Buchanan, Manchao Xiao and Cheol Seong Hwang, "Atomic layer deposition of $Ge_2Sb_2Te_5$ thin films for phase change memories", ALD 2015, Hilton Hotel, Portland, USA, June 28 - July 1 (2015), oral
11. Taeyong Eom, Taehong Gwon, **Sijung Yoo**, Moo-Sung Kim, Iain Buchanan, Sergei Ivanov, Manchao Xiao, and Cheol Seong Hwang, "Atomic layer deposition of $Ge_2Sb_2Te_5$ thin films for phase change memories", Atomic Layer Deposition: Russia 2015, September 20 - 21 (2015)

12. **<u>Sijung Yoo</u>**, Taeyong Eom, Taehong Gwon, and Cheol Seong Hwang, "Bipolar resistive switching behavior of amorphous $Ge_2Sb_2Te_5$", 1st International Symposium on Emerging Functional Materials, 송도 컨벤시아, November 4-6 (2015), poster

Abstract (in Korean)

칼코제나이드 물질은 고유의 다양한 전기적 스위칭 거동 – 통칭 OTS 또는 Ovonic Threshold Switching 으로 불리는 휘발성 저항변화, 또는 memory switching 으로도 알려진 상변화를 수반하는 전기적 특성 변화, 혹은 Electrochemical Metallization 에서의 높은 이온 전도도를 기반으로 한 고체 전해질로의 활용 – 으로 인해 많은 주목을 받아왔으며, 이로 인해 광학 저장 매체 및 차세대 비휘발성 메모리 응용 분야의 핵심 물질로 자리매김하고 있다.

본 논문은 칼코제나이드 박막의 전기적 스위칭 거동 및 상세한 연구와 그 응용에 대해 다루고 있다. 먼저 비활성 전극 (Ti 및 Pt) 사이에 위치한 비정질 $Ge_2Sb_2Te_5$ (GST) 박막의 양극성 저항 변화 (BRS) 메커니즘에 대해 보고하였다. 높은 저항비 및 안정적인 신뢰성 특성을 갖는 전형적인 양극성 저항 변화 메커니즘이 관찰되었으며, 고해상도 투과 전자 현미경 (HRTEM) 관찰을 통해 비정질 GST 매트릭스 내에 상부 전극과 하부 전극을 연결하는 전도성 Te 필라멘트가 존재함이 밝혀졌다. 전기 전도 메커니즘 분석을 통해 낮은 저항 상태 (LRS) 의 전도는 국부적으로 생성된 반도체 경로에

의해 지배되는 반면 높은 저항 상태 (HRS) 의 전도는 전극 전체 면적을 통한 Poole-Frenkel 메커니즘에 의해 지배됨을 알 수 있었다. 따라서 발견된 양극성 저항 변화 현상을 강한 전기장 하에서 이온화된 Te 이온의 이동을 통한 반도체 Te 필라멘트의 생성 및 소멸에 의한 것으로 결론지을 수 있다. Te 이온은 하부 전극 계면에 형성된 얇은 (~5nm) Te 층에 의해 공급된다.

둘째로, Ge-Sb-Te 삼성분계 및 Ge-Sb-Se-Te 사성분계의 원자층 증착 및 이의 높은 step coverage 를 바탕으로 한 선택소자로의 응용, 특히 3D 수직 소자에의 응용이 연구되었다. Ge(OEt)4, Sb(OEt)3, (Me3Si)2Te 및 (Me3Si)2Se 전구체를 사용하여 Ge-Te, Sb-Te 및 Sb-Se 의 이성분계 박막과 이를 조합한 pseudo-binary 박막의 증착이 이루어졌다. 증착된 삼성분계 및 사성분계 박막의 조성은 화학량론적 조성의 이성분계 박막의 조합으로 구성된 것으로 확인되었다. 다양한 조성을 2-terminal MIM 구조 소자로 시험하여, 박막의 조성이 threshold field (F_{th}) 을 비롯한 소자 동작 특성 및 endurance 를 비롯한 소자 신뢰성에 미치는 영향을 알아보았다. Ge : Sb 비율의 변화는 threshold field 의 변화로 이어지는 반면 endurance 는 거의 개선되지 않았다. 한편, Se 농도가 증가하면

endurance 가 크게 향상되는 반면, threshold field 는 거의 영향을 받지 않았다.

셋째로, 다층으로 쌓인 초박막 GST 에서의 상변화 거동 및 그에 따른 광학적 대비와 그 응용이 제시되었다. 광학 소자의 다양한 색상 변화는 유전체 산화물 장벽에 의해 분리된 여러 층의 초박막 GST 의 상전이에서 기인하였다. GST 필름의 다층 적층 및 각 층의 선택적인 상전이는 강한 간섭 효과의 변조와 그에 따르는 다양한 색상 변화로 귀결된다. 이를 통해, 착색된 기판 상에 증착된 1 층 이상의 초박막 GST (< 10nm) 를 통해 다양한 색상 변화가 가능한 정적인 광학 코팅이 가능함을 제시하였다. 반사 스펙트럼의 점진적인 변화는 GST 층의 선택적인 상변이로부터 비롯되었으며, 이는 transfer-matrix 광학 시뮬레이션을 통해 확인되었다. 또한, 전도성 원자력 현미경을 통해 나노 스케일의 이미지 기록의 실현 가능성 역시 다루어졌다.

주요어**:** 칼코제나이드 물질**,** 전기적 특성 변화**, GeSbTe,** 원자층 증착법
학번**:** 2014-30213

유 시 정